PONTIFICIA
UNIVERSIDAD
CATÓLICA
DE CHILE

CHARACTERISATION OF COMPACT STELLAR SYSTEMS IN THE COMA CLUSTER OF GALAXIES.

SIMÓN ÁNGEL

Tesis para optar al grado de Doctor en Astrofísica
Instituto de Astrofísica
Facultad de Física
Pontificia Universidad Católica de Chile

Abril 2021

SUPERVISORS:
Dr. Thomas H. Puzia
Dr. Patricia Tissera
Dr. Paul Goudfrooij

"Where must we go, we who wander this wasteland, in search of our better selves?"

— The First History Man

A mi familia y amistades.

ABSTRACT

We present the Coma Cluster Core PrOject (C^3PO), a deep, high resolution and contiguous mosaic survey of the inner $\approx$ 150 square arcminutes of the core of the Coma Cluster. The region was tiled by 21 HST/WFC3 pointings and was observed in F336W from the UVIS channel, and F160W from the IR channel. Using this data, and combining this with archival data in F475W and F814W taken previously in programs led by some of our team members, we study the compact stellar systems of said cluster. We separate those systems from background galaxies and foreground stars guided by a near-UV/visible/near-IR colour-colour diagram, obtaining more than 9000 objects. From our selection, we study the globular cluster luminosity function in our available bands, finding values of the turn-over magnitude of 26.2 mag for F814W, 27.3 mag for F475W, and 25.8 in F160W. We recover the blue and red GC populations found by Peng et al. [138], finding similar relative abundances and spatial distribution. We do not recover the colour distribution found by Madrid et al. [119] because their extremely red objects are not present in our data, most likely due to the inclusion of the *u* band. For the first time with such diagnostic power, age and metallicity are derived for distant GCs. 60% of our GC sample falls inside the range of our SSP models, finding an age-metallicity relation that does not correlate with any single colour, but is rather dependant on pairs of colours. The age and metallicity also do not correlate strongly with spatial distribution or environment. Colour-colour relations with visible (*gi*) colours show differences with varying environment, which may indicate differences in star formation history and chemical enrichment history. The dataset also contains a large number of UCDs, and the method can be easily expanded to also find NSCs.

ACKNOWLEDGMENTS

Muchas gracias a quienes me han apoyado, entendido y acompañado en este proceso de autodescubrimiento.

Based on observations with the NASA/ESA Hubble Space Telescope obtained at the Space Telescope Science Institute, which is operated by the association of Universities for Research in Astronomy, Inc., under NASA contract NAS5-26555. These observations are associated with program GO14182.

Software used: astropy [10], APLpy [157], matplotlib [92], ComEst [43], SExtractor [18], PSFEx [17], TOPCAT [166], STILTS [167], NumPy [171], galstreams [122].

CONTENTS

LIST OF TABLES

Part I

INTRODUCTION

1 INTRODUCTION

Massive galaxy clusters are regions of various galaxy evolution processes and provide rich laboratories for studying a wide variety of baryonic structures, from globular clusters (GCs), to giant galaxies. GCs, associated with both individual galaxies and with the intracluster medium, are one example of the several compact stellar systems (CSSs) that inhabit the galaxy cluster ecosystem, where we can also find ultra-compact dwarf galaxies (UCDs), especially numerous in rich, dense clusters, and nuclear star clusters (NSCs) that are found in the centres of many dwarf galaxies. Their characteristics, and in particular their relation to the galaxy population, are a vital piece of information to the understanding of the history of the mass assembly of the cluster since these are the only baryonic components which scale proportionally with the mass of the galaxies' dark matter haloes [22, 78, 91]. Studying the relative brightnesses, sizes, and location of these objects in the cluster environment requires deep imaging with a high spatial resolution that is currently only provided by the *Hubble Space Telescope* (HST). Several earlier investigations have concentrated on nearby galaxy clusters observed with the Advanced Camera for Surveys [ACS, 164], like in Virgo [83, 139, 64], Fornax [127, 98], and Coma [35, 149, 120, 138, 53, 54]. While these studies are extensive in area coverage and sample size, they all have the limitation of the available (typically, only two) passbands in ACS, covering only a part of the visible spectrum. Limited spectral coverage means limited information on the star formation histories and metallicities of the CSSs present in the studied galaxy clusters. Our team was already involved in a survey in the Coma cluster core with ACS, the HST/ACS Coma Cluster Treasury Survey (HST Program GO-10861, PI: David Carter), and its results were published in Carter et al. [35], from now on C08, and several other papers in a series. We will refer to this survey as the Coma Treasury Survey throughout this paper.

1.1 THE COMA CLUSTER OF GALAXIES

The Coma galaxy cluster [Abell 1656, 1] is a dense galaxy supercluster, among the closest to Earth in the Abell et al. [2] catalogue, and the nearest class-2 richness cluster. It contains over a thousand galaxies, from two massive elliptical galaxies, NGC 4874 and NGC 4889, passing through regular massive galaxies, mostly elliptical in the centre, and transitioning to a relatively higher spiral fraction towards

the outskirts [7], to dwarfs, like dwarf ellipticals [dEs, 53, 105] or ultra-compact dwarfs [UCDs, 38]. Coma is located where several filaments, including the Great Wall [77], intersect [see figure 1 of C08]. In fact, the Great Wall connects Coma with the near, equally rich cluster Abell 1367. Despite having two massive elliptical galaxies near its centre, the multi-wavelength emission of the intergalactic medium (IGM) radiation points to NGC 4874 being the true cD galaxy [see 13, and references therein], which is also hinted by the intra-cluster globular cluster distribution [138, but also see section 2.1 below]. The Coma cluster is a natural extension of the Fornax and Virgo cluster in terms of distance, size, mass, and density. We summarise the main structural properties in table **??**, and we explicitly use R_{200}, the radius of a sphere of mean density 200 times the critical density of the Universe, and not R_{vir} given that neither Virgo [19], nor Coma (see below) are truly virialised structures, while the massive galaxies in Fornax follow a virialised phase-space distribution [60, 58]. Its density and relative proximity make the Coma cluster a popular zero-redshift laboratory for a series of astronomical tests[1], with photometric observations in all possible wavelengths, from the high-energy end of the electromagnetic spectrum in γ-rays [4, 3], X-rays [159, 74], UV [84, 121], visible [among many others, the HST/ACS Coma Cluster Treasury Survey, C08], infrared [94, 103, 169], microwaves [143, 102], to the low-energy radio wavelenghts [75, 25, 27], taking into account observations only from the last $\sim$ 10 years. Several multi-object spectroscopic surveys in the Coma area have been conducted [30, 129, 47, 40, 38, 150, 76, 61, 173, 99, 5, 65], most of them being focused on observations of large galaxies, due to technical limitations present at the time of observation preventing massively targeting dim and small (CSSs), or extended and low-surface-brightness (ultra-diffuse galaxies) objects.

The evidence of Coma being dynamically active traces back to Bahcall [12], who noted an anisotropy on the galaxy distribution of the Coma cluster, with galaxies preferably oriented in the East-West direction. This is the axis on which the two cD galaxies are aligned (see figure 2), and the intracluster light (ICL) mostly follows this alignment [95]. This idea was later contrasted with the opposite point of view of Coma being quite symmetric and compact [101], or more recently, that the core temperature profile (that is to say, the region probed in this study), as measured by X-ray Iron K-lines, indicates a fairly relaxed state [161]. The spectral energy distribution (SED) of the ICL in Coma, as studied by Jiménez-Teja et al. [95] also shows photometric evidence of recent ($\sim$ 1 Gyr) stirring and dynamical activity, as per Jiménez-Teja et al. [96]. The distribution of galaxies, while sitting mainly on the E-W axis, shows subclumps and overdensities, as

1 Note that Pimbblet et al. [142] gave a word of warning concerning the usage of Coma as an archetype cluster, arguing that, while kinematically 'typical', its galaxy population is not typical for clusters of similar mass.

Cluster	DISTANCE (MPC)	R_{200} (MPC)	$\mathcal{M}_{200}$ ($10^{14} M_\odot$)	ρ_{200} ($10^{13} M_\odot$ MPC^{-3})
Coma	100[C08]	2.94[108]	27.73[108]	2.6
Virgo	16.5[124]	1.55[63]	4.2[63]	2.7
Fornax	20[21]	1.4[60]	0.7[60]	0.6

Table 1: Coma cluster properties compared to other nearby clusters.

shown by Fitchett and Webster [67], which is also observable when studying the velocity dispersion of the galaxies [125, 184, 46]. Coma also has an unusually high X-ray temperature, when compared to clusters of similar mass [as compiled by 142], and in the same spectral range, shows elongation towards the south-west, where NGC 4839 lies $\approx 0.^{\circ}56$ away from NGC 4874. Recent work presented in Lyskova et al. [118] also supports this scenario. This all adds to the idea proposed by Burns et al. [29] that Coma is a post-merger cluster, rather than a pre-merger or currently merging one, proposed by White et al. [179] and later by Neumann et al. [132]. In fact, Burns et al. [29] concluded that the NGC 4839 group already passed through the centre of the potential well $\sim$ 2 Gyr ago, a factor of two longer than what Jiménez-Teja et al. [95] found. Burns et al. also argue, showing hydrodynamical simulations, that the large radio halo found in Coma is due to this merger. Despite these differences, the studies cited above all agree that the perturbed state in which Coma is is a result of a merging process, with this south-west group (associated with NGC 4839) being dragged into the bottom of the potential well.

1.2 OBSERVING COMA

Two observational factors help with analysing the Coma cluster's photometric data: low extinction, and low foreground stellar contamination. As for extinction, our calculations using the Schlafly and Finkbeiner [162] extinction maps and the Fitzpatrick [68] reddening law give median values for A_λ of ~ 0.043 mag for the F336W HST/WFC3 UVIS filter, and ~ 0.005 for F160W HST/WFC3 IR, when taking into account the projected rectangle that encompasses our survey area. We show our calculated extinction map for the u_{336} filter in Figure 1. Note that the areas with larger extinction ($A_\lambda > 0.05$) that skew off the distribution are off northwest (top-left corner) of the main survey footprint, and therefore not affecting our data. On the other hand, the Besançon model of stellar population synthesis of our Galaxy [156][2] predicts a stellar surface number density of ~ 9500 stars deg^{-2} for the Coma Cluster position in the celestial sphere, not taking into account

2 http://model2016.obs-besancon.fr/

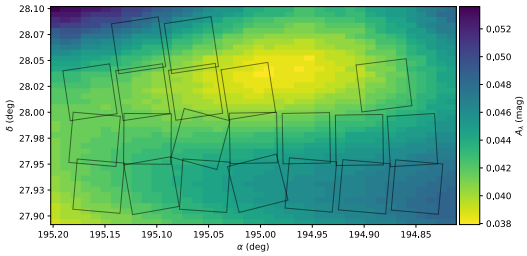

Figure 1: A_λ extinction map of the area around the footprint of our survey. Values are calculated for the F336W HST/WFC3 UVIS filter following Fitzpatrick [68] law and the map of Schlafly and Finkbeiner [162]. Median A_λ throughout this rectangular field is ~ 0.043 mag.

any magnitude or colour cuts (that is, considering the worst-case scenario), which translates to $\sim$ 19 stars for each HST/WFC3 UVIS tile ($\approx$ 7.3 arcmin^2). There is also no Galactic halo substructure in the direction of Coma, as compiled in the library used by the Python package GALSTREAMS [122][3].

In accordance with the Coma Treasury Survey results, we adopted a distance of 100 Mpc to the Coma Cluster, which is equivalent to a distance modulus $m - M = 35$ mag. This value is in good agreement with the measured redshift of $z = 0.023$ [52], even though with the recent cosmological values of $H_0 = 67.4$ km sec^{-1} Mpc^{-1}, and $\Omega_m = 0.315$ obtained by Planck Collaboration et al. [145], we obtain a slightly greater luminosity distance $D_L \approx 110$ Mpc. At 100 Mpc, one arcsecond corresponds to roughly 0.5 kpc.

3 https://github.com/cmateu/galstreams

2 SCIENTIFIC RATIONALE

2.1 INTRACLUSTER GLOBULAR CLUSTER POPULATION IN COMA

Peng et al. [138] discovered ~ 47,000 intra-cluster GC (IGC, a population of globular clusters bounded to the gravitational potential of the galaxy cluster rather than to the potential of a particular galaxy) candidates in the inner ~ $0.2R_{200}$ [i.e. ~ 270 kpc or ~ 9′ for $R_{200} \approx 2\ h^{-1}$ Mpc and $h = 0.678$, 108, 144] of Coma, from which ~ 20% had $g_{475} - I_{814}$ colours as red as GCs which belong to massive ellipticals, instead of finding a mostly blue population, as early simulations suggested [16, see below]. More recently, Madrid et al. [119] found an even redder GC colour distribution when studying a sample more spatially extended than the one used by Peng et al.: separating the sample at $g_{475} - I_{814} = 1.5$, they found that 52% of their GC candidates are red, and 48% are blue. This discrepancy comes most likely because of the extended spatial coverage used by Madrid et al., including a few extra fields around large galaxies, including secondary cD NGC 4889. Opposed to this, the simulations of Bekki and Yahagi [16] show a single metal-poor peak for the metallicity distribution of GCs, which translates to mostly only blue GCs. On the other hand, more recent results in smaller scale haloes (a Virgo-like cluster) find similar fractional numbers, with fractions as high as 40% of red IGCs [151], more consistent even with the nearly 50/50 red/blue separation found by Madrid et al.. They also find that the fraction of subhaloes merged with the main galaxy cluster halo, to the total of subhaloes, is nearly independent of the subhalo mass. Given that the number of GCs in a halo (and therefore, the number of GCs candidates to be stripped from it) is proportional to the host subhalo mass [91, 69], they conclude that massive haloes are the main IGCs progenitors, almost independently of the GC colours. This result is opposite to the idea that the IGC population cannot solely originate in and around dwarf galaxies, generating only GCs with low metallicities and blue colours, as previous studies suggested [117, 165]. We will collect evidence to support one of these views with the data from our survey, using the fossil record provided by the GCs. Since the typical physical size of these systems, as measured by their effective radius r_{eff}, is of the order of $r_{eff} \lesssim 10$ pc, which corresponds to an angular size of $r_{eff} \lesssim 0\farcs02$, or half of a pixel of HST/WFC3 in the UVIS channel in the case of Coma, it is safe to assume that GCs are unresolved at Coma distances. Hence, and with no option of doing massive multi-object spectroscopy, it is hard to distinguish them from

foreground stars or compact background galaxies, even with two optical passbands. Adding UV and NIR data to the existing optical information allows the usage of multi-wavelength selection tools (see section 3.2 below), which are not magnitude dependent (or, at least, depend only on photometry errors), as opposed to what has been done in previous, similar work, which has been mainly carried out using ACS, therefore relying only on a single colour as the selection tool [see, in the case of the Coma cluster, 138, 44, 114]. Having a more robust selection method for GC (and other CSS) candidates will lead to a better understanding of the baryonic systems in the Coma cluster.

2.2 NUCLEAR STAR CLUSTERS IN COMA

A large fraction of galaxies in the local Universe, across all morphological types, are occupied by compact sources at their centres, as compiled by Böker [23] from several sources. Several HST studies conclude that these sources have a stellar origin [34, 24]. These nuclear star clusters (NSCs) are as compact as GCs but have larger masses and luminosities, with typical dynamical masses of $10^6 - 10^7 M_\odot$ regardless of host galaxy size [175, 134] and around 40 times more luminous than a typical Milky Way (MW) GC[1]. Studies in the context of the ACS Virgo Cluster Survey [48] estimated that around $\sim 70 - 80\%$ of its early-type galaxies, with luminosities as low as $M_B \approx -16$ mag, host NSCs, regardless of the galaxy being dwarf or giant [49], while the Next Generation Fornax Survey [NGFS, 131] found that for bright galaxies ($M_{g'} \leqslant 16$ mag), the nucleation fraction reaches values of $\geqslant 90\%$, dropping to zero at magnitudes fainter than $M_{g'} \sim 10$ mag [134]. Also in the Virgo Cluster, it was found that the masses of NSCs $\mathcal{M}_{NSC}$, just like the masses of supermassive black holes (SMBHs) $\mathcal{M}_\bullet$, correlate with the bulge mass of their host galaxy $\mathcal{M}_{bul}$ (64, but see also 32 for a generalisation to other clusters and environments) with a ratio of NSC to bulge mass of $\mathcal{M}_{NSC}/\mathcal{M}_{bul} \approx 0.2\%$. This correlation has been observed regardless of galaxy mass, over four orders of magnitude [177], a correlation also found in NSCs in Fornax dwarfs by Ordenes-Briceño et al. [134], albeit instead of bulge mass, it was total galaxy mass $\mathcal{M}_{gal}$, since dwarves were being studied, and it was detected over a reduced mass range. The main difference between SMBH and NSC studies, which also turns out to be an advantage, is that the stellar populations of the latter can be examined to trace their evolutionary link with the galaxy in which they reside. Their luminosities and colours are tightly correlated, as found by the studies mentioned above in Fornax and Virgo, and there are indications of a wide range of ages in their stellar populations, evidence of recent star formation, and chemical enrichment being driven by internal mechanisms [158]. Following a selection and analysis procedure

1 For a comprehensive review of NSCs, refer to Neumayer et al. [133]

similar to Ordenes-Briceño et al. [134], we will detect and measure the stellar populations' properties (colours, ages, and chemical composition) of NSC, in order to derive stellar masses, and therefore test the $\mathcal{M}_{NSC}/\mathcal{M}_{gal}$ relation in Coma. That way, we will put in perspective the properties of stellar populations in the NSC, the host galaxy, and the galaxy GC population, especially its mass. Combining the mass function of the GC population (via its proxy, the luminosity function) with the individual residuals of the fit to the $\mathcal{M}_{NSC}/\mathcal{M}_{gal}$ relation [134, figure 10], that means, whether there is a relative excess or lack of galactic mass compared to the average, will give us key information about the relative importance of in-situ formation mechanism of NSC, versus the GC infall formation scenario. Our survey is deep enough to get to the turnover of the GC luminosity function, so we will be able to test these scenarios with our data.

Davies et al. [51] studied the nuclear stellar populations around eight active galactic nuclei (AGNs) observed with SINFONI, and found that in the central $\lesssim 10-100$ pc, those radiating at low efficiency, for example, $L \lesssim 0.1 L_{Edd}$, are associated with young ($\sim 50-100$ Myr) starburst, while older starburst ages are measured in more efficient AGNs. This essential piece of information can lead to predictions about the connection between the star formation (SF) processes in the centres of galaxies with the AGN activity, and this can be studied via the age gradient near NSCs as a function of galactocentric radius, using multicolour gradients as a proxy. Different scenarios predict different gradients: on the one hand, a positive (youngest ages towards the centre) to flat age gradient can be generated by a delay between the onset of SF and AGN activity and an accumulation of gas towards the AGN; on the other hand, a negative (oldest ages towards the centre) age gradient will be generated if the AGN activity quenches the SF. The latter case is shown in massive galaxies, as given by models that predict that these gradients scale predominantly with the galaxy mass, from strongly negative metallicity gradient (of inverse symbol with respect to the age gradient) in massive galaxies, to almost nonexistent in dwarf galaxies (see Tortora et al. 168, and den Brok et al. 53 for Coma Treasury Survey results) since in these environments it is stellar feedback (OB winds and supernovae ejecta) that constitutes the dominant internal mechanism of SF regulation. For dwarfs, especially the ones found in clusters, we also have ram pressure stripping, stripping the gas preferentially in the galaxies' outer regions first and in the very centre last, thus creating a positive age gradient. Finally, the GC infall scenario mentioned above can lead to negative gradients: as the GCs spiral towards the core, they begin losing stars, making the area around the centre look old in colours [8, 9]. These formation mechanisms are also reviewed by Renaud [153, §9.1], which adds the critical component of kinematics.

We can test all of these cases in galaxies down to the dwarf regime of $\mathcal{M}_{gal} \approx 10^7 M_\odot$, measuring their colour distributions at high spatial resolutions, identifying the various feedback sources to study their influence and relative importance on the environment of NSCs, aided by our panchromatic information to break the age-metallicity degeneracy. The extended wavelength coverage will also help reconstruct the star formation histories (SFH) of NSC host galaxies, and their connection to the feedback mechanisms mentioned earlier.

2.3 ULTRA-COMPACT DWARFS IN COMA

Ultra-Compact Dwarfs [UCDs, 141] are key to our understanding of star cluster formations, the missing satellite problem, and galaxy evolution and assembly, but are overall poorly understood objects, with unclear and disputed origins (see below). These objects have been found mainly in dense environments, and indeed a large population is present in the major nearby galaxy clusters, like Virgo [83, 97, 182], Fornax [89, 57, 126], and Coma [149, 120, 38], and it has been found that the number of UCDs scales with the mass of the host system [115], very much as the GC system, as was discussed above. UCDs [or dwarf-globular transition objects, DGTOs, 83] occupy a parameter space between the most massive GCs and compact dwarf ellipticals when taking into account their optical magnitudes, colours and their structural parameters. Therefore, at the moment, their formation has been explained both as giant GCs [70, but see also Chiboucas et al. 39], or as remnant nuclei after tidal stripping of nucleated dwarf ellipticals [140, 183]. However, a few other alternative mechanisms have been proposed, like merging of star clusters, to form "superclusters" [107, 28], or collapse of monolithic, supergiant molecular clouds [80], all of which are consistent with the dense environments in which UCDs reside. Another mechanism was proposed by Drinkwater et al. [59], which proposes that UCDs are actual compact dwarf galaxies, formed in the smallest peaks of primordial dark matter fluctuations, based on the spatial distribution of UCDs in Fornax: UCDs follow a much more concentrated distribution than nucleated dwarf ellipticals (dENs), that, since stripping would not change the orbital parameters of objects dramatically, is inconsistent with the tidal stripping scenario. This result has since been disputed by Zhang et al. [182] in the case of the Virgo cluster, arguing that the radially biased orbital structure for large galactocentric distances is, in general, in agreement with the stripping scenario. It has been found that UCDs have similar metallicities, internal velocity dispersions, and colour-magnitude relationships to those of CSSs. For instance, most M87 UCDs have colours similar to blue GCs and NSCs, which also show a colour-magnitude relation, with the most luminous (massive) UCDs also being the reddest [115]. This reinforces the

tidal stripping scenario. A crucial, yet still not known, aspect of UCDs, which may solve this problem, is their ages, particularly whether or not they are as old as GCs. So far, the optical colours used in UCD studies are not enough to discriminate between the old, metal-poor, and the young, metal-rich populations, due to the age-metallicity degeneracy presented in optical colours. Therefore, the inclusion of UV and NIR photometry will allow us to answer the question regarding the formation scenario of UCDs.

2.4 ULTRA-DIFFUSE GALAXIES IN COMA

Ultra-diffuse galaxies [UDGs, 172] are extended, low-surface brightness systems, having sizes of giants, but luminosities of dwarfs, with van Dokkum et al. [172] finding $L \sim 2 \times 10^8 L_\odot$, $R_e \sim 3.5$ kpc, and $\mu \sim 25$ mag arcsec^{-2}. It is been determined that these galaxies are old and metal poor [ages of ≈ 9 Gyr, and metallicites of [Fe/H]≈ -1, as measured by 81]. They are most likely dark matter dominated systems [172, 15]. They have been discovered in the nearby Virgo [128], Fornax [131, although these are smaller galaxies], and Coma [172, 104, 6] clusters, and in several other clusters with redshifts around two or three times the redshift of Coma [170]. Due to their characteristics, they are most efficiently discovered and characterised in deep, high-resolution imaging HST observations. Recently, spectroscopic observations have targeted these objects [173, 99, 5, 65, 81], confirming cluster membership, besides studying their stellar population properties and dynamics, and its disputed origin: both van Dokkum et al. [172] and Koda et al. [104] suggested that UDGs are 'failed' L^* galaxies, with quenched star formation at infall by gas stripping, whereas the spectroscopic study by Ferré-Mateu et al. suggest, besides failed primordial galaxies, an alternative scenario, with field dwarfs becoming quenched by infalling into the denser cluster environment. It must be stressed that, in order to explain their data, they need both scenarios. A third scenario is proposed, supported by simulations, in which gas outflows in isolated environment generates UDGs [55, 36]. With our dataset, we can apply an similar analysis to Amorisco et al. [6] to the UDGs in our field of view to accurately determine their stellar populations and estimate their star formation histories, testing the formation scenarios mentioned above.

Part II

THE DATA

3 OBSERVATIONS

Observations were carried out as part of HST program GO-14182 (PI: Thomas H. Puzia, Co-PI: P. Goudfrooij), which consisted of 63 orbits in HST Cycle 23, tiling the central field of the Coma cluster with 21 HST pointings. Observations were done between December 25th, 2015, and April 17th, 2017, using the Wide-Field Camera 3 (WFC3) in both the UVIS and the IR channels, in the F336W (from now on, u_{336}) and F160W (H_{160}) filters. Each tile was observed during three orbits: two for the u_{336} image, and one for the H_{160} image, yielding an effective exposition time of 5073 s for u_{336}, and 2806 s for H_{160}. Besides, we took advantage of parallel imaging using the Advanced Camera for Surveys (ACS) fields while observing with WFC3 and captured information in the F475W (g_{475}) and F814W (I_{814}) filters, in order to complement previous observations in such wavelengths, like the Coma Treasury Survey. The parallel fields' exposure times are 4454 s for g_{475}, and 2396 s for I_{814}. The u_{336} data for each pointing was split into 6 dithered long exposures of 820 s, plus two shorter exposures to avoid bright objects' saturation. We applied a post-flash illumination of 12 e^- to each u_{336} exposure to optimize the charge transfer efficiency of the CCD detectors in the UVIS channel of WFC3 [see 56, and references therein][1]. The g_{475} exposures were taken in parallel with the u_{336} exposures. The H_{160} data were obtained using the near-infrared channel of WFC3, featuring a 1024×1024 HgCdTe array with $0''.13$/pixel. The H_{160} exposures were taken using a 2-point dither pattern with spatial offsets designed to improve the sampling of the point spread function (PSF). Each H_{160} exposure used the SPARS100 up-the-ramp sampling sequence with 15 samples per exposure, resulting in effective exposure times of 1403 s. I_{814} exposures were obtained in parallel with the H_{160} exposures, taking two 648-s I_{814} exposures at each of the two dither positions. A summary of the observation dates, positions, and internal denominators, as well as some other complementary details, is presented in tables 2 and 3.

3.1 FIELD COVERAGE

Figure 2 shows the spatial coverage of our survey (filled tiles), compared to archival data (open tiles), obtained with HST/ACS of similar photometric quality and spectral coverage, from the aforementioned

1 http://www.stsci.edu/hst/wfc3/documents/handbooks/currentIHB/wfc3_cover.html

VISIT	α_{2000}	δ_{2000}	TARGET	START TIME (UT)	END TIME (UT)
01	13h00m37.4664s	+27d55m43.4227s	TILE-01	2015-12-25 00:26:33	2015-12-25 02:48:21
03	13h00m12.8834s	+27d55m45.023s	TILE-03	2015-12-29 22:09:43	2015-12-30 00:30:16
06	12h59m35.9678s	+27d55m41.1828s	TILE-06	2016-01-01 18:35:09	2016-01-01 20:55:24
07	12h59m23.7522s	+27d55m40.3828s	TILE-07	2016-01-01 23:21:39	2016-01-02 01:41:51
05	12h59m48.331s	+27d55m47.4728s	TILE-05	2016-01-04 21:22:00	2016-01-04 23:43:29
08	13h00m38.403s	+27d58m25.9527s	TILE-08	2016-01-10 00:07:49	2016-01-10 03:43:39
04	13h00m00.6243s	+27d55m53.3145s	TILE-04	2016-03-03 14:17:19	2016-03-03 16:40:02
18	12h59m31.407s	+28d01m33.556s	TILE-18	2016-03-04 12:33:10	2016-03-04 14:55:59
15	13h00m39.4741s	+28d01m09.4813s	TILE-15	2016-05-23 13:11:53	2016-05-23 15:35:24
16	13h00m27.2337s	+28d01m09.7614s	TILE-16	2016-05-24 09:51:45	2016-05-24 12:15:16
17	13h00m15.0234s	+28d01m11.0414s	TILE-17	2016-05-25 11:17:49	2016-05-25 13:41:14
20	13h00m28.2279s	+28d03m52.5414s	TILE-20	2016-05-27 08:34:53	2016-05-27 11:47:00
21	13h00m15.9952s	+28d03m53.2801s	TILE-21	2016-05-28 04:27:56	2016-05-28 08:06:29
19			TILE-19	2016-05-31 06:14:38	2016-05-31 09:33:49
02	13h00m25.2228s	+27d55m44.9891s	TILE-02	2016-11-11 17:12:14	2016-11-11 20:54:32
14	12h59m24.8176s	+27d58m23.3561s	TILE-14	2016-11-16 03:30:39	2016-11-16 05:53:18
12	12h59m49.3848s	+27d58m29.8114s	TILE-12	2016-11-18 03:12:39	2016-11-18 05:34:30
11	13h00m01.6439s	+27d58m30.7314s	TILE-11	2016-11-18 17:57:03	2016-11-18 21:28:21
13	12h59m37.0917s	+27d58m23.7719s	TILE-13	2016-11-20 01:19:42	2016-11-20 03:40:48
09	13h00m26.1612s	+27d58m27.7342s	TILE-09	2016-11-24 00:46:18	2016-11-24 03:06:33
10	13h00m13.8628s	+27d58m27.1673s	TILE-10	2017-01-06 10:01:45	2017-01-06 14:51:10
59	13h00m02.8047s	+28d01m13.8966s	TILE-19-COPY	2017-04-17 13:16:03	2017-04-17 15:39:32

Table 2: Summary of observations of the C^{3}PO survey, u_{336} data. Positions cited are similar for the H_{160} data, and times, similar for the g_{475} data.

VISIT	α_{2000}	δ_{2000}	TARGET	START TIME (UT)	END TIME (UT)
01	13h00m39.8164s	+27d49m49.8427s	TILE-01	2015-12-25 03:34:34	2015-12-25 04:21:45
03	13h00m14.723s	+27d49m50.9076s	TILE-03	2015-12-30 01:16:32	2015-12-30 02:03:43
06	12h59m38.3175s	+27d49m47.5995s	TILE-06	2016-01-01 21:41:42	2016-01-01 22:28:53
07	12h59m26.1021s	+27d49m46.7954s	TILE-07	2016-01-02 02:45:50	2016-01-02 04:51:30
05	12h59m50.6809s	+27d49m53.8881s	TILE-05	2016-01-05 00:31:42	2016-01-05 01:18:53
08	13h00m40.7538s	+27d52m32.3715s	TILE-08	2016-01-10 04:55:23	2016-01-10 06:56:57
04	13h00m26.5802s	+27d54m25.8738s	TILE-04	2016-03-03 17:26:16	2016-03-03 18:13:27
18	12h59m58.0043s	+28d00m49.3378s	TILE-18	2016-03-04 15:42:13	2016-03-04 16:29:24
15	13h00m43.4211s	+28d07m00.5832s	TILE-15	2016-05-23 16:21:35	2016-05-23 17:08:46
16	13h00m31.1807s	+28d07m00.8618s	TILE-16	2016-05-24 13:01:27	2016-05-24 13:48:38
17	13h00m18.9702s	+28d07m02.1471s	TILE-17	2016-05-25 14:27:25	2016-05-25 15:14:36
20	13h00m32.1748s	+28d09m43.6354s	TILE-20	2016-05-27 12:33:12	2016-05-27 13:20:23
21	13h00m19.9436s	+28d09m44.3861s	TILE-21	2016-05-28 09:13:00	2016-05-28 10:00:11
19			TILE-19	2016-05-31 10:20:01	2016-05-31 11:07:13
02	13h00m20.595s	+27d49m55.3939s	TILE-02	2016-11-11 21:45:08	2016-11-11 22:32:19
14	12h59m23.2065s	+27d52m29.0602s	TILE-14	2016-11-16 06:39:29	2016-11-16 07:26:40
12	12h59m48.9365s	+27d52m34.9223s	TILE-12	2016-11-18 06:20:42	2016-11-18 07:07:53
11	13h00m01.1956s	+27d52m35.8423s	TILE-11	2016-11-18 22:14:33	2016-11-18 23:01:44
13	12h59m36.7314s	+27d52m28.8651s	TILE-13	2016-11-20 04:27:01	2016-11-20 05:14:12
09	13h00m26.4138s	+27d52m32.811s	TILE-09	2016-11-24 03:52:49	2016-11-24 04:40:00
10	13h00m20.8127s	+27d52m44.2882s	TILE-10	2017-01-06 14:54:32	2017-01-06 16:35:25
59	13h00m06.9836s	+28d07m04.5126s	TILE-19-COPY	2017-04-17 16:25:41	2017-04-17 17:12:52

Table 3: Summary of observations of the C^{3}PO survey, I_{814} data. Positions cited are similar for the g_{475} data, and times, similar for the H_{160} data.

Coma Treasury Survey and programs GO-11711 [PI: John Blakeslee, 20] and GO-12918 [PI: Kristin Chiboucas, 37].

The WFC3 mosaic was arranged based on the relatively larger field of view (FOV) of the UVIS channel with respect to the IR channel (162×162 arcsec^2 vs 123×136 arcsec^2, respectively). The fields were rotated so that the parallel ACS fields broaden the spatial coverage of the archival data. This produces a contiguous mosaic of an area of $\approx$ 153 arcmin^2 in u_{336} of the core of the Coma Cluster (blue tiles). Given that the IR FOV is slightly smaller, the H_{160} mosaic (magenta tiles) covers a smaller area of $\approx$ 98 arcmin^2. The positions of these pointings were selected so that they preferentially target the location of previously known NSCs, IGCs, and other CSSs [138, 38]. Parallel data taken using ACS filters g_{475} and I_{814} is shown in yellow, respectively. One of the pointings was rotated so that the corresponding ACS parallel field contained one of the UDGs of van Dokkum et al. [172]; therefore it is not aligned with respect to the rest of the parallel fields.

3.2 SPECTRAL COVERAGE

Our observations span a wide wavelength coverage: from the near-UV (u_{336}, central wavelength = 3355 Å), to the near-IR (H_{160}, central wavelength = 1.537 µm). With these new data, combined with the previous optical information (g_{475}, central wavelength = 4746 Å; I_{814}, central wavelength = 8045 Å)[2] the colour-colour (CC) photometric selection tool developed by Muñoz et al. [130] for the Next Generation Virgo Survey [NGVS, 63] Infrared (NGVS-IR) can be applied, which helps identify unresolved GCs and other CSSs, and separate them from both foreground galactic contamination, and background, high-redshift galaxies. Despite not having exactly the same spectral energy distribtion (SED) coverage (the method of Muñoz et al. 130 uses a redder filter, K_s from CFHT-WIRCAM, plus CFHT-MEGACAM SDSS-like filters, slightly redder than u_{336}), the method works with similar filters: Ordenes-Briceño et al. [134], for instance, use VISTA K_s (central wavelength = 2.147 µm)[3] and Blanco-DECAM SDSS-like filters. Therefore, by using H_{160}, the reddest filter available in HST, it is possible to separate stars from simple stellar populations (SSPs) and other passively evolving aggregations that optical colours would not be able to. The addition of these filters also allows to break the age-metallicity degeneracy present when using purely optical colours in studies regarding the formation and evolution scenarios of CSSs. This can be seen in figure 3, that shows SSP evolutionary tracks constructed with PÉGASE-HR [110], using an interpolation of the BASEL

2 http://www.stsci.edu/hst/wfc3/ins_performance/ground/components/filters
3 http://casu.ast.cam.ac.uk/surveys-projects/vista/technical/filter-set

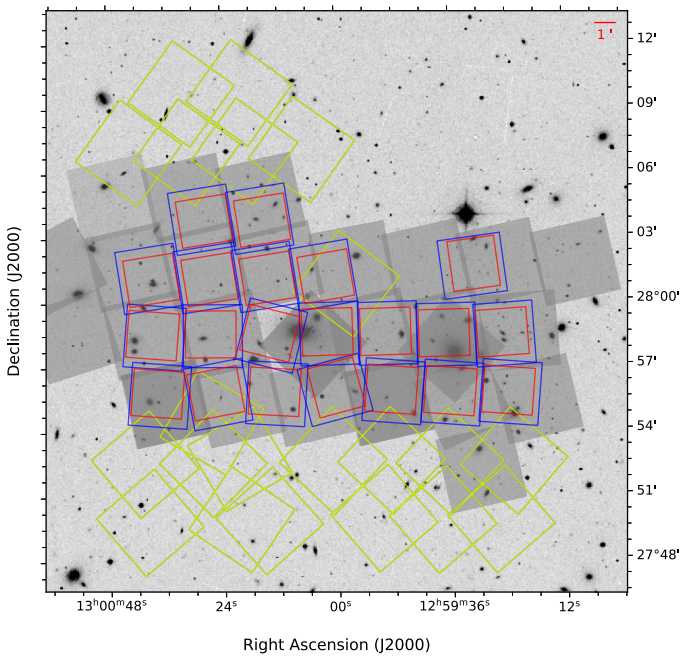

Figure 2: Spatial coverage of the new data (open squares) compared to the archival data (gray squares) of archival HST programs (see section 3.1). Different colours indicate different filters: blue tiles are u_{336} images; red, H_{160}; yellow, g_{475} and I_{814}, since the footprints of these filters overlap and at this scale are indistinguishable. Background is a DSS-2 R image

3.1 stellar SEDs [178][4], in the different possible colour-colour combinations made from this new data and the archival information. Panel *a* shows the uIH CC plane; panel *b*, gIH, which is the CC plane used in [figure 14 of 44]; panel *c*, ugIH; and panel *d*, ugI, the only one not using NIR information. The spectra produced by PÉGASE-HR were redshifted to the Coma cluster redshift of $z = 0.023$ [52] before performing the colour calculation. This is a small, but noticeable correction, especially in the u_{336} band: Cho et al. [44] calculated K-corrections of 0.05 mag and smaller (in absolute value) for g_{475}, I_{814}, and H_{160}, which is on the order of the tolerance of our photometry errors. Since Cho et al. do not have u_{336} data, they do not calculate K-correction for that filter. To estimate it, we used the K-corrections calculator[5] of Chilingarian et al. [42] and Chilingarian and Zolotukhin [41]. Their calculator does not support HST/WFC3 nor HST/ACS filters, but supports SDSS filters, so as an approximation for u_{336}, we used SDSS u, and SDSS i for I_{814}. For $1.5 \lesssim u_{336} - I_{814} \lesssim 4.5$, the approximate colour range on the left panel of figure 3, we obtain a median K-correction of 0.1 mag, same size of the error marker in figure 3.

We also see in figure 3 that, for typically observed GC ages (1 Gyr and over), the addition of the H_{160} band, and therefore the extended dynamic range in both axes of the uIH CC space helps discern between populations of different ages and different metallicities ($z = 0.0001$ to 0.1, roughly [Fe/H] $= -2.3$ to 0.7), in particular, between young, metal-poor, and old, metal-rich populations. This will be key to understand whether nuclear star clusters are young or old. In panel *b*, we also indicate with a grey open rectangle the parameter space sampled by the GCs of Cho et al. [44], which correspond to the GC system of the Coma cD NGC4874, and with a grey filling, the $g_{475} - I_{814}$ colour range occupied by the GCs found in Peng et al. [138]. u_{336} also has an enormous value as it indicates spatially zones of recent stellar formation. Combined with the high spatial resolution of WFC3/UVIS, it is possible to resolve the star formation regions of galaxies, which are not resolved in H_{160} (see figure 11 and section 6.2 for an extended discussion).

4 http://professor.ufabc.edu.br/~pieter.westera/BaSeL.html
5 http://kcor.sai.msu.ru/

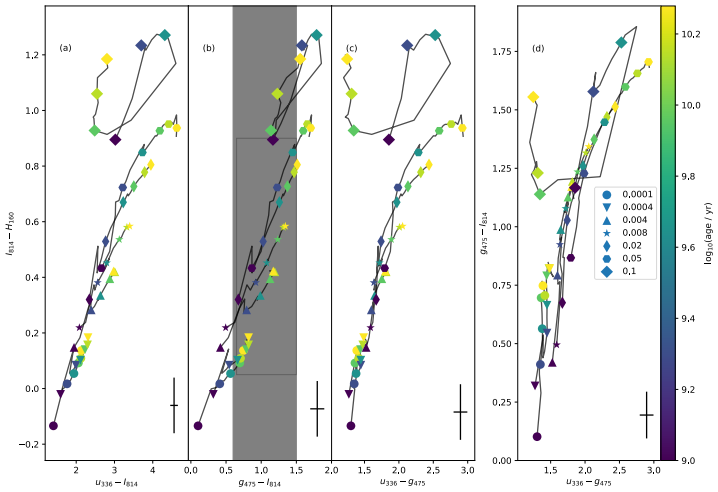

Figure 3: Comparison of PÉGASE evolutionary tracks for evolution of a single stellar population at $z = 0.023$, in uIH (panel *a*), gIH (*b*), ugIH (*c*) and ugI (*d*) colour-colour planes. All magnitudes are AB magnitudes. The addition of the H_{160} band is crucial to separate old, metal-poor populations from their young, metal rich counterpart. Symbols at the bottom right on each panel show a 0.1 magnitude error in both axes. The open rectangle in panel *b* shows the approximate colour-colour range of GCs in Cho et al. [44], while the grey filled area shows the $g_{475} - I_{814}$ range spanned by the GCs of Peng et al. [138].

4 DATA PROCESSING

Data processing was performed at the Space Telescope Science Institute (STScI). It involved dedicated wrapper scripts that use modules from the DrizzlePac [11][1] software package, including `AstroDrizzle` and `TweakReg`.

4.1 IMAGE COMBINATION

For the image stacking and combination, `AstroDrizzle` ran on every set of associated images (i.e., all images taken in one visit with the same filter) using the setting `driz_separate = True`. This created "singly drizzled" output images, which are the individual exposures after correction for geometric distortion using the World Coordinate System (WCS) keywords in the image header. The software package SExtractor [18] was then run on each singly drizzled image, using a signal-to-noise threshold of S/N = 10. The resulting catalogues were trimmed using object size, location, and shape parameters were chosen to reject most cosmic rays, detector artifacts, diffuse extended objects, and objects near the edges of the images. Using these cleaned catalogs, residual shifts and rotations between the individual singly drizzled images were then determined using `TweakReg`. This yielded formal alignment uncertainties below 0.1 pixel. The reference image is always taken to be the image observed first in the visit. The resulting shifts and rotations were then implemented in a second run of `AstroDrizzle` to verify the alignment.

Cosmic ray rejection was performed within `AstroDrizzle`, which uses a process involving an image that contains the median values of each pixel in the (geometrically corrected and aligned) input images as well as its derivative (in which the value of each pixel repre-

1 http://www.stsci.edu/hst/HST_overview/drizzlepac

Instrument/Filter	`final_pixfrac` (PIXEL)	`final_scale` (ARCSEC/PIXEL)
WFC3/F336W	0.90	0.039
WFC3/F160W	0.85	0.128
ACS/F475W	0.80	0.05
ACS/F814W	0.80	0.05

Table 4: `AstroDrizzle` parameters used for final image combination

sents the largest gradient from the value of that pixel to those of its direct neighbours; this image is used to avoid clipping bright point sources) to simulate a "clean" version of the final output image. For the H_{160} images, for which cosmic ray rejection is already done during the ramp slope fitting procedure of the basic pipeline reduction, we used the default cosmic ray reduction settings in `AstroDrizzle` (`combine_type = minmed`), which use the median value unless it is larger than the minimum value by a $4\,\sigma$ threshold. For the images taken with all other instrument/filter combinations, we have at least four images per visit and chose to use settings `combine_type = median` and `combine_nhigh = 1`, which uses the median value after rejecting the pixel with the highest value.

Sky subtraction was performed on each image prior to the final image combination, using iterative sigma clipping on the region shared by all images with a given filter. The resulting sky values were stored by `AstroDrizzle` in header keyword MDRIZSKY of the individual `_flt.fits` or `_flc.fits` images; our wrapper script then calculated the average sky rate in e^-/s for that filter and stores it in header keyword MDRSKYRT of the final `AstroDrizzle` output file (`_drz.fits` or `_drc.fits`), which also uses e^-/s units. This is done to allow the sky level to be added back in, which is needed to obtain photometry with proper magnitude errors.

4.2 VISUAL ASESSMENT OF IMAGE QUALITY

An example of the final combined image can be seen in Figure 4, in which we show the data of Visit 01 of the survey, located on the bottom-left tile of Figure 2: on the top-left panel, the H_{160} image is shown; on the top-right panel, the u_{336} image is shown. Images are at neither the same colour scale nor pixel scale, and are both shown with an arcsinh stretch. It is possible to note both the larger UVIS FOV (shown by different scales in both axes), and the greater depth of the IR data (sky level with respect to objects, i.e. stars or large galaxies, is lower in the IR image with respect to the UVIS image), due mainly to the relatively higher throughput and wider wavelength range of the H_{160} filter. The position of u_{336} with respect to the 4000-Å break also has to be considered[2]. We include as well the ACS parallel fields corresponding to Visit 01 on the bottom panels: g_{475} on the left, and I_{814} on the right. Those tiles are located further below and to the left of the bottom-left corner in figure 2.

2 This is both a blessing and a curse: low UV flux on one hand, diagnostic power to separate CSSs from background sources and foreground stars on the other.

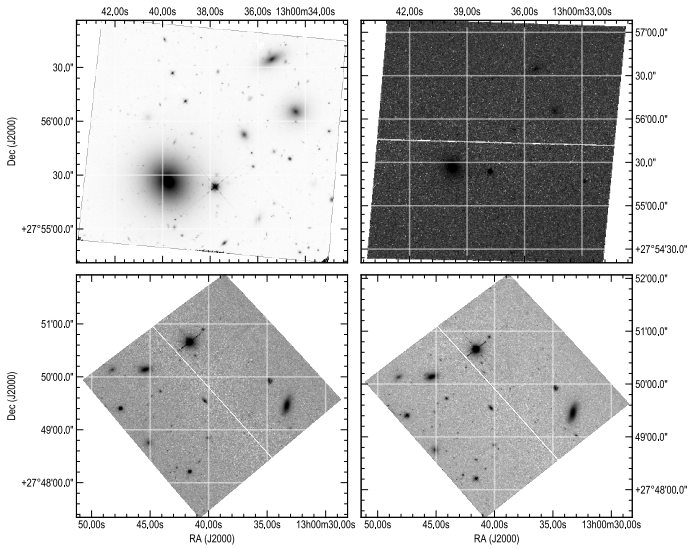

Figure 4: Data from Visit 01, the bottom-left tile of Figure 2. Top-left, H_{160} image; top-right, u_{336} image; bottom-left, g_{475} image; and bottom-right, I_{814} image. All four images are shown with a arcsinh stretch, and they are neither at the same colour scale, nor the same pixel scale, except the bottom two panels, that share the same pixel scale. In all panels, north is up and east is right.

5 DATA QUALITY CONTROL AND CALIBRATIONS

In order to be consistent with the Coma Treasury Survey, we performed SExtractor [18] and PSFEx [17] photometry on the WFCe/UVIS images with the values provided in Table 5 of Hammer et al. [85]. These parameters were also used when analysing the ACS images in both filters. Due to different pixel scale, depth, and FWHM, the WFC3/IR (i.e., H_{160}) images have been analysed with a slightly different set of values. Because of this, we did not run SExtractor in double image, forced photometry mode, and rather the images were SExtracted independently.

5.1 ASTROMETRIC CALIBRATION

To test the quality of our astrometric calibration, we matched the sources in our data with the *Gaia* data release 2 [71, 72] using STILTS [167], with a tolerance of $0\farcs5$. To be sure that only stellar sources are being matched, we restrict the effective radius of sources of our catalogue to be of only a few pixels maximum (see figure 17 and section 7), ending up with 58 matches in H_{160}, and 105 in u_{336}. Then we studied the distribution of the separation between the sources in the matched catalogues, finding that for both filters there was a peak in the separation distribution around $\approx 0\farcs4 - 0\farcs45$. This difference of $\approx 0\farcs4$ is equivalent to $\approx$ 10 pixels for WFC3/UVIS (u_{336}), and $\approx$ 3 pixels for WFC3/IR (H_{160}). Further dissecting the separation between the sources in the catalogues, it was found that this shift is mainly caused because the data in both passbands was calibrated to a position slightly towards the south with respect to the *Gaia* Celestial Reference Frame [*Gaia*-CRF2, 73], as can be seen in the blue curve in figure 5, where we plot the difference between coordinate values in our data, minus coordinate values in *Gaia* data, $\Delta\,\mathrm{coord} = (\alpha,\delta)_{C^3PO} - (\alpha,\delta)_{Gaia}$, as well as the absolute separation. There is no apparent shift towards the east or west (red curve in both left panels of figure 5 looks whether uniform or peaking around $0''$). Secondary and lesser order peaks in these distributions correspond to differential shifts in different visits of our survey. This process was repeated for the g_{475} and I_{814}, showing a peak again in the separation distribution at $\approx 0\farcs42$, and a dominant peak in the $\Delta\delta$ distribution, same behaviour as shown in figure 5, with 84 matched sources for g_{475}, and 78 for I_{814}. This is to be expected since the parallel data was observed simultaneously as the main data, using the same guiding stars, and they were astrometrically calibrated to the same

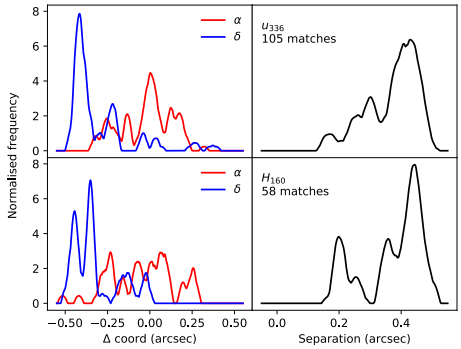

Figure 5: Distribution of the difference in coordinate values $\Delta\,\mathtt{coord} = (\alpha,\delta)_{C^3PO} - (\alpha,\delta)_{Gaia}$ (*left*) and separation (*left*) between the matched sources in our data and the *Gaia* DR2 catalogue, in both u_{336} (*top*) and H_{160} (*bottom*) filters. In both left panels, red curve represents difference in right ascension; blue curve, in declination. Distribution in all panels is estimated with a KDE using an Epanechnikov [62] kernel with a 0.03″ bandwidth.

frame of reference. There is no correlation between the distribution of sources in the sky and Δ coord.

When matching between the u_{336} and the H_{160} catalogues (see section 5.4 below), we noted that for Visit 59 we had an unusually low (almost an order of magnitude less) number of matched sources. This was because our images were aligned $\approx 0\farcs75$ away relative to each other, so the handful of matched sources we were getting were not even actual matched objects. This motivated a re-calibration of the astrometric solution for each image, reframing their WCS by minimising the median distance between objects in our catalogue and objects in the *Gaia* catalogue, independently on both axes. We had between one and ∼ 20 matched sources for each image. The reframing we performed was only a linear shift, subtracting the median distance between matched sources to the `CRVAL1` and `CRVAL2` values of each image's header. We did not modify the projection of the images, since we found no correlation between separation and position within the image, nor any evidence of rotation. The steps of this realignment procedure are presented graphically in figure 6 and elaborated here, for an example visit: we start with the H_{160} image of Visit 07 after the image processing described in section 4.1 (top left), in which we have overplotted the *Gaia* DR2 sources in the area of the image, and the matched sources in our catalogue as it was described above. Then, we study how Δ coord varies with respect to the corresponding coordinate (top right). Finding no correlation between these quantities (not in this particular example, nor any other case), we then determine that only a linear shift is needed. Studying the distribution of

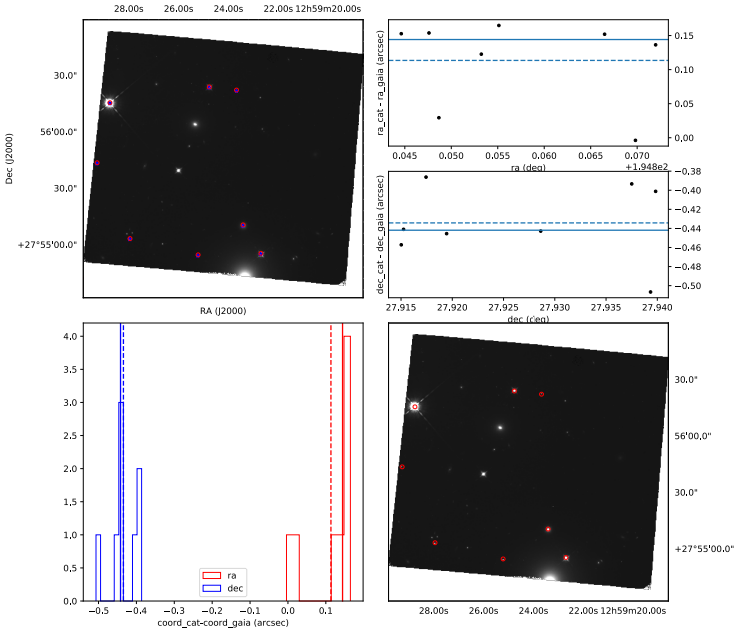

Figure 6: Example of the reframing procedure. *Top left*, Visit 07 H_{160} image, with *Gaia* sources (red circles) and their matched sources in our catalogue (blue stars) overlaid. *Top right*, difference between out catalogue and *Gaia* coordinate as a function of coordinate: top, right ascension; bottom, declination. In this and the following panel, solid line is the median of the offsets, and dashed line is the average. *Bottom left*, histogram of these offsets. In red, right ascension; in blue, declination. *Bottom right*, Visit 07 H_{160} image after shifting by the median difference in both coordinate axes, with the *Gaia* sources overlaid, showing the result of the realignment.

Δ coord (bottom left), we decided to use its median (solid line in the bottom left and top right panels) to set the offset, instead of the average (dashed line), given that outliers more easily skew the latter. Finally, in the bottom right panel, we present the image after the realignment procedure, with the *Gaia* sources again overplotted, showing that they are more well-aligned with the sources in our catalogue.

We studied the origin of this discrepancy between the WCS solution of our images and the *Gaia* frame of reference, and theorised that the discrepancy could arise between the *Gaia*-CRF2 and the Guide Star Catalog II [GSC-II, 109][1] used for HST pointing. These two catalogues were matched around the Coma cluster area with a tolerance of 1″. Surprisingly, the trend shown by the matched catalogues is entirely different to the ones observed in figure 5: the difference in $\Delta\,\mathrm{coord} = (\alpha,\delta)_{GSC-II} - (\alpha,\delta)_{Gaia}$ distributes as a gaussian curve peaking around 0″ and with a standard deviation of $\sigma \approx 0\farcs14$ for declination, and for right ascension, as a double gaussian with a primary peak in $\approx 0\farcs125$, and a secondary peak around $\approx 0\farcs42$ with $\approx 60\%$ the height of the primary peak. This difference has been addressed in the recent ACS Instrument Science Reports of Kozhurina-Platais et al. [106] for sources in *Gaia* DR1 near Milky Way GCs ω Cen and 47 Tucanae. Therefore, the conclusion is that there was an internal error in the procedure described in section 4.1 and the images were not aligned correctly with the sky frame of reference. Most likely, the issue is that individual guide stars have positional offsets with respect to the reference frame of GSC-II, therefore conditioning the WCS of each visit. As a closing remark, we were cautious when comparing catalogues to avoid discrepancy due to differences in J2000 or J2015.5 equinoxes, since *Gaia* catalogues include positions in both equinoxes. After having all 84 images re-aligned with the *Gaia*-CRF2 world coordinate system, we proceeded to re-run our SExtractor reduction procedure and continue with our catalogue generation.

5.2 EXTINCTION IN THE LINE OF SIGHT

As mentioned in section 1.2, Coma is located near the Northern Galactic Pole, and is therefore barely obscured by galactic extinction, which is mostly predominant when observing toward the disk or bulge. We studied the distribution of extinction coefficients over our survey footprint using Schlafly and Finkbeiner [162] extinction maps and Fitzpatrick [68] reddening law with a flat spectrum. In figure 7 we show the distribution of extinction values for a discrete rectangular grid over our survey footprint for all the four filters in our data. All four distributions have roughly the same shape due to the A_λ being calculated with a constant spectrum, and have minor differences not visible to this scale due to different reddening values in our footprint. As

1 http://gsss.stsci.edu/Catalogs/GSC/GSC2/GSC2.htm

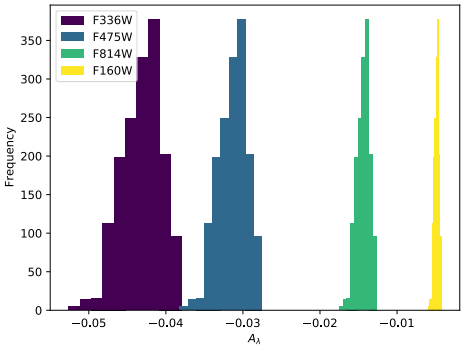

Figure 7: Distribution of extinction values calculated in our survey footprint area for our four filters.

expected, the most affected filter is F336W with a median integrated extinction value of $A_\lambda = -0.043$ mag; the least affected is F160W with a median integrated extinction value of $A_\lambda = -0.005$ mag. The standard deviation of those distributions is 0.0026 mag and 0.0003 mag respectively. Given that the spread of A_λ values is rather low, we use the median value for the entire footprint as the outlier values skewing off the distribution are actually located outside our footprint (top-left corner of figure 1).

5.3 COMPLETENESS OF POINT SOURCES

One of the survey's science objectives is to study the global GC population of the cluster and the link to the nuclear star clusters of dwarf galaxies, so assessing the completeness of point sources in our data is a key aspect. We tested completeness using the ComEst Python package [43][2], injecting 100 sources per square arcminute in our images and running SExtractor with the same extraction parameters as in the science run. We repeated this process two hundred times for each image. Our simulations show that the survey is, on average, complete at 50% at 28 mag for u_{336} and 26.32 mag for H_{160}. Completeness as a function of magnitude, as obtained with ComEst is shown in figure 8. Completeness of each tile is shown with a different line, which are colour-coded with the tile's median surface brightness measured in AB magnitudes per square arcsecond. This allows noting that frames with brighter galaxies, and therefore higher average surface brightness, reach 50% completeness at brighter magnitudes. This average brightness effect is more evident when studying the H_{160} data, which also shows a wide range of median surface brightnesses compared to the other filters ($\approx$ 3 mag vs $\approx$ 0.5 mag). Losing objects in these

2 https://github.com/inonchiu/ComEst

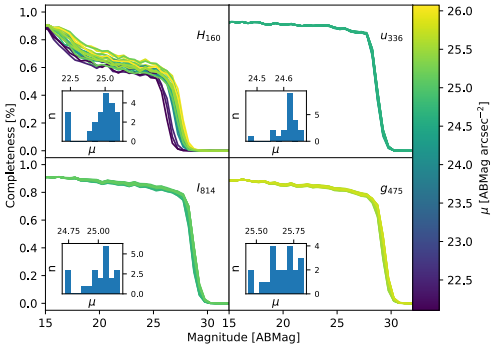

Figure 8: Completeness diagrams for our data. The four panels show the information in the different filters, and for each filter we plot the completeness as a function of magnitude of the sources of each tile. Completeness lines for different tiles are colour-coded by the median surface brightness μ of the tile, measured in AB magnitude per square arcsecond. In each panel, the insert shows a histogram with the distribution of these surface brightnesses, showing a wide spread in the H_{160} data, which is not found in the other filters.

"bright tiles" may be prevented by subtracting the galaxy flux from the images.

To put the 50% completeness limits in perspective, we consider the measured GC Luminosity Function (GCLF) turnover (TO) of $m_U(\sim u_{336}) = 17.65$ [14] and $m_H(\sim H_{160}) = 14.7$ [176] for M31 GCs. Taking the distance to Andromeda as 780 kpc [123], its distance modulus is $m - M = 24.46$ mag, so when recalculating these GCLF-TOs to Coma distance, they convert to $m_U = 28.19$ and $m_H = 25.24$, which are roughly the 50% completeness limits calculated for our data.

We also calculated the 50% completeness limit for the parallel g_{475} an I_{814} bands, which is on average at 27.9 mag. The corresponding GCLF-TO in i_{814} was calculated to be equal to 25.5 mag in Madrid et al. [119]

5.4 CATALOGUE GENERATION

The individual image catalogues were then merged into two master catalogues. These master catalogues of objects with well-measured photometry have 43845 sources in the H_{160} catalogue, and 1182174 in the u_{336} catalogue. Then, they were matched by their sky positions with a 0.″4 maximum separation, equivalent to 8 pixels in the u_{336} images and ≈ 3 pixels in the H_{160} images. We studied the distribution of the separation between the matched objects, finding a peak around 0.″066 (≈ 1.3 pixels for u_{336}, and ≈ 0.5 for H_{160}), and that 80% of the matched sources had a companion less than 0.″3 away. The matched

catalogue has 32610 objects with well-measured photometry in both bands. Considering that the FOV of the IR channel of WFC3 is smaller than the FOV of the UVIS channel, as mentioned in section 3.1, we are losing $\approx$ 18000 sources in the matching process because of this. This accounts for over 50% of our total numbers, according to the UVIS channel being $\approx$ 57% larger than the IR channel. Another reason for this decrement of objects maybe galaxies being "shredded" in the u_{336} images (see section 6.2.1 below), or different contrast or background levels between background and sources between the u_{336} and H_{160}.

6 GENERAL ANALYSIS OF SOURCES

6.1 SPATIAL DISTRIBUTION OF SOURCES

In figure 9 we show the distribution of all of the objects detected in the u_{336} and H_{160} catalogues, plus the 32610 objects in the matched catalogue described in section 5.4. The horizontal and vertical gaps between tiles are caused by the smaller IR channel of WFC3 relative to the UVIS channel. The overdensity of objects centred at $(\alpha, \delta) \approx (12h59m35s,\ 27^{o}58')$ and spanning several tiles coincides with the position of the cD galaxy NGC 4874, and likely corresponds to the IGC system as measured by Peng et al. [138], but not as measured by Madrid et al. [119] since they measure higher projected spatial densities around the secondary cD galaxy NGC 4889, uncharted territory for Peng et al.. At this spatial resolution, GC systems of individual galaxies would not be observable since they would be smoothed out. Other than that, the distribution is fairly homogeneous, a good indicator that most of the objects detected are background sources (see below).

6.2 MAGNITUDE DISTRIBUTION OF SOURCES

We show in figure 10 the magnitude distributions for the master catalogues in each filter, before the match, and also the distribution of matched sources as was described above. We use the SExtractor parameter `MAG_AUTO` as the source magnitude in this context. We see that, for most of the magnitude range observed, the index of the power-law (the slope of the curve in logarithmic space) is preserved after the matching process. It is important to note that several (several tens) objects brighter than $\texttt{MAG\_AUTO}_H \sim 16$ are not matched with an u_{336} counterpart. We propose that this phenomenon be explained by the photometric "shredding" of late-type galaxies, where their star-forming regions are detected as separate objects in u_{336} but are not separated in H_{160}. We explain this in the next section.

6.2.1 *Galaxy "shredding" in the u_{336} images*

We show an example of such shredding in figure 11. The galaxy is SDSS J130039.50+275547.8, present on the tile corresponding to Visit 01. Tens of star formation regions are detected in the NUV filter (red circles), hinting at the galaxy's spiral morphology, while the lower resolution, different PSF, and actual different physical mechanisms

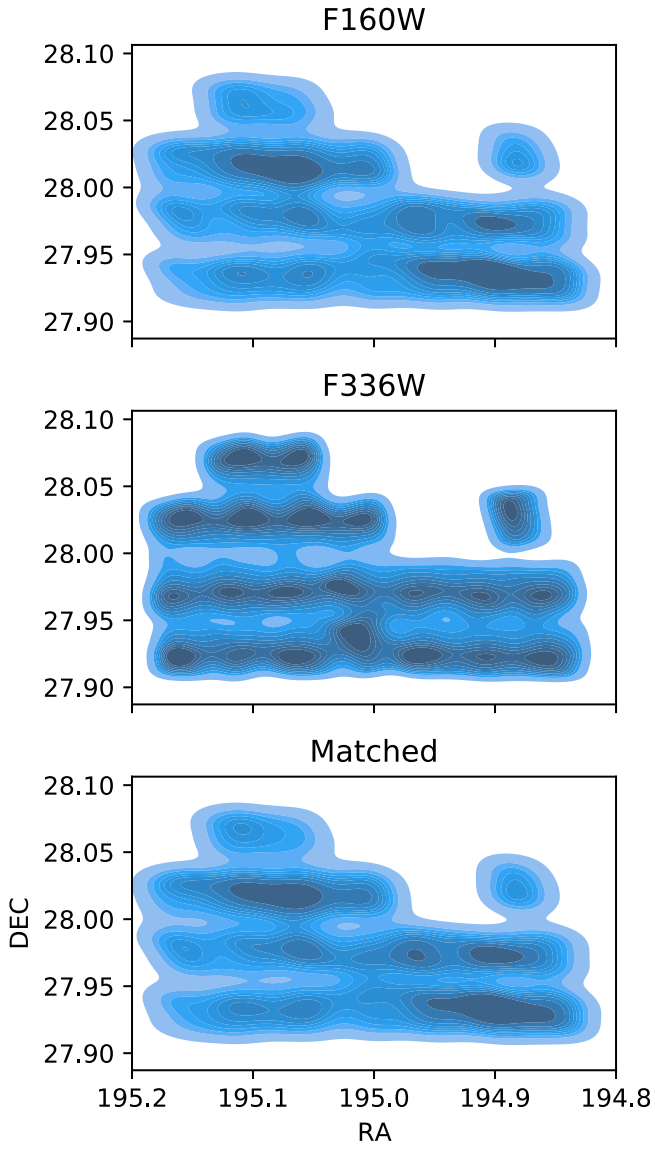

Figure 9: Object distribution in the H_{160} catalogue (top), u336 (middle) and matched (bottom) catalogues.

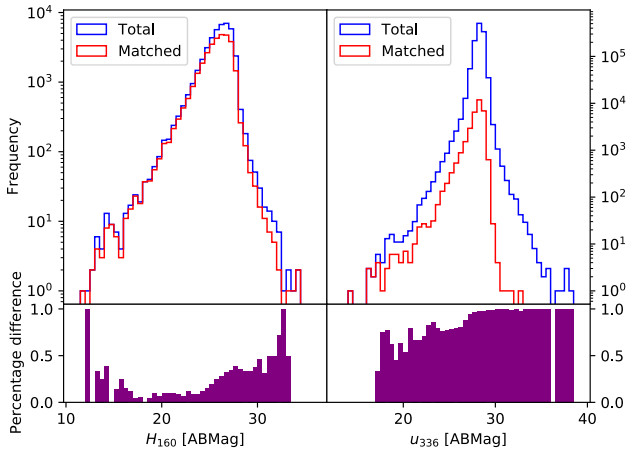

Figure 10: Distribution of magnitudes in our main data set, before (red) and after (blue) matching between the two filters. Top left, H_{160} data; top right, u_{336} data. Bottom panels show the difference between the histograms of the total and matched catalogues.

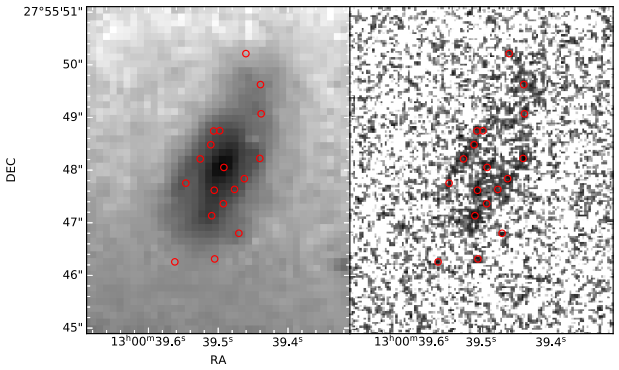

Figure 11: Example of how the galaxy SDSS J130039.50+275547.8, detected as a single object in H_{160} is divided into several detections in the u_{336} images (red circles)

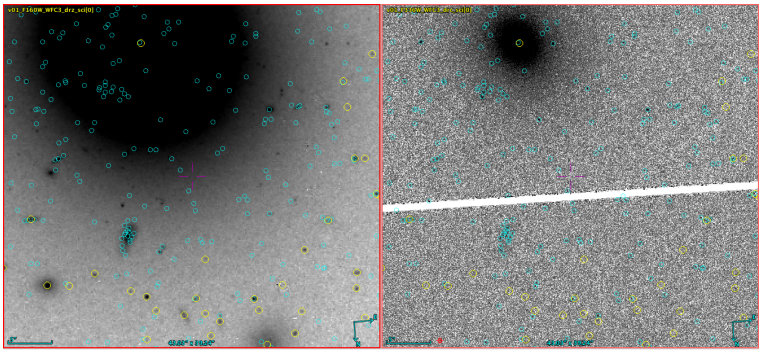

Figure 12: Detected objects in the vicinity of NGC 4906 in Visit 01, in the F160W (lest) and in F336W passbands (right). Note that the cutouts in figure 11 is included in this field of view

being probed in the infrared allow only the detection of the object as a whole. Segregation like this can explain the dearth of matched objects bright in H_{160}: in these cases, the centre of the object in IR, as determined by SExtractor is several pixels apart from the nearest detection in NUV, and over our tolerance of 0.″3 when matching objects from sources. If this happens to most star-forming galaxies (which are less common in Coma than passive galaxies, but nonetheless important), that would explain this lack of objects bright in H_{160} that have no apparent match in u_{336}. Note also that NGC 4889 and NGC 4874, the brightest galaxies in Coma, have their photocenters *outside of the IR mosaic*. Therefore, the bright flux of these objects detected in H_{160} won't have *meaningful* matches in u_{336}.

6.3 GALAXY FLUX REMOVAL IN F160W DATA

Because most of the galaxies in the core of Coma are elliptical with old, cold stars, they are very bright and extended mainly in the red and infrared filters, like F160W. Combined with the fact that the IR channel has a lower resolution than the UVIS channel of WFC3 and ACS, software that automatically detects sources like SExtractor has many difficulties detecting sources immersed in the galaxies' light such conditions. Failure of detecting objects near galaxies may be fatal for studies of globular clusters like the one present here, knowing that they most like are going to cluster around (bright) galaxies. In our case, there was an evident shortage of detected sources surrounding galaxies in our F160W data, as seen in figure 12 for the vicinity of NGC 4906 in Visit 01. This figure shows the objects detected with our SExtractor procedures. Many bright objects detected in the F336W data cannot be automatically detected in F160W due to the reasons exposed above. The lack of objects in the infrared data motivated a

search for several galaxy flux removals. Three main strategies were tested, one parametric and two non-parametric:

1. Usage of GALFIT[1] [136, 135] to fit parametric models. This software proved useful if the structure of galaxies wanted to be studied, and the relatively low number of galaxies per tile made it feasible to use. In the end, many galaxies required heavy tweaking due to having many components and both of the cD galaxies were clipped and their light profile truncated, and even their photocentre was outside of the tile in some occasions. which difficulties the fitting procedure of the software. Since obtaining the galaxy structure was not a goal of this study, this method was dismissed.

2. Iterative masking of point sources and medianing of the images, as described in Fischer et al. [66]. In several iterations, SExtractor runs over an image, point sources are masked, and then a median filter of decreasing size as the iterations proceed is applied to the masked image. This smoothed image is subtracted from the original data, and the process continues. This process gives good results and works well with bright, clipped galaxies, but the presence of bright stars or many point sources close to some of the galaxies left some holes in the medianed mask, which artificially generated residuals that difficulties the automatic detection of sources too close from the centres or in locations like medium-sized galaxies.

3. Iterative subtraction of background. Using SExtractor's automatically generated global background available in the `BACKGROUND` check image. This is a general light profile of the image, which then was smoothed with a decreasing size median filter as the previous method. The background map is created from the local background of each detected source. This method did not require any masking, so there were no holes in the substracted light and therefore, no artifacts.

Ultimately, based on ease of coding and strategic use of resources, the last method was used. We ran a three-iteration procedure with a square box of 101, 51 and 21 pixels as our median filter. Figure 13 shows the results of one iteration of this procedure running over the F160W data of our visit 10. This field includes most of the light, but not the photocenter, of NGC 4874, which is at the top left corner in this visualization. All image panels are shown with the same colour scale and stretch. From the top left panel and moving right, we have: *Original*, the data from the image; *Background*, the output background map from SExtractor in which the brightest sources can be seen and

1 https://users.obs.carnegiescience.edu/peng/work/galfit/galfit.html

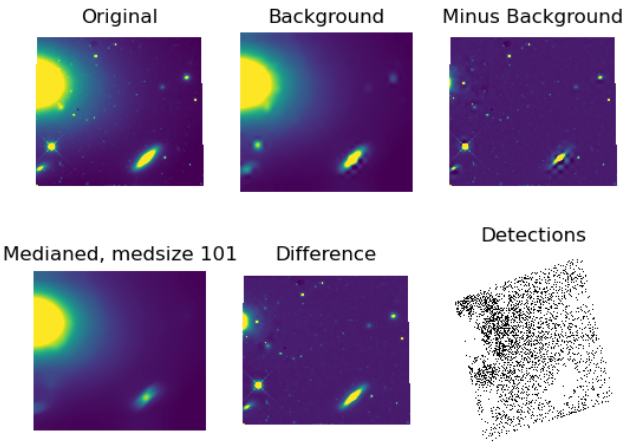

Figure 13: Example of the results of the first iteration of our galaxy light removal procedure on the F160W data of visit 10.

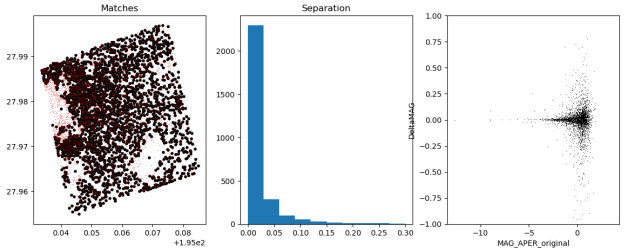

Figure 14: Example of the results of the galaxy light removal procedure on the F160W data of visit 10.

identified as background sources; *Minus Background*, also a SExtractor check image which is just the image minus the background. Then, on the bottom row, *Medianed, medsize 101* is the background map smoothed with a square median filter of 101 pixels a side; *Difference* which is the original data minus the smoother background; *Detections*, which are the sources detected automatically and from which the background map is built.

After iterating the process and reducing the filter size, we tested the integrity of the photometry of the already detected sources, to probe if we were losing more than we were gaining. We did this by matching the original catalogue of sources for each visit with the image's catalogue after the iterative procedure and see how much their calculated flux was changing. The results for the same visit are shown in fig-

ure 14. We see the detections for the original, unaltered image (black circles) and the final, galaxy-removed image (red dots) in the left panel. Many more sources are detected towards the centre of NGC 4874 and other galaxies in this field. In the middle panel, we plot the match separation distribution. We used `astropy.coordinates.match_catalog_sky` with `nthneighbor=1` and applied a cut of 0.″3 to make sure that we had actual matches. Most of the matches have a separation of less than 0.″03, a tenth of our cut. Finally, in the right panel, we show the magnitude difference. The majority of the objects have a change in magnitude of $\Delta\text{mag} < 0.1$ mag, which is well within our accepted magnitude errors. Plus, that difference increases as the magnitude increases, so that variance may be due to actual errors in measuring the magnitude of dim objects and not error introduced in the galaxy removal process. Therefore, this method proved useful and applied to the data in other filters with virtually the same results.

6.3.1 *New catalogues, matching and completeness*

After removing the galaxy flux from our images, we again run our main procedures:

1. Automatic detection of sources with SExtractor: we ran our detection procedure with the same inputs and parameters for our new set of images. We have 43845 sources in the original catalogue and 108746 sources in the final catalogue, so this method means an increase of 150% in detections. These new sources are preferentially located around the cD and lesser galaxies of the cluster, which is to be expected given our galaxy flux removal procedure.

2. Catalogue matching with STILTS: we ran STILTS to match our catalogues with the same parameters as before. As expected, we have more matches due to the higher number of objects in the F160W catalogue. When matching, we tested for different tolerances and found that, for values higher than 0.″5 the confusion in regions with high surface density of objects rends less matches than when performing the same match with a smaller threshold.

3. Completeness test with COMEST: we ran again the automatic completeness test with COMEST and compared it with the previous result (see section 5.3 and figure 8). Figure 15 shows the comparison: in the left panel we have the completeness as a funcion of magnitude for the untouched images, in which we see that images with a high surface brightness have a steeper completeness curve as was discussed above. On the other hand, in the right panel we have the completeness as a function of magnitude for the frames with the galaxy flux sustracted. In this

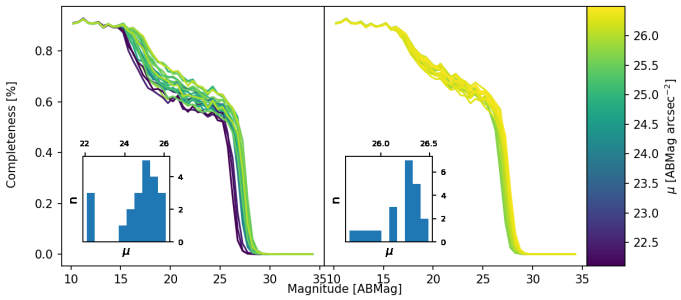

Figure 15: Comparison of the completeness in the F160W data before (left) and after (right) the galaxy flux removal.

case, the curves hold their shape compared to the left panel, but their average 50% completeness limit is a bit dimmer, albeit unnoticeable at this scale: before galaxy flux removal, it was 26.32 mag; after our iterative procedure, it is 26.49 mag, almost half a magnitude dimmer. We also note that the surface brightness distribution is much less spread after galaxy flux removal: spanning a bit more than 4 magnitudes before, now it spans less than a magnitude.

7

PRELIMINARY OBJECT CHARACTERISATION

We will now examine the different types of objects found in our images. In order to proceed on categorising the objects, we plot in figure 17 the size-magnitude relation for all objects detected by SExtractor in the data of Visit 01, using half-light radius (HLR) and MAG_AUTO measured by SExtractor. We will focus our analysis on the u_{336} and H_{160} images; the analysis can be extended to the ACS parallel fields data. The sparsely populated horizontal locus at HLR $\sim$ 1.3 pix corresponds to stars, mainly at MAG_AUTO $\lesssim$ 23 mag. Stars brighter than $\approx$ 18.5 mag in u_{336} and $\approx$ 16 mag in H_{160} are saturated. At dimmer magnitudes, we will also find compact stellar systems. Objects with HLR $\gtrsim$ 10 pix and brighter than $\approx$ 24 mag in u_{336} are likely Coma cluster member galaxies. Finally, objects with HLR $\lesssim$ 2 pix and MAG_AUTO $\gtrsim$ 23.5 mag are most likely background, barely- and un-resolved objects. We can also use a colour-magnitude diagram (CMD) to study the behaviour and properties of some of the groups of objects just mentioned. From the matched catalogue described in section 5.4, we create a $u_{336} - H_{160}$ CMD, shown in figure 16. Points are coloured according to their HLR in the u_{336} band in pixels, as measured by SExtractor. Both sets of objects mentioned above can be seen: the stars, and the cluster galaxies. As described, stars and cluster members are the brightest objects in our data. In fact, almost all of the objects brighter than $\approx$ 23 u_{336} mag are either stars or cluster galaxies. They can be discerned by their HLR, as was done before: stars have a practically invariant HLR of $\approx$ 1.4 pix, almost independent of their magnitude and colour. Only saturated stars have artificially higher values for HLR due to their central brightness profile reaching a plateau rather than a gaussian, which confuses SExtractor and creates an unrealistic larger value. Cluster galaxies, on the other hand, while being brighter than the majority of objects, are redder and more extended (HLR $\gtrsim$ 20 pix) than stars, and can be seen as the sequence of violet points between $3.5 \lesssim u_{336} - H_{160} \lesssim 6$ and $18 \lesssim u_{336} \lesssim 22$.

7.1 COMPACT STELLAR SYSTEMS

The detailed analysis of CSSs will be presented in the next chapters. The newly collected data, combined with the archival g_{475} and I_{814} information, allows usage of the method described in section 3.2 to separate CSSs from background sources and foreground stars. With our data sample described in section 5.4, we tested compatibility with the catalogue from den Brok et al. [54], which compiled the nuclear

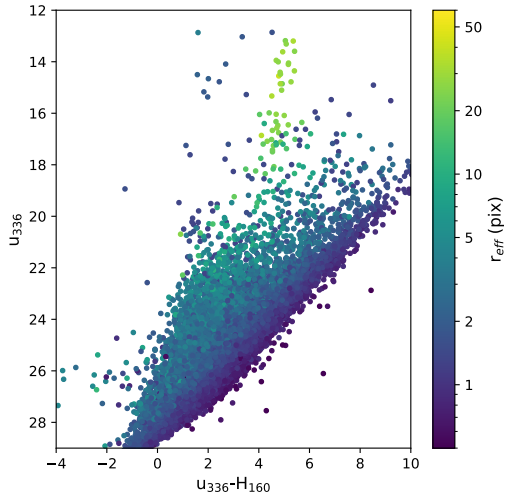

Figure 16: PLACEHOLDER IMAGE. Colour-magnitude diagram for sources in the matched catalogue described in section 5.4. Colour-coded is the HLR of the objects in the u_{336} data. Notable sequences include the stellar sequence at $u_{336} \lesssim 23$ and HLR$\approx$ 1.5 pix, regardless of their colour, and the cluster galaxies, with HLR$\gtrsim$ 20 pix, that show their known colour-magnitude relation: the brighter, the redder.

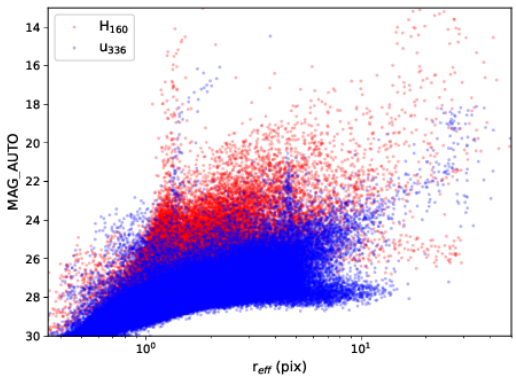

Figure 17: Size-magnitude plot for all detected objects in the u_{336} and H_{160} catalogues.

star clusters of galaxies in Coma. We have ~ 160 members of that catalogue in the survey footprint area. We also have matches between our catalogue and the spectroscopically confirmed UCDs of Chiboucas et al. [38].

7.2 CLUSTER MEMBERS

Having already several catalogues of confirmed and candidate members of the Coma Cluster [90, 53, 180, 181], we will extend the physical measurements (HLR, orientation, elongation, to mention a few) for these objects to our data with extended SED coverage. It is also possible to trace the "choppiness" of these galaxies with the u_{336} filter, indicating substructure and star formation regions, as was discussed above. Coma galaxies are well constrained in the CMD, because, most of them being early-type, they follow a colour-magnitude relation: as they get brighter, they get redder as well. This relation has been documented for Coma cluster galaxies, in particular, recently by Head et al. [88] with CFHT/MEGACAM NUV-optical (ugi) photometry. We are now expanding the SED coverage and can confirm that the galaxy colour-magnitude relation holds, even when combining NUV and NIR information.

7.3 DWARF AND ULTRA-DIFFUSE GALAXY CANDIDATES

Having g_{475} and I_{814} archival data added to the new images means that deep, high spatial resolution RGB images of the cluster can be constructed. These can be used to look for dwarf and ultra-diffuse galaxy (UDG) candidates, using the visual inspection method developed in Muñoz et al. [131], since these objects are well beyond SExtractor's detection limit, and therefore do not show up in figure 17. In recent years van Dokkum et al. [172] and Koda et al. [104] found almost 1000 ultra-diffuse galaxies in the central 4.1 degree^2 area of Coma, most of them Milky-Way sized. Following these numbers, we should expect ~ 10 of these galaxies in our survey. Our improved wavelength coverage, spatial resolution, and negligible sky variation will allow us to search for candidates more effectively and avoid spurious detections, using the method mentioned earlier of visual inspection of RGB images.

7.4 BACKGROUND SOURCES

Even in deep images of dense environments, it is expected that most detections belong to background sources. We consider two methods to differentiate these objects: One, constructing RGB images it is possible to identify, via visual inspection, high-redshift clusters, since all of its members will appear bright red in a confined space; and two,

from a CC diagram, like the one used to separate CSSs, it is also possible to separate high-redshift objects [see figures 14-15 of 130]. Expanding the spectral coverage to the NUV with u_{336} will allow us to also estimate photometric redshifts of background galaxies at $z \approx 3$ using the Lyman break at 912 Å [87, figure 1]

7.5 FOREGROUND STARS

Stars can be separated from other sources because they are bright and compact, as was mentioned above. Their main feature is their HLR of $\sim$ 1.4 pix, regardless of their magnitude or colour. This can be confirmed by examining figure 16 since the stellar sequence is a well-dispersed sequence in the 2-D CMD, but the third axis constrains it. However, it is possible to have stars in this sequence dimmer than magnitude $\approx$ 23, as seen in the right panel of figure 17, but here they are mixed with all of the other objects. Despite being low-number statistics (we have on the order of a hundred stars in our footprint, see below), the distribution of stars in the CMD suggest a particular clustering around $u_{336} - H_{160} \approx 1.7$, which might correspond to the colour of the main sequence (MS) turn-off (MSTO) of stars in the MW halo. As revealed by Besançon model simulations, the synthetic population for the Coma area (i.e. MW halo stars) has a MSTO at $u_{336} - H_{160} \approx 2.4$, and calculations using the halo MSTO obtained by the CC diagrams in Lokhorst et al. [116] in MEGACAM u, g, and i, and Powalka et al. [146] adding WIRCAM K_s, both from NGVS data, with extrapolation to our colour set using synthetic spectra from the PHOENIX spectral library [93][1] at the appropriate surface temperature and gravity intervals, yields an average colour of $u_{336} - H_{160} \approx 1.3$. Therefore, the values obtained by simulations and by data bracket widely our obtained result. This discrepancy may arise from the disparity in the SED regions we are probing, which may be calibrated differently for the PHOENIX and Besançon models. The colour distribution for stars has a secondary peak at $u_{336} - H_{160} \approx 7.1$, which, according to the Besancon prediction, corresponds to the MS "knee", a feature well documented in deep photometry of stars in globular clusters (see Bono et al. 26 and Saracino et al. 160 for a compilation of observations). Finally, as mentioned in section 1.2, the Besançon model predicts a few stars per tile, which translates to roughly 60 in the entire survey. Some of them were evident to find in the images, due to their diffraction spikes (e.g. the bright star near the galaxy in the top panels of figure 4). As mentioned in section 4.2, we have several matched sources between our catalogue and the *Gaia* catalogue: 56 in the H_{160} catalogue, and 103 in the u_{336} catalogue, which correspond to 0.57 stars per square arcmin in H_{160}, and 0.67 in u_{336}. This is $\approx$ 5 times lower than the predicted

1 http://phoenix.astro.physik.uni-goettingen.de

$\approx$ 2.6 stars per square arcmin given by the Besançon model, as mentioned in section 1.1, but this was not taking into account any cuts in magnitude or colour. When adjusting for photometric limits of the matched C^{3}PO-*Gaia* data ($G_{Gaia} < 21$ mag), the stellar surface density drops by a factor of $\approx$ 7.5, to 1260 stars per square deg, or 0.35 stars per square arcmin, which is closer, but lower by a factor of $\approx$ 2 than the number of stars estimated from our data.

Part III

COMPACT STELLAR SYSTEMS

8

THE COLOUR-COLOUR DIAGRAM AS A SELECTION TOOL

Our data's high resolution and depth allow us to study in detail the stellar structures present in the Coma cluster. Of particular interest are Globular Clusters (GCs), which can help trace the history of star formation and the cluster's general mass assembly. Usually, GCs are selected from monochromatic data, using only morphological parameters. In this chapter, the multiwavelength colour-colour (CC) selection tool is presented and compared with previous selection tools.

8.1 COLOUR-COLOUR DIAGRAMS IN PREVIOUS WORKS

Since its appearance in Muñoz et al. [130], *uiK* CC diagrams have been tested and used extensively to dissect light sources and select GCs in different environments at varying redshifts: from the most massive local clusters (the aforementioned Muñoz et al. [130] for Virgo and Ordenes-Briceño et al. [134] for Fornax) to other, less dense environments (Cantiello et al. [31] for NGC 253 and González-Lópezlira et al. [79] for NGC 4258). These diagrams are based on the *BzK* diagram presented in Daddi et al. [50], but with the focus put onto separating GCs from foreground stars and high-redshift galaxies instead of said galaxies. These diagrams are an appropriate tool given that photometric data for bulk objects can be obtained much more quickly than spectroscopy, especially for dim objects such as GCs. The long spectral baseline, from the near-UV to the near-IR takes advantage of spectral features like the 4000 Å break plus the redshifted spectra of distant galaxies to accurately separate between the different objects observed (see section 6.1 of Muñoz et al. [130] for a more detailed description and discussion of the *uiK* CC diagram).

8.2 AN ANALOG TO *uik* FOR COMA

Inspired by the results presented in these studies, we set foot to test if it was possible to extend fivefold the distance applicability of this tool: from the Fornax cluster at 20 Mpc, to Coma at 100 Mpc. We took advantage of existing optical data for Coma in the form of the Coma Treasury Survey and other programs mentioned in section 3.2 and build up from there. With the HST GO 14182 program, we tiled the central region of the Coma Cluster. Given that the IR channel of WFC3 does not extend as far to the infrared as the ground-based detectors used in the studies mentioned in the previous section (the

instrument has a sharp cutoff at around 1750 nm), *K* data is impossible to obtain. We then chose to observe in the reddest wide filter present in WFC3-IR, which is F160W. This filter is an analogue to the *H* band present in several ground-based instruments. Newly obtained data also included the F336W filter, analog to *u*, while archival data provided F475W (analog to *g*, also tested in Muñoz et al. [130]) and F814W (analog to *i*). In this context, we were presented with two concerns and challenges:

1. whether it is possible to use this CC selection tool at large distances, and
2. whether it is possible to use *H* band as an alternative to the *K* band

The distance concern relates just to photometric quality and depth of observations, in particular obtaining good quality photometry of a large number of GCs rather than redshift affecting the position of the sequences in the diagram: at 100 Mpc, the redshift of the Coma cluster is just $z = 0.0231$, so it would barely shift the objects in our diagram. The second concern is less worrying, given that the *K* band was used to separate GCs from stars and, as was mentioned above, there are not many stars in our survey footprint.

8.3 THE *uih* DIAGRAM FOR COMA

The archival raw data needed to complete the spectral coverage for our *uiH* diagram was downloaded from the MAST portal[1] in the form of `*_flc.fits` files and reprocessed using TweakReg[2] to put them in the *Gaia*-DR2 astrometric frame of reference, and then drizzled together using AstroDrizzle[3], both part of the DrizzlePac[4] software package [11]. The bias reference files for Coma Legacy Survey stacks had to be re-processed due to level offsets as mentioned in section 4.3 of C08 [see also 163]. Sources in the final stacks were analysed by SExtractor in a similar way to the one described in previous chapters. Once we had our archival data catalogues, we matched them with our new data using STILTS in `multimode=group` mode with a tolerance of 0.″4. As before, we tested for the best value of tolerance since, for larger values, the confusion was too high and the crowded zones got fewer matches. In the end, two matches were performed: one with tolerance of 0.″4 and one with tolerance of 0.″2. These two catalogues were then concatenated and an internal match with tolerance 0.″1 was performed to consolidate the matches. We present our first iteration of a *uiH* diagram for all the sources automatically SExtracted with good

1 https://mast.stsci.edu/portal/Mashup/Clients/Mast/Portal.html
2 https://drizzlepac.readthedocs.io/en/latest/tweakreg.html
3 https://drizzlepac.readthedocs.io/en/latest/astrodrizzle.html
4 https://www.stsci.edu/scientific-community/software/drizzlepac.html

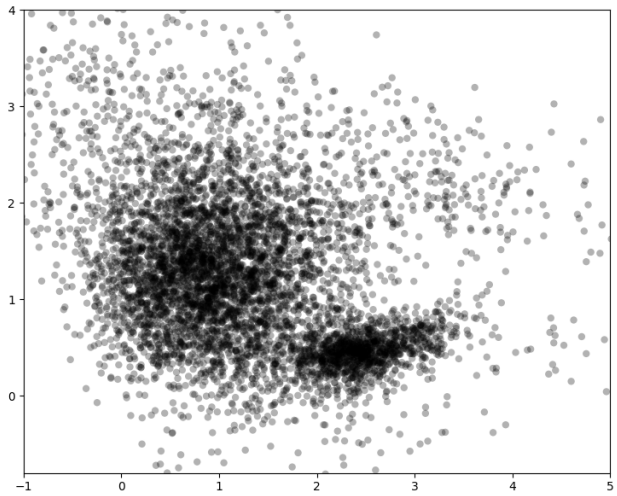

Figure 18: First iteration of our *uiH* diagram. Included are all the sources with well-measured MAG_PSF.

quality PSF photometry in all four filters but without the galaxy flux removed from the *H* images and matched from new and archival data in figure 18. Each point represents a source in our data. It is possible to identify two loci of objects clearly: an extended component centred around $\approx (1, 1.5)$ with a tail towards red values of $u - i$, and a compact, oblate component roughly aligned with $i - H \approx 0.5$. Similarities with the *uiK* diagram suggest that these components correspond with galaxies, both cluster members and background, and with GCs. These similarities can be tested with both morphological parameters and SSP model predictions. In figure 19 we show the same figure, but with four different parameters colour-coded: error in magnitude (top left), `SPREAD_MODEL` (top right), flux in the brightest pixel (bottom left), and effective radius (r_{eff}, bottom right). All of these parameters are given by SExtractor, and for all four, the median value across all filters has been selected. The thought process behind selecting these parameters is as follows:

1. **Δ mag** or magnitude error: as these objects have a medianed error of less than 0.05 mag, it can be inferred that its position in this parameter space is not due to errors and they actually populate this locus.

2. `SPREAD_MODEL`: this is a parameter given by SExtractor that measures how much a source deviates from the calculated PSF of the image. Values greater than zero mean than the object is more

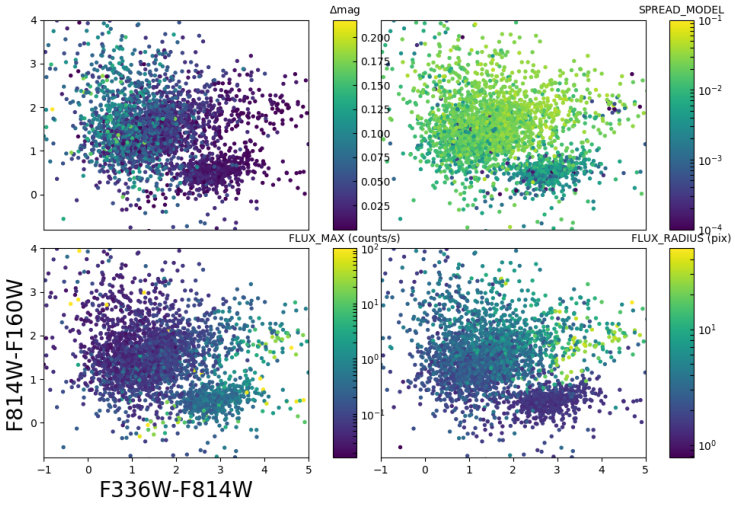

Figure 19: As figure 18, but with colour-coded morphological information: error in magnitude (top left), SPREAD_MODEL (top right), flux in the brightest pixel (bottom left), and effective radius ($r_e$ff, bottom right).

extended than the local PSF; negative values, the opposite: so it's highly likely that objects with negative `SPREAD_MODEL` values are spurious detections or cosmic rays. As these sources have low `SPREAD_MODEL` values but not the lowest, they mostly resemble PSFs but do not fix exactly that profile since they mostly occupy the middle range of the parameter values. This means that they are barely resolved. Points with lowest values are most likely stars, which ties with the next parameter.

3. `FLUX_MAX` or flux in the brightest pixel: we use this parameter to check which objects are most likely stars. These objects would then populate the stellar sequence expected in CC diagrams. In fact, we see on the order of ten yellows dots crossing the bottom right quadrant of the plot diagonally, hinting at the presence of a stellar sequence. Objects in the presumed GC locus do not have such high values of `FLUX_MAX`, and are therefore most like not stars. Note that this is where some of the points with the lowest `SPREAD_MODEL` values are present.

4. $\mathtt{r_{eff}}$: in a similar way to `SPREAD_MODEL`, we study this parameter to probe the compactness of our objects. In the presumed GC locus, we have effective radius on the order on one pixel, so these objects are extremely compact. Note that on the red tail of the galaxy locus we have mostly extended sources with $r_{eff} \gtrsim 10$. These object, cluster members, coincide with the passive galaxies locus mentioned in [130].

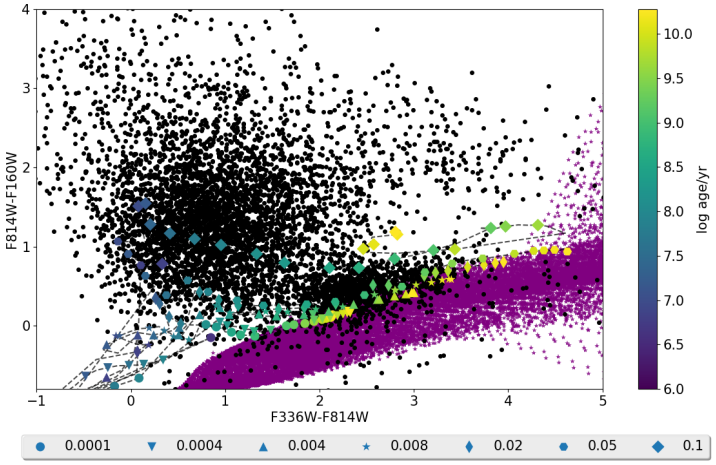

Figure 20: As figure 18 with the SSP tracks obtained with PÉGASE-HR and the stellar information given by the PHOENIX spectral library.

We conclude that these objects are most likely GCs or, more generally, compact stellar systems (CSSs) since there can also be nuclear star clusters (NSCs) or even ultra-compact dwarf galaxies (UCDs). This was further tested with the addition of two models: the PÉGASE-HR [110] model using BASEL 3.1 stellar SEDs [178] and the PHOENIX spectral library [93]. We build model spectra of single stellar populations (SSP) with the former, redshifting them before calculating magnitudes, transferring them to our CC space, and then doing the same with the synthetic atmosphere spectra. The result is shown in figure 20. From this plot, we can note several things:

1. The objects with the highest values of `FLUX_MAX` trace the stellar sequence suggested by the PHOENIX models. Consider that in figure 20 all of the atmospheric models available, even those with highly unrealistic parameters for stars present in the Milky Way halo (for example, $[\alpha/Fe] < 0.2$, unlikely since those stars were not born in an enriched medium). When those values are trimmed following what we can expect from the Besançon models, the stellar sequence becomes more streamlined.

2. The suspected GC locus is nicely bracketed by the SSP models in the y-axis. All but one of the models (the most metal rich) are crammed together in the blue end of $i - H$, but that is mainly due to axis scaling so the galaxies can be incorporated (see figure 3 for a plot with a relaxed version of the tracks). As expected, the higher the metal composition of a SSP, the redder its track in both axes. This is taken to the extreme with the $Z = 0.1$ track, the most metal-rich available, which is also the reddest in $i - H$.

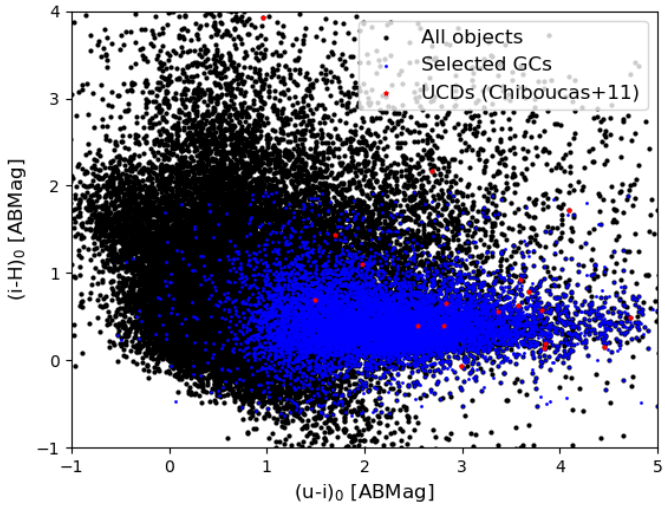

Figure 21: *uiH* diagram of all of the sources analysed with matched in all four filters. In black: all sources; in blue: selected GCs; in red: UCDs from Chiboucas et al. [38] matched with the full catalogue.

3. Both models have a non-negligible overlap, with the tracks spanning the same as all but one of the models at intermediate and old ages. This, again, is due to the use of *H* band instead of *K* band. This means that only using the CC diagram to select objects is just shy of perfect, and we have to consider adding other morphological parameters, like those shown in figure 19.

It is therefore highly likely that this locus is populated by GCs and other CSSs. Unfortunately, there is no spectroscopically confirmed GCs in Coma, so we cannot test the effectivity of our selection tool with such information. There is, however, spectroscopy data for UCDs as presented in Chiboucas et al. [38]. We have approximately 75% of those object in our survey footprint, and we performed a match between our full catalogue and the catalogue of Chiboucas et al.. From that match we can see that these objects populate primarily the GC locus of the CC diagram, extending towards redder magnitudes in the horizontal direction. These objects are shown with red markers in figure 21. This is in agreement with what was presented in Chiboucas et al. [38]. We will expand our analysis of these objects in the following chapters.

In the end, the requirement of having good quality PSF magnitudes in all four filters was too prohibitive and culled most (around 90%) of objects, the *u* band being the most restrictive as it is the shallowest and a good PSF model throughout the entire image cannot be trust-worthily built; and conversely *H* band is the less restrictive. We

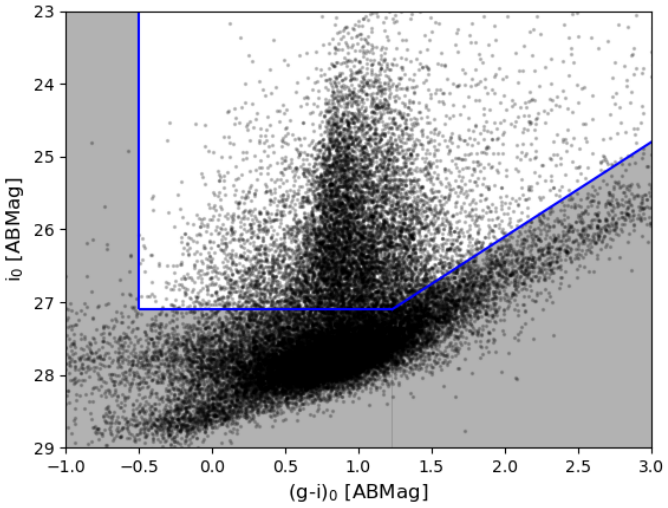

Figure 22: Photometric cuts performed in our GC selection procedure. Objects in the shaded regions were discarted.

use the newly added to SExtractor `MAG_POINTSOURCE` to construct out *uiH* diagram, precisely because out objects of study are point sources. In general, for compact sources this measurement of flux practically doesn't differ to `MAG_AUTO` or `MAG_APER` with an aperture three times as large as the FWHM of the point sources. We see in figure 21 the diagram constructed with `MAG_POINTSOURCE` for all sources in our survey with a match in the four filters. The evident separation between the two loci of objects mentioned above is not evident anymore, as it was introduced by the requirement of having well measured `MAG_PSF` mentioned above, which kept mostly unresolved objects (GCs and unresolved background galaxies). We still used the *uiH* diagram as a test ground for our selection procedure, which included photometric and morphological cuts:

1. Photometric cut: from our combined data we constructed a *g-i* colour-magnitude diagram for all sources, which is shown in 22. We isolated candidates in the typical GC locus and past the GCLF-TO magnitude, but before the distribution is dominated by background sources. The cuts made were:
   - $i \leqslant 27.1$
   - $-0.5 \leqslant g - i$
   - $i \leqslant 28.7 - 1.3 \times (g - i)$
2. Morphological cut: since we expect GCs to be compact, we then studied the distributions of parameters like `A_IMAGE` (semi-major

axis), FLUX_RADIUS and FWHM_IMAGE in all filters to filter only compact objects which already met the photometric conditions imposed above. The morphological conditions are:

- "Quality control" cuts: we require FLUX_MAX> 0 in all filters to ensure that detections were not spurious or cosmic rays.
- As Peng et al. [138], we use the *i* band as our reference for morphology. We limit the FWHM_IMAGE to be less than 5 pixels in that band. This naturally restricts the FWHM range in all other filters, ending up with around 90% of objects with FWHM less than 5 pixels in all other bands. This relaxed cut allows for slightly larger objects, like NSCs, to be included in our analyses.
- FLUX_MAX < 5 counts per second in all filters, to avoid the handful of stars that we expect in our footprint.
- SPREAD_MODEL > -0.02 in the *g* and *H* band. These were the filters where there were more detections with well-measured PSF magnitudes, and therefore the PSF was well measured. The value of -0.02 and not zero allows to slight variations in the quality of the measured PSF.

After each cut, we looked at the distribution of selected sources in our *uiH* diagram to see if they actually populate the GC locus and if there were strays in other regions of the diagram. We ended up with a collection of 9165 points grouped in and around the GC locus, with an average $u-i$ colour of 2.25 mag and an average $i-H$ colour of 0.45 mag. Some objects were far off the GC locus, so we applied a final colour cut of $-0.8 \leqslant u-i \leqslant 6$ and $-0.7 \leqslant i-H \leqslant 2$. This final selection is highlighted in image 21.

8.4 COMPARISON WITH OTHER SELECTION TOOLS

Studies of GCs based in photometric data in the previous decade have been heavily influenced by the selection tool presented in Peng et al. [138]. It relies on the high resolution of ACS and in the radial light profile of GCs to separate them from background sources using a concentration index C_{4-10}, defined as the difference in magnitude when measured with an aperture of 4 pixels versus 10 pixels in diameter, plus a colour and magnitude cut (see section 2.4 of Peng et al. for further details). This technique has been reproduced in other GC studies in Coma [44, 113, 137, 174, 6], albeit with slight variations or additions. We show in figure 23 how the C_{4-10} concentration index compares with our selection tool. 4049 objects are identified as GCs with this technique, from which 3655 are in our selection. We see that our objects (blue dots) group prominently around $C_{4-10} = 0.45$, the median value as mentioned in Peng et al. (left panel), and, conversely,

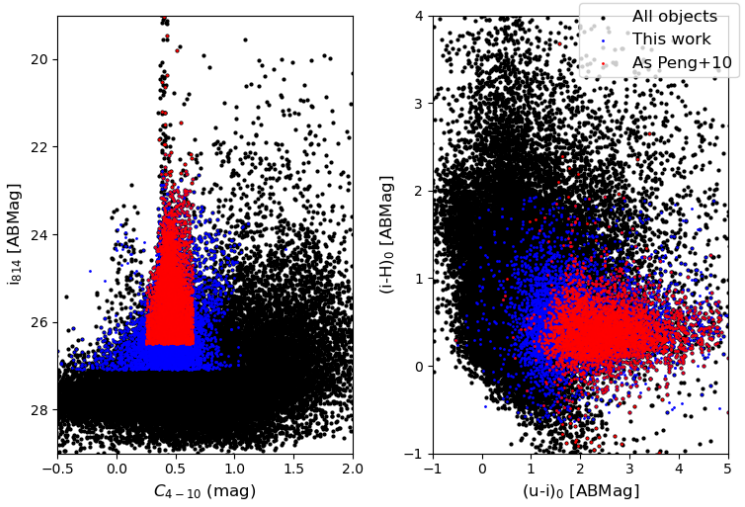

Figure 23: Comparison of the selection procedure used in this research (blue dots) and the selection procedure introduced in Peng et al. [135] (red dots). Left, concentration index versus i band magnitude; right, *uiH* diagram.

the objects selected via the compactness method fall into the GC locus in the *uih* diagram (right panel). Our data was cut at a deeper magnitude, $i = 27.2$ mag, 0.7 mag deeper than the data of Peng et al.. The most blue objects in the GC locus of the *uiH* plot are precisely the dimmest, so it's only natural that objects selected by compactness are on average redder. Choosing objects more or less concentrated can account for GCs in different states of relaxation, variable background (important for NSCs) or more extended objects like UCDs. The crossmatch between the Peng et al. catalogue and our catalogue was performed, but due to wildly different footprints, we decided not to compare these two. Nevertheless, when matched with our full catalogue of objects, their GCs populated the GC locus in the same way that is shown in figure 23.

While the concentration index may be useful when having less than three passbands, using a CC diagram for reference improves the quality of the selection. There is, of course, the pitfall of having to detect the object in all three filters simultaneously[5]. Other issue with this method is the massive amount of IR flux coming from the galaxies in our survey, mostly being late-type. The galaxy light removal mentioned in section 6.3 helps to overcome this problem, since we saw that most of the sources were lost when matching due to being undetected as they were drowned in the galaxy flux.

5 *At least* three filters. Since there is a good amount of previous literature that uses $g - i$, the *g* filter has to be added to the mix as well

9 THE GLOBULAR CLUSTER SYSTEM OF COMA

Having selected our sample of GCs from the CC diagram and with the addition of morphological information, it is possible to study the scaling relations present between the parameters of the GCs and the environment in which they are found.

9.1 COLOUR AND MAGNITUDE OF GCS

9.1.1 *Magnitude distribution of GCs*

First, we study the magnitude distribution of our selected GCs. Figure 24 shows the magnitude distribution from our sample in all available passbands. We see that the distributions for g, i and H seem to be mostly well-defined and completed, given that their peak is at magnitudes brighter than the 50% completeness limit, which are shown as a black dashed line. The only exception is u, being the shallowest band. For u, i and H the GCLF-TO magnitudes is shown with a solid red line. For u and H, this was calculated in section 5.3 from local sources; for i the value of 25.5 mag is taken from Madrid et al. [119].

9.1.2 *Colour distribution of GCs*

Next, we study the colour distribution of our sample of GCs, which we show in figure 25. All possible contiguous colour combinations were plotted. These distributions cannot be described effectively with a single component model, so we fitted them with a Gaussian mixture model (GMM) with three components. We chose three because it minimises the Akaike Information Criterion (AIC). To see if these distributions are physically related, we also show in figures 26, 27 and 28 all the possible CC diagrams of our sample as 2D KDEs. It can be seen that some of the peaks found using the GMM correlate to the CC diagram, the most clear being *gih* space in figure 28. In that figure, we see that the distribution has its main peak at $\approx (0.9, 0.3)$ and that even with a secondary peak missing, the asymmetry of the distribution towards redder colours (top-right region of the plot) indicates a secondary population, possibly indicated by the peaks crossing at $\approx (1.1, 0.4)$. Such an asymmetry can be seen less prominently in *ugi* colour-colour space (figure 26): in this case, the distribution is skewed from its main peak towards blue $u - g$, but red $g - i$ (top-left region of the plot).

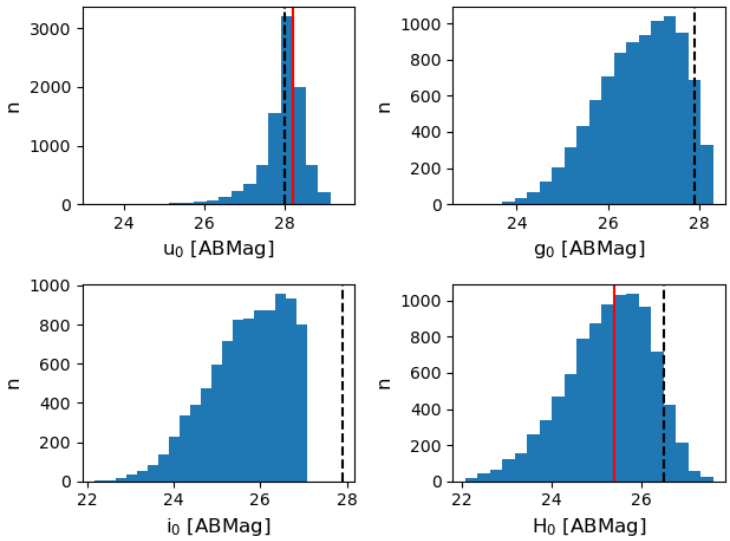

Figure 24: Magnitude distribution of our selected sources. Blue histogram: distribution; black dashed line: 50% completeness limit; red solid line: GCLF-TO magnitude.

9.1.3 *Colour-magnitude diagram of GCs*

The final purely photometric analysis performed was studying the colour-magnitude diagram (CMD) of our GCs. In figure 29 we show all possible CMDs constructed with contiguous colours. The sharp cut-offs in the distributions come from the photometric cut that was mentioned in the previous chapter.

9.2 SPATIAL DISTRIBUTION

9.2.1 *General spatial distribution*

Figure 30 shows the spatial distribution density of all our our selected GCs as a 2D KDE. The distribution mostly centered around NGC 4874 with a secondary peak around NGC 4889. This coincides with what was found in Peng et al. [138] and Madrid et al. [119]. The dips in the distribution coincide with the spacing in the IR mosaic of the survey., except towards the southeast: there we hit a zone of lower density of objects, as was also shown in those two papers. In the next section we see how this distribution varies with colour.

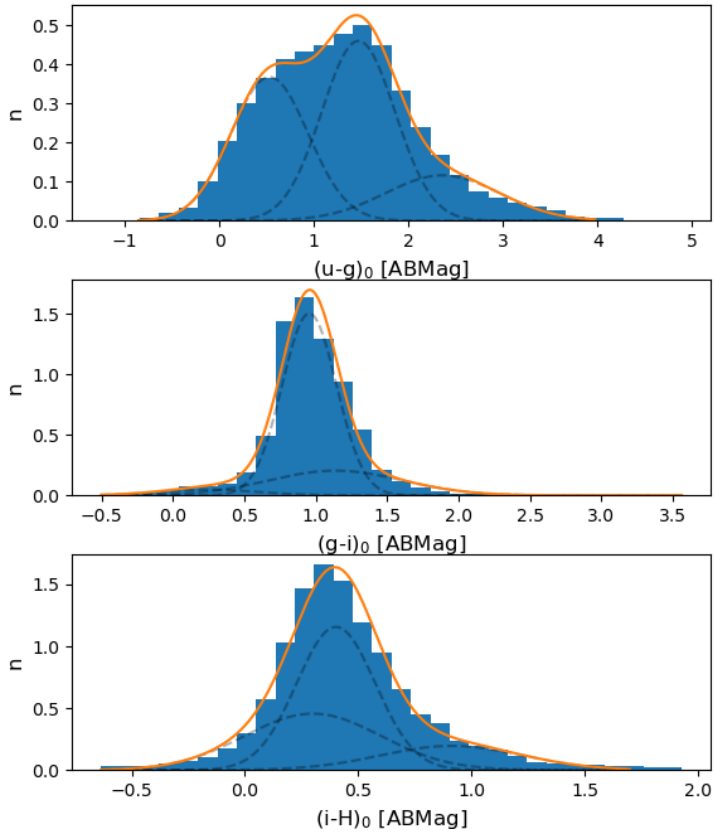

Figure 25: Colour distribution of selected GCs in the three possible contiguous colours. Data is shown as a histogram (blue bars) and a Gaussian mixture model (orange solid line) with three components (dashed gray line)

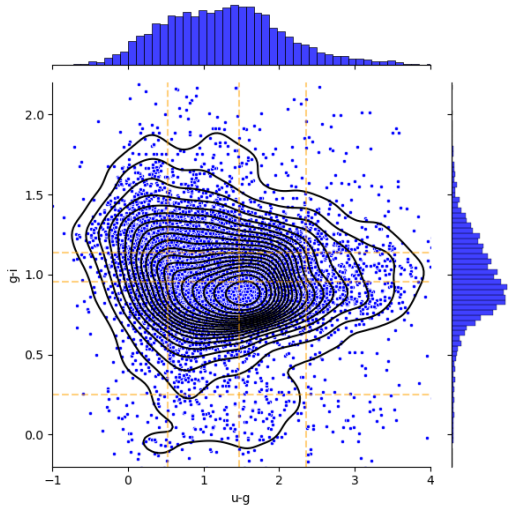

Figure 26: Colour-colour distribution of selected GCs. $u-g$ vs $g-i$ are shown in blue squares and in black 2D-KDE; marginal distributions are shown along the axes. The peaks of the GMM of figure 25 are shown as orange dashed lines.

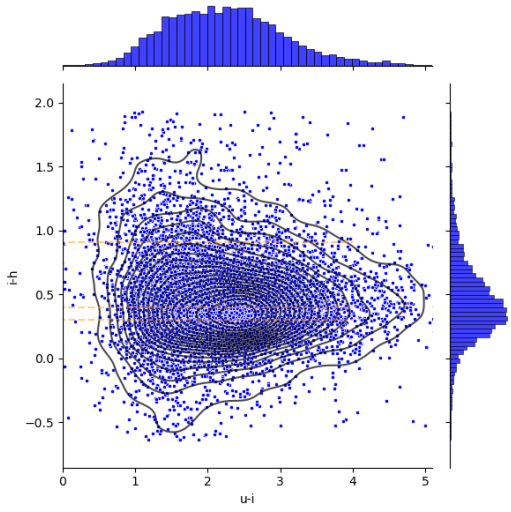

Figure 27: Colour-colour distribution of selected GCs. $u-i$ vs $i-h$ are shown in blue squares and in black 2D-KDE; marginal distributions are shown along the axes. The peaks of the GMM of figure 25 are shown as orange dashed lines.

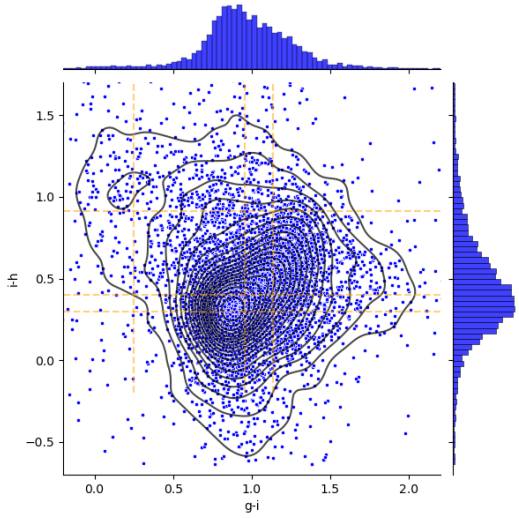

Figure 28: Colour-colour distribution of selected GCs. $g - i$ vs $i - h$ are shown in blue squares and in black 2D-KDE; marginal distributions are shown along the axes. The peaks of the GMM of figure 25 are shown as orange dashed lines.

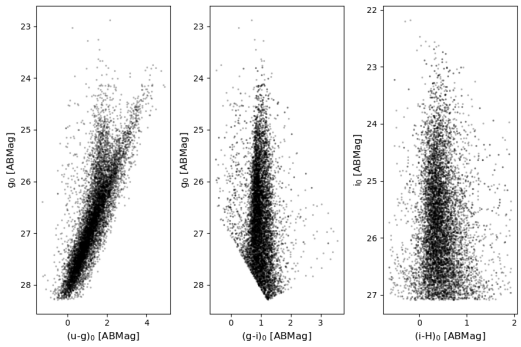

Figure 29: Colour-magnitude diagrams of selected GCs. Left: $u - g$ vs g; middle: $g - i$ vs g; right: $i - H$ vs i.

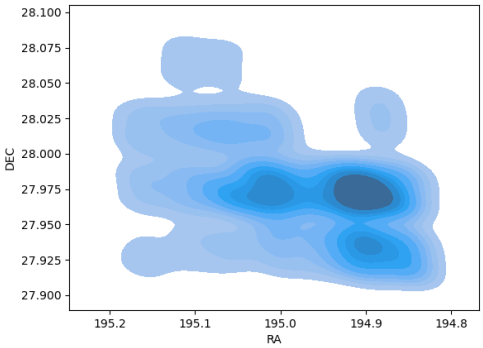

Figure 30: Spatial distribution of selected GCs as a 2D KDE

9.2.2 *The blue and red population*

From our colour distributions shown above, we can study their separate spatial distribution. We test both the Peng et al. and Madrid et al. approaches: splitting by distance and by colour.

1. When creating the subsets by distance to NGC 4874, as Peng et al., we split the population of GCs in three: a "galactic" population, less than 50 kpc from NGC 4874; a "distant" population farther than 130 kpc, and the "in between". At Coma distance, the scale is roughly half a kpc for each arcsecond: one arcminute equals 29 kpc. This translates to distances less than 1′.724, more than 4′.48, and in between. The $g-i$ colour distribution of these three subsets is shown in figure 31. The "galactic" and "distant" populations follow very closely the distributions shown in figure 8 of Peng et al., with some minor differences: for instance, the red peak of the inner population is not as obvious, but there is a skew which indicates that the population exists.

2. When creating the subsets by colour, as Madrid et al., we found that our distribution does not go as far in the red as their distribution: their distribution peaks at $g-i \approx 1.5$ mag; in our catalog, only 10% of the sources are redder than that, even considering our wide colour cut (see figure 22). Sources redder than that fall into the locus of background, unresolved objects. In the following chapters we present some scenarios that may cause this discrepancy. Still, if we trim the distribution to the limits of Peng et al. ($0.5 \leqslant g-i \leqslant 1.5$) we can see that it's nicely fit by two Gaussians with peaks of $(g-i)_1 = 0.85$ mag and $(g-i)_2 = 1.17$ mag. Figure 32 shows the distribution and the GMM fit. If we split the population at the intersection of these Gaussians ($g-i = 1.03$ mag, a bit redder than the average of the

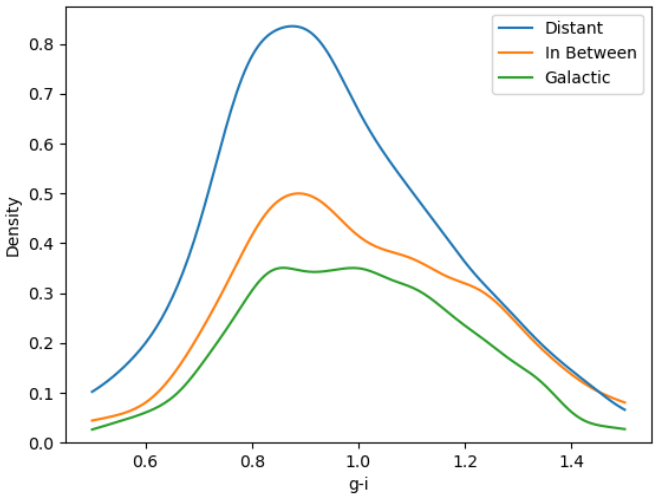

Figure 31: Distribution of the $g - i$ colour for three subsets of GCs defined by distance from NGC 4874

peaks) we can study the spatial distribution of our red (5153 objects) and blue (3131 objects) population, which is shown in figure 33. We see that the blue component is more extended than the red population, and there are some overdensities which do not coincide, most notably around NGC 4906 or in the northernmost tiles. The main overdensities are truncated: for NGC 4874 by the gap between two IR pointings; for NGC 4889 because of a slightly rotated archival pointing. In the following chapter we present some scenarios which could cause this distribution.

9.3 DERIVED PROPERTIES

Having access to synthetic stellar population models allows us to derive properties from our sample of GCs. In this study we use PÉGASE-HR [110], that work over the BASEL 3.1 stellar SEDs [178]. As mentioned in the introduction, we redshifted the generated spectra to the Coma redshift and then obtained the colours. The software and set of SEDs were chosen over other alternatives due to practicality and widespread use, but we note that different models may lead to different results [148]. With these results in hand, we assigned each datapoint an age and metallicity from this grid using the RMODEL algorithm [33][1], which takes into account the errors in magnitude as provided by SExtractor and propagates them to errors in the derived

1 https://rmodel.readthedocs.io/en/latest/

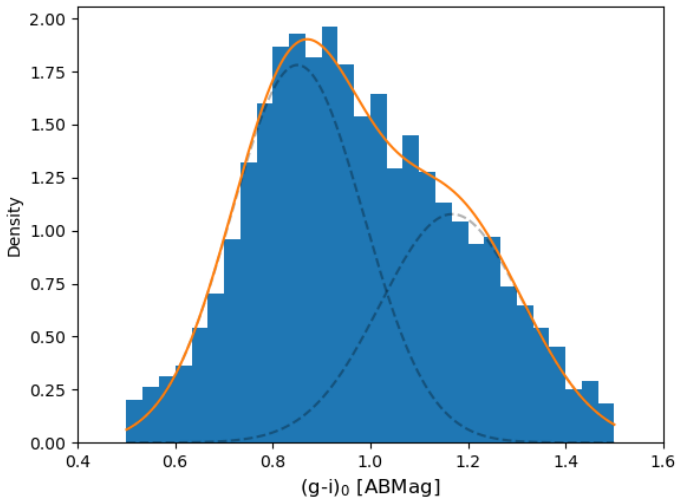

Figure 32: Distribution of the $g-i$ colour for all our GCs in the range $0.5 \leqslant g-i \leqslant 1.5$. The orange solid line shows a Gaussian mixture model fit with two components, each individually shown in dashed gray lines.

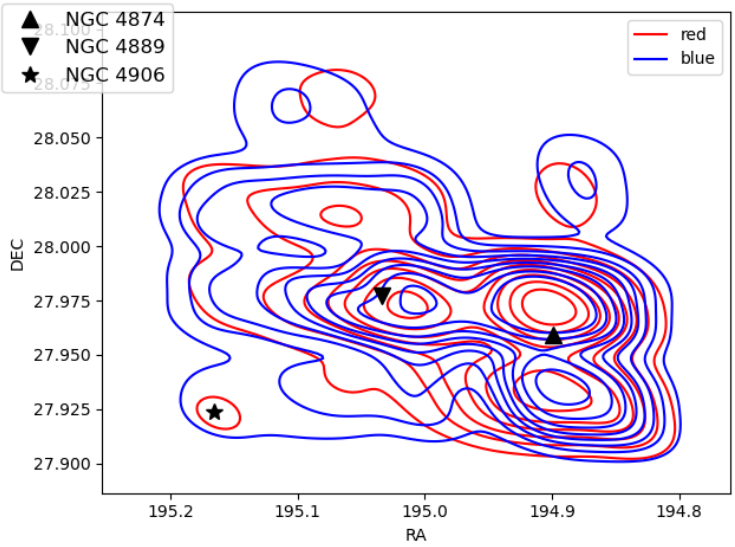

Figure 33: Spatial distribution of the two populations of GCs as defined by $g-i$ colour following figure 32.

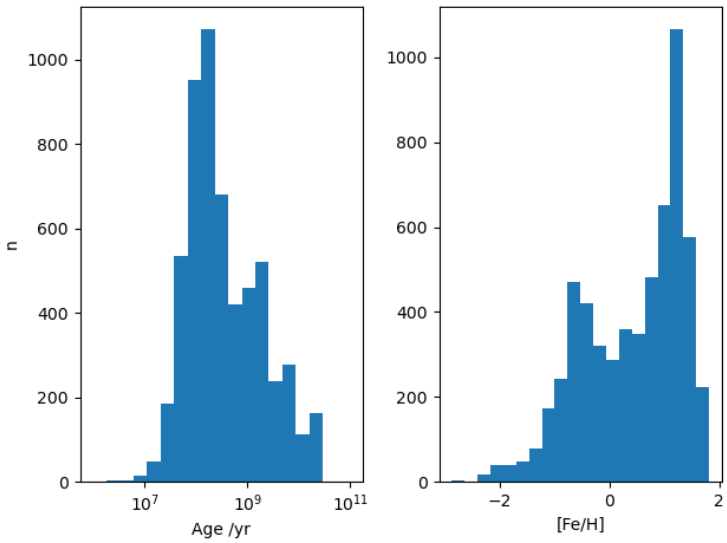

Figure 34: Derived age and metallicity distributions for a subset of GCs which are inside the limits of the PÉGASE models

parameters. With these propagated errors we can see how our values are affected by errors in photometry before analysing them. The derived errors are calculating via a Monte Carlo method by obtaining the parameters of datapoints that follow a Gaussian distribution using the errors in the input. Errors are then given as 1-, 2- and 3-σ values from the median value. We show in figure 34 the derived age and metallicity distributions of all objects within the limits of our model grid (5849, or 60.8%) and proceed to dissect them in the following subsections. Note that this is the first time that ages and metallicities are derived for globular clusters in Coma.

9.3.1 *Age*

As mentioned above, the derived parameters are model dependant, and in particular ages are typically calculated biased towards the lower part of the available parameter space [148]. For this reason, we do not assume these ages as being absolutely correct, but rather *relatively* correct, meaning that objects with young ages, like one million years for some of the objects in our sample, are not necessarily that young, instead being younger that objects with a derived age of one billion years. We will refer to the derived ages and metallicites anyway when describing the distributions.
The age distribution has a sharp rise, a main peak at 200 Myr, and a slow decline towards old ages with lesser peaks at around 2, 7 & 20 Gyr, the old age limit of our model. This indicates that the majority

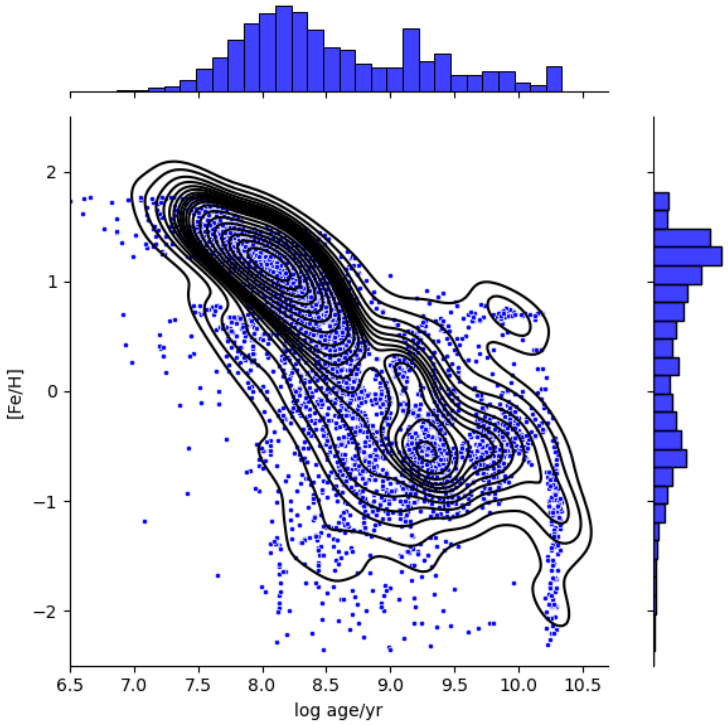

Figure 35: Derived age and metallicity combined distribution, shown as blue squares and as a 2D KDE. Along the axes are the marginal distributions, which are identical to the ones shown in figure 34

of the GC population in Coma is relatively young, a fact that may be supported from the $g-i$ colour distribution shown above. Note that the $g-i$ colour **is not explicitly included** in our RMODEL calculations. In the following subsections we study if there is a correlation or not.

9.3.2 *Metallicity*

For the metallicity we take the same approach of considering *relative* metallicities rather than absolute ones, but still will refer to the obtained values to describe the distribution. The metallicity distribution seems to be bimodal, conformed by a distribution peaking at [Fe/H]≈ -0.5 dex, the other one peaking at [Fe/H]≈ 1.2. The classic separation of old and metal-poor, and young and metal-rich may be considered if it shows in a bivariate plot of the data – see below.

9.3.3 *The Age-Metallicity relation*

Figure 35 shows the age-metallicity relation for the points in our sample. There are two main sequences in this plot: the young-age centered at the metal-rich, young-age peaks described above, and the old-age, centered at the 2 Gyr age peak and the metal-poor peak. There is a third, less prominent sequence of the objects of age $\approx$ 2 Gyr. None of these sequences appears to be the continuation of one another, and in all the average behaviour is the same: as GCs get older, they also get more metal-poor. This bifurcated relation was found for MW GCs by Leaman et al. [111], and from a technical point of view this may be expected to be found here as well, since the SSP models are based on MW GCs. From an astronomical point of view, there is evidence that Coma underwent recent merger activity, between one to two Gyr ago [29, 96, 95], which may have sprouted both GC stripping from galaxies or new GC formation (or maybe both). There's also an interesting population at around 6 Gyr and 0.6 dex, fairly old but quite metal-rich. Different scenarios are discussed in the next chapter.

9.3.4 *Spatial distribution of age and metallicity*

Since it was already established that there were trends in colour in the spatial distribution of our GCs and there were some relations between colour, age and metallicity, we study now the relation between these last two and spatial distribution, using both the spatial criterion by Peng et al. and the colour separation inspired by Madrid et al.:

1. Separate by distance: the three populations and their age-metallicity distributions are shown in figure 36. There is no major perceptible difference in the overall distributions, only a hint that the old, metal rich population mentioned above is more present in the distant population.

2. Separate by colour: the blue and red population and their age-metallicity distributions are shown in figure 37. In this case a difference can be seen by looking at the marginal distributions: the old, metal-poor peak is less prominent in the red population, and conversely more prominent in the blue population, which follows more closely the overall distribution. Still the majority of both blue and red GCs fall in the young metal-rich population.

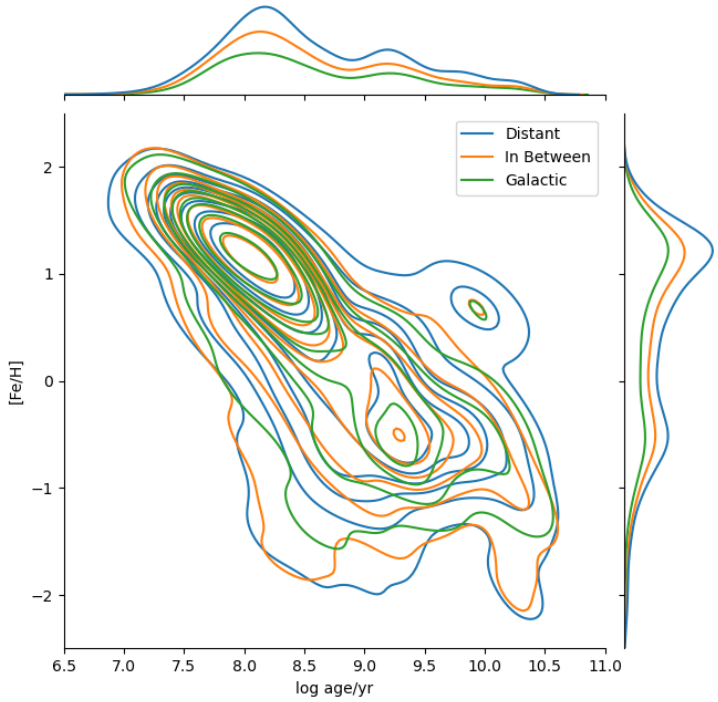

Figure 36: Derived age-metallicity distribution of the three sub-populations of GCs separated by distance to NGC 4874.

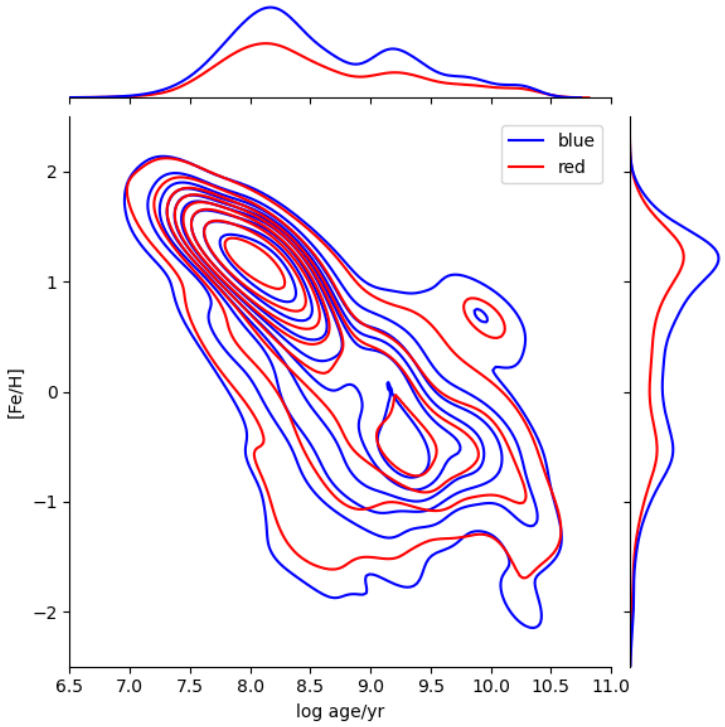

Figure 37: Derived age-metallicity distribution of the two sub-populations of GCs separated by $g - i$ colour.

Part IV

DISCUSSION

10 ANALYSIS

We proceed to analyse the results shown in the previous chapters

10.1 THE GLOBULAR CLUSTER SYSTEM OF COMA

Our catalogue of 9165 GCs and other CSSs is complete past the GCLF-TO magnitude in three of our four filters. Only for the shallow u band the 50% completeness limit is in a magnitude brighter than the TO magnitude. Therefore, we can confidently say that our analyses describe well the CSSs population of the central region of Coma, despite having some holes in our distribution due to the IR pointings and archival mosaic. Most of this population comes in form of IGCs, which are not bound to individual galaxies but to the cluster itself. These IGCs are mostly blue, while the GCs associated with galaxies are redder, in particular those associated with NGC 4874. This galaxy was key in the analysis of Peng et al. [138], due to it being in the Coma Legacy Survey footprint. Archival data for NGC 4889 was later added, so it could be added to the analysis of Madrid et al. [119] or what is being presented here. Thanks to our extended spectral coverage towards the near-UV and near-IR, we can use an improved selection tool in the form of a colour-colour diagram and derive age and metallicity from models with the lowest amount of uncertainty and degeneracy possible. We found that these IGCs follow a bimodal age-metallicity relation, with most of them being relatively young and metal-rich. From what can be seen in figure 37, a single colour **does not** correlate with metallicity in this case: it could be expected that the two colour populations correspond to the two age-metallicity populations, but the relation is more complex than that. In fact, the blue population does not correspond to neither the young, metal-rich population (expected because they are young) nor the old, metal-poor population (expected because they are metal-poor), only showing that the old, metal-poor population is more prominent in the blue GCs than in the red GCs. Perhaps if we had the extremely red GCs of Madrid et al. we could have a more noticeable bimodality, but in our case due to the addition of the u band we are unable to detect such red objects.

10.2 STAR FORMATION HISTORY IN COMA

Having such a high number of young, metal-poor GCs in our sample roaming in the gravitational potential of the cluster is an indicator that there was a recent event that triggered the formation of a mas-

sive GC population. It has been proposed that Coma is a post-merger cluster [29, 95, 45] on photometric and dynamical bases. Burns et al. [29] mention that the NGC 4839 group, currently towards the south-east of Coma, has passed through Coma ≈ 2 Gyr ago, while Jiménez-Teja et al. [95] indicate a merger less than 1.2 Gyr ago. This coincides with their intra-cluster light (ICL) large contribution of late A and early F stars, which they claim were stripped from infalling galaxies or disrupted dwarfs, although this later scenario is dismissed by Peng et al. [138]. Taking into account the evidence for a recent merger, it is tempting to propose the idea that most of these IGCs were formed **during** the merger from the free gas in the cluster and in the NGC 4839 group. Both the cluster and the group may have been rich with hot gas when they were merging, and the ram pressure formed GCs around galaxies (see Lee et al. [112] for Virgo and Roberts and Parker [155] for Coma), the star formation got quenched quickly, and then these cluster were stripped. Note that no assumption is being made on *when* these clusters were formed since, as discussed in the previous chapter, these ages have to be taken as relative ages instead of absolute, and same with metallicities. Unfortunately for this scenario, recent observations prove this idea wrong: the ICL stellar populations show ages older than 6.7 Gyr and more metal poor than $[\mathrm{Fe/H}] = -0.6$ [82], supporting the idea that the material forming the ICL (stars and IGCs) comes from disruption of small galaxies or tidal stripping of large galaxies.

10.3 COLOUR-METALLICITY RELATIONS

It is widely assumed that, regarding GCs, colour can be used as a proxy for metallicity: bluer colour indicates lower metallicity for a given age. Therefore, this relation is used mainly for old GCs. We do not find such a relation for our GCs: two colours are needed are needed to fully grasp the degeneracy of the age-metallicity relation and the extension of colors to the near-UV and near-IT to maximally reduce it. Further analysing the data neither shows that the opposite is true: selecting GCs by derived age or derived metallicity shows no significant differences in the distribution of the colour of GCs. Certainly this may be caused by a systematic error introduced by the models and in the deriving of the parameters, so one of the things to keep in mind in the future is to test different models to see if similar results can be recovered. Nevertheless, all of those models have been created and calibrated around MW GCs and will all show the same pitfalls that were exposed in Powalka et al. [148].

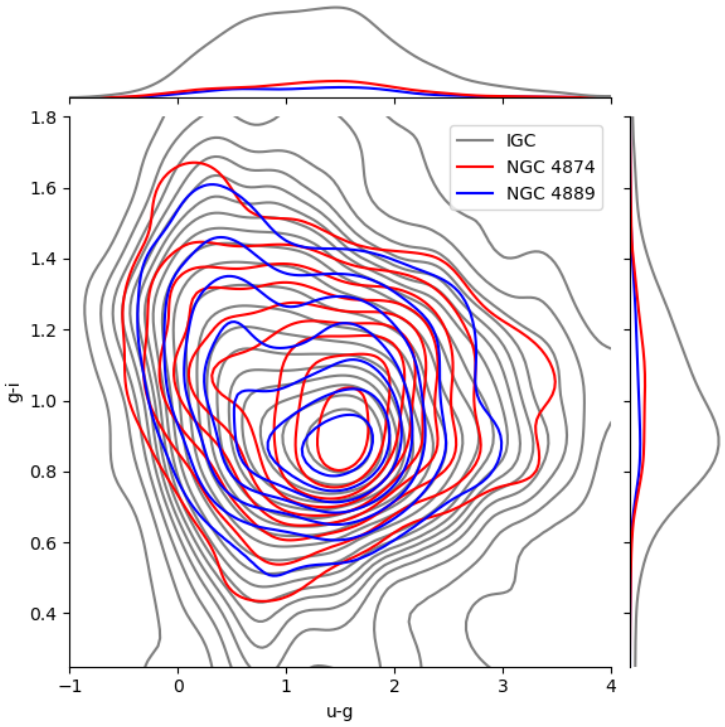

Figure 38: ugi CC distribution of GCs from the vicinity of NGC 4874, NGC 4889, and IGCs

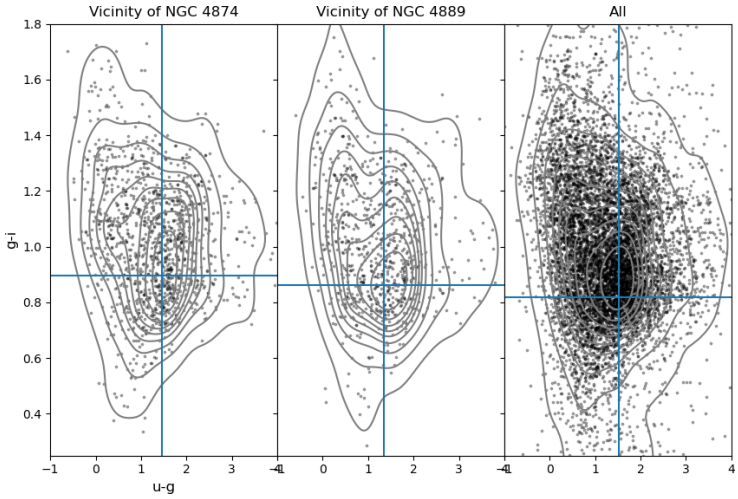

Figure 39: Comparison of the *ugi* CC distribution for the subsets defined above. The approximate peaks of the 2D distribution are shown as light blue lines

10.4 COLOUR-COLOUR RELATIONS AS A FUNCTION OF ENVIRONMENT

In Powalka et al. [147] it was shown that CC relations for GCs in Virgo are slightly different when selecting GCs from different environments: near M87, in a ring around the galaxy, far from the galaxy, and around some minor galaxies. Their results show that for the GCs nearest to galaxies, the CC relation is tight, while being more disperse farther from the galaxies. They also have bluer colours for distant GCs, as as presented here. This similarity motivated the execution of an analogous analysis, considering the GCs in the immediate vicinity of NGC 4889, NGC 4874, and all of the other clusters. We show in figure 38 the compared distribution of the *ugi* colours for GCs within a distance of 80 kpc (78.″7 arcsec) of NGC 4889, NGC 4874, and clusters outside of this radius. The individual distributions are shown in figure 39. There is a noticeable offset in this CC relation for GCs in this dense environment, affecting its shape and peak. We find the same overall trends: a well-defined CC relation for clusters in the bottom of the potential well, which get fuzzier and bluer once we move outwards. This behaviour is observed when using visible bands g and i, but is not evident if we use the *uiH* CC plane instead of *ugi* (figure 40), something also noted by Powalka et al.: otherwise, the CC selection tool won't be useful, and in particular for their case, given that the GC locus is more tightly defined in a *uiK* diagram. We have seen that there are no major trends of derived age or metallicity with colour or spatial distribution, so the same conclusion is drawn: there

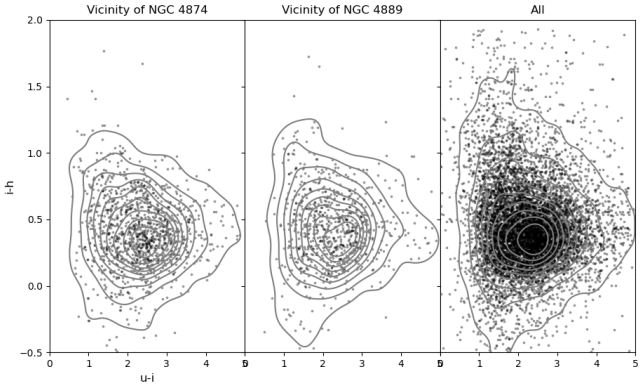

Figure 40: Same as figure 40, but for *uih* CC space.

is something fundamentally different in the chemical abundances of these clusters which is given by their environment. In the case of Coma, since IGCs were stripped from galaxies, its differences in the formation processes of the parent haloes of these galaxies as compared to process of chemical enrichment of the host galaxies. Since we are speaking about some of the largest galaxies in the nearby Universe, their star formation history started very early, has been violent and chaotic and could have led to skewed chemical distributions as compared to the surrounding gas. In the dark matter haloes in which, say, NGC 4889 was going to form, there was a large amount of gas infalling. This gas formed supergiant stars that exploded as Type II Supernova very quickly, enriching the environment before the central super-massive black hole turned on the AGN mechanism. When turned on, feedback may have caused a single burst of star and GC formation, after blowing the remaining available gas. Other GCs later accreted, which would become IGCs, were formed in less dense environments, so their enrichment process was different. Future spectrographs on large next-generation telescopes, such as ELT, TMT and GMT, will be able to directly measure the chemical abundance patterns of these GCs and illuminate this discussion and advance our understanding of the formation of these supposedly first GC generation in the Universe.

10.5 THE SELECTION TOOL

The *uiH* CC plane proved powerful to *aid* in the selection process of GC candidates, given that there was too much degeneracy between the GC locus, the cluster members and the background galaxies. Given that we manually input a series of conditions on what we *expect* from GCs, what we ended up performing was a brute-

force unsupervised learning algorithm with many dimensions. One improvement that can be tested is creating a "modified" *uiH* plane that includes some morphological parameter over the color axis, like the one implemented in Powalka et al. [146]. Such an improvement would allow to select GCs using an unsupervised algorithm with few dimensions, using some colour cuts, or it may even allow to do a free-hand selection of GCs as cleanly as possible.

It was shown in figure 21 that our selection tool also can select UCDs and, in fact, objects brighter than $g = 23.5$ mag may as well be all UCDs as per the middle panel of figure 29. But the *uiH* diagram alone may not be useful to detect NSCs, at least the ones in bright galaxies, due to SExtractor limitations: the software cannot dissect the components of an object and it will detect the whole galaxy as the object. We wanted to put this to the test and try a workaround. We matched the NSC catalogue from den Brok et al. [54] with our data. Their catalogue was built using visual inspection and fitting the galaxies to remove the galaxy light, leaving only the central object. From their catalogue of 198 objects in the Coma Legacy Survey, we match 28 in our data. Since SExtractor cannot identify the NSCs as an independent object from the host galaxy, it's no use to plot these matches in a *uiH* plot, because they do not populate the GC locus, even when using `MAG_POINTSOURCE`[1]. Instead, we used the parameter `FLUX_MAX` as a "zero-pixel"[2] aperture and constructed the *uiH* plot with these magnitudes. The resulting plot is shown in figure 41. The NSCs share the GC locus with our selected objects, but on average occupy the reddest part of the locus, in both colours. This may well be the consequence of being immersed in the light of the host galaxy, most likely an early-type galaxy, so the NSC colour would be biased towards the red. This aspect requires a dedicated morphological decomposition analysis for all cluster galaxies and is beyond the scope of this work.

10.6 THE GLOBULAR CLUSTER LUMINOSITY FUNCTION

From figure 24 we see that our GC selection is mostly complete in visible and infrared magnitudes, while the *u* band distribution hits a peak right at the 50% completeness limit. The magnitude distribution for the other filters can be fitted with a Gaussian to obtain the parameters of the GCLF, given that those functions follow a Gaussian shape (an empirical result instead of a physical one, as recounted by Richtler [154], Rejkuba [152]). The GCLF is obtained by fitting the distribution with a KDE using a Gaussian kernel, which is then re-

1 An altenative is to use proper aperture magnitudes with a small aperture and a well defined annulus for background subtraction, but sequences in the *uiH* plot become more messy with the use of those magnitudes

2 Actually, one pixel

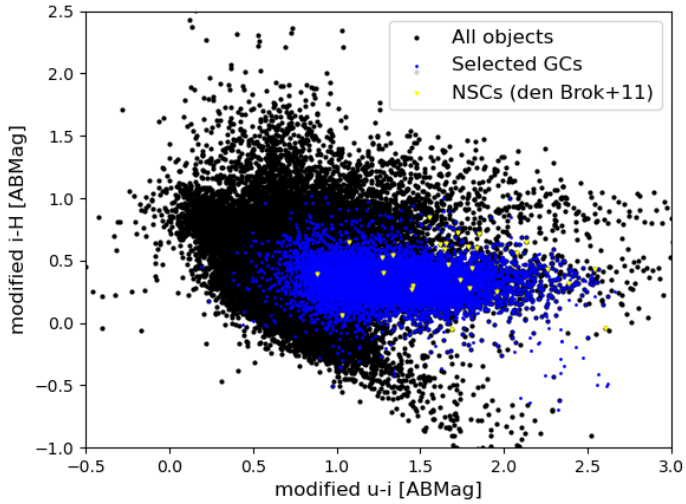

Figure 41: Modified *uiH* plot with "zero-pixel" apertures. Included are the GCs selected for this work and the matched NSCs of den Brok et al.

flected around the highest point. The distribution and fits are presented in figure 42. In the legend, the μ values of the Gaussian distributions are presented, which can in turn be taken as the GCLF-TO, although with some precautions: note that the 50% completeness limit is only 0.6 mag deeper than μ for the g band, and the dropoff in completeness is quite steep, from 80% to 0 in a range of around 1.5 mag, or -53.3% mag^{-1} . Therefore, the actual distribution may peak at a lower brightness level since there may be a percentage of GCs slightly dimmer than the peak magnitude which we are not automatically detecting. This means that the value of $\mu_g = 27.27$ mag is only a lower limit for the GCLF-TO in the g band, but it should not be more than 0.3 mag dimmer, similar to our random error. For the case of the H band, we have a much more flat gradient of completeness-magnitude in the magnitude range spanned by the GCs, at about -3% mag^{-1} up to $H = 26$ mag, but then dropping off, reaching -24% mag^{-1}. This means again that the value of $\mu_H = 25.76$ is a lower limit, but the actual value should not be more than 0.3 mag dimmer, again in well agreement with our $1-\sigma$ random errors. The cited previous value of 25.24 mag was calculated in section 5.3 following the GCLF of confirmed members of the GC system of Andromeda [176]. The Andromeda GC system shows internal variations in their GCLF, which Barmby et al. [14] argue can be caused by age, metallicity or IMF; these same parameters can cause the difference in the measured values. By far the most complete is the i band, with

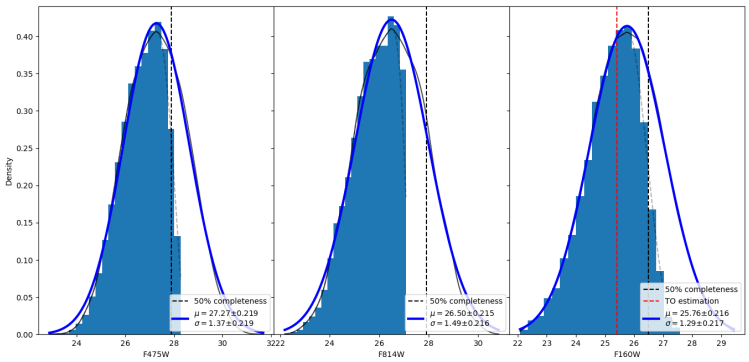

Figure 42: Magnitude distribution and fitted Gaussian for the g, i and H bands. The distributions are shown as a light blue histogram and as a KDE with a Gaussian filter with a gray dashed curve; the solid gray curve shows the reflected KDE. As in figure 24 previous values of the GCLF-TO are shown as a red line and 50% completeness limit are shown as a black dashed straight line.

almost a magnitude and a half between the peak of the distribution and the 50% completeness. There is a sharp cut on the distribution only half a magnitude past the TO point, but said turnover is not a consequence of the magnitude cut: the cut was introduced in section 8.3 as part of our photometric cuts to select GCs and there was *already* a dip in the amount of points, barely evident in figure 22. In fact, this decrement was our motivation to place the magnitude cut at that value. At $i = 26.5$ mag, our data is complete at around 85% with a very slow decline, so that any change in the distribution due to completeness will fall well within the errors. Comparing this with previous values proved hard since many studies are based in Johnson V photometry but, despite being unable to parameterise the GCLF, Madrid et al. [119] say that their peak in $i = 25.5$ mag is a magnitude brighter than the GCLF calculated around bright early-type galaxies in Coma [100, 86], consistent with our calculated value.

10.7 CALCULATING THE AMOUNT OF GCS IN OUR SURVEY

Using the i band GCLF as it is the most complete, we attempt to calculate the amount of GCs in our survey footprint. Besides taking into account the shape of the GCLF, the smaller size of the IR channel of WFC3 with respect to the UVIS channel has to be taken into account, as the completeness for point sources. We will address these effects one by one, considering that our starting number of GCs is 9165.

1. **IR footprint**: we study how many more objects we would find if the WFC3/IR channel FOV were as big as the UVIS channel. The UVIS channel is 57% larger than the IR channel so,

assuming that in large enough scales the GC distribution is homogeneous, we would have 14389 GCs in total in our footprint. The assumption of homogeneity is imprecise given that there is a higher concentration of GCs around the cD galaxies, which fall squarely in the gaps of the IR pattern. In the overall picture this would average with the lower densities far from the center of the cluster. There is also a gap left by the archival data just north-west of NGC 4889, but is small compared with the total difference between the IR and UVIS mosaics.

2. **Completeness of point sources**: we study how the number of GCs changes when taking into account the efficiency of our automatic detection procedure. For the magnitude range of our selected GCs ($22 \lesssim i \lesssim 27$) the completeness level maintains an almost constant value of 85%, so dividing out previous number of 14389 GCs by 0.85 we get 16928 GCs in the footprint of our survey. This completeness value may vary a few percent if we take it as a function of spatial distribution, but as we saw, in the *i* band there is not much variation of the completeness in the tiles of different average surface brightness, as was the case with the *H* band.

3. **GCLF**: we study how many more clusters are present in the cluster but are too dim and they were either left out because of our photometric cuts or were not detected by SExtractor. We use the *i* band GCLF with their $1-\sigma$ errors and a total of 16928 clusters up to $i = 27.1$. Two million random values are drawn from the normal distributions of μ_g and σ_g shown in figure 42 to calculate the total amount of GCs present in the core region of the Coma cluster. The final number of clusters is 19958^{+1080}_{-946} clusters, with a random error propagated from the errors in the fit of the GCLF

For comparison, Madrid et al. [119] report 22426 GC candidates, a number barely off our error, but with a footprint that is 69% larger than ours (25 ACS/WFC tiles versus 23 WFC3/UVIS tiles). They don't account for any errors or uncertainties like completeness of GCLF, just giving a brief mention about them.

10.8 SURFACE DENSITY OF GCS

Direct comparison of total number of GCs with Peng et al. [138] is harder due to a more different footprint and spatial coverage, so instead the surface densities as measured from NGC 4874 are compared. We show our calculated surface density in figure 43. We took annuli of logarithmically increasing distance from NGC 4874 and calculated the density of GCs inside said annuli using the corrected number of GCs obtained in the previous section. Compared to figure 5 of Peng

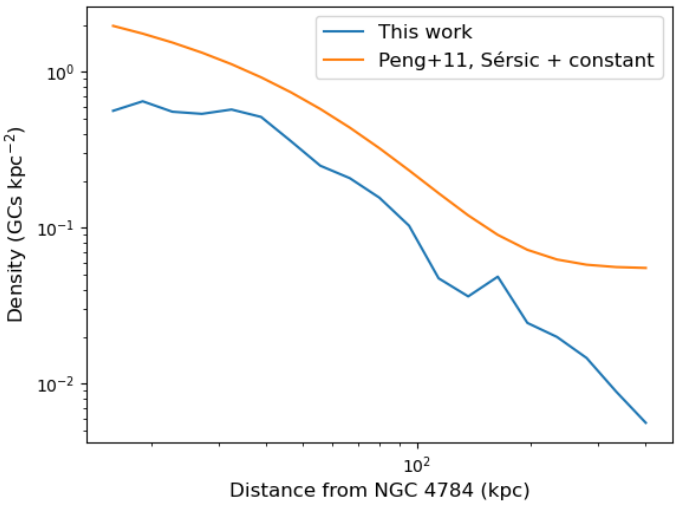

Figure 43: Surface density of GCs as a function of distance to NGC 4874. The number of GCs has been corrected for the effects mentioned in section 10.7

et al., they obtain a higher density in all regions. We propose that this difference arise in the efficiency in which their method is not biased towards selecting red clusters as compared to ours, which includes the u band. As the blue population is much more prominent for IGCs, we are undersampling such population with our selection method. The same overall behaviour is seen if instead of choosing NGC 4874 as the center of the GC system, NGC 4889 is chosen.

Part V

SUMMARY

11 CONCLUSIONS

11.1 THE SURVEY

We present the **C**oma **C**luster **C**ore **Pr****O**yect, or C^3PO for short, in which we have tiled the inner ≈ 150 square arcminutes of the nearby Coma Cluster of galaxies. We used both the UVIS and the IR channels of WFC3 mounted in HST, to perform deep observations of the highest possible spatial resolution with virtually no sky contamination. We extend the previous optical coverage obtained by Co8 and other HST programs with the same spatial resolution and similar depth by Blakeslee and Chiboucas, to the near-UV with u_{336} observations, and to the near-IR with H_{160} data, to improve object classification, characterisation of stellar populations of different aggregations, trace star formation regions, among other science objectives. These objectives will be achieved thanks to the depth obtained with our program, available to get up to the GCLF-TO at 50% completeness limits, and combining our depth with our spatial resolution and spectral coverage, while adding the previous data, we can perform a tomography of objects in the line of sight of the Coma Cluster Core, and study the history of mass assembly of baryonic structures in the cluster.

11.2 THE SELECTION METHOD

We test the *uiH* CC diagram to select GCs and separate them from foreground stars and background unresolved galaxies. The diagram alone proves not fruitful, but we use it as a guide to have a clean, non-magnitude dependant selection of GCs down to the 50% completeness limit of our data and to the GCLF-TO magnitude of the GC system. We show that this diagram may be used to select UCDs and NSCs as well.

11.3 THE RESULTS

We select more than 9000 GCs from our data, from which we estimate age and metallicity using SSP models. Two populations can be identified: a young, metal-rich, and an old, metal-poor. From our estimates, there is no clear colour-age-metallicity relation; instead, the derived quantities come from the inclusion of the two bands outside of the visible spectrum. We recover the results previously found by Peng et al. [138] of a IGC population mostly blue, located around NGC 4874. We do not recover the relative amounts of blue and red IGCs

presented in Madrid et al. [119] due to our GC colours not being as red as theirs. This may be a selection effect due to the inclusion of the u band which is our limiting magnitude. The GCs follow also the CC-environment relation found by Powalka et al. [147] for Virgo GCs, hinting at a different star formation history and chemical enrichment history for different environments. From our selection of GCs we are able to calculate conservative lower limits for the GCLFT-TO in g and H, and confidently calculate the GCLF-TO for the i band. We calculate the total number of GC candidates in our data to be just below 20000 taking into account gaps in our footprint, completeness and GCLF. These numbers are compared with absolute numbers and surface densities from previous works.

BIBLIOGRAPHY

[1] G. O. Abell. The distribution of rich clusters of galaxies. *ApJS*, 3:211, May 1958. doi: 10.1086/190036.

[2] G. O. Abell, H. G. Corwin, Jr., and R. P. Olowin. A catalog of rich clusters of galaxies. *ApJS*, 70:1–138, May 1989. doi: 10.1086/191333.

[3] M. Ackermann, M. Ajello, A. Albert, W. B. Atwood, L. Baldini, J. Ballet, G. Barbiellini, D. Bastieri, K. Bechtol, R. Bellazzini, E. Bissaldi, R. D. Blandford, E. D. Bloom, R. Bonino, E. Bottacini, J. Bregeon, P. Bruel, R. Buehler, G. A. Caliandro, R. A. Cameron, M. Caragiulo, P. A. Caraveo, J. M. Casandjian, E. Cavazzuti, C. Cecchi, E. Charles, A. Chekhtman, G. Chiaro, S. Ciprini, J. Cohen-Tanugi, J. Conrad, S. Cutini, F. D'Ammando, A. de Angelis, F. de Palma, R. Desiante, S. W. Digel, L. Di Venere, P. S. Drell, C. Favuzzi, S. J. Fegan, Y. Fukazawa, S. Funk, P. Fusco, F. Gargano, D. Gasparrini, N. Giglietto, F. Giordano, M. Giroletti, G. Godfrey, D. Green, I. A. Grenier, S. Guiriec, E. Hays, J. W. Hewitt, D. Horan, G. Jóhannesson, M. Kuss, S. Larsson, L. Latronico, J. Li, L. Li, F. Longo, F. Loparco, M. N. Lovellette, P. Lubrano, G. M. Madejski, S. Maldera, A. Manfreda, M. Mayer, M. N. Mazziotta, P. F. Michelson, W. Mitthumsiri, T. Mizuno, M. E. Monzani, A. Morselli, I. V. Moskalenko, S. Murgia, E. Nuss, T. Ohsugi, M. Orienti, E. Orlando, J. F. Ormes, D. Paneque, M. Pesce-Rollins, V. Petrosian, F. Piron, G. Pivato, T. A. Porter, S. Rainò, R. Rando, M. Razzano, A. Reimer, O. Reimer, M. Sánchez-Conde, C. Sgrò, E. J. Siskind, F. Spada, G. Spandre, P. Spinelli, H. Tajima, H. Takahashi, J. B. Thayer, L. Tibaldo, D. F. Torres, G. Tosti, E. Troja, G. Vianello, K. S. Wood, S. Zimmer, Fermi-LAT Collaboration, and Y. Rephaeli. Search for gamma-ray emission from the coma cluster with six years of fermi-lat data. *ApJ*, 819:149, March 2016. doi: 10.3847/0004-637X/819/2/149.

[4] F. Aharonian, A. G. Akhperjanian, G. Anton, U. Barres de Almeida, A. R. Bazer-Bachi, Y. Becherini, B. Behera, K. Bernlöhr, C. Boisson, A. Bochow, V. Borrel, E. Brion, J. Brucker, P. Brun, R. Bühler, T. Bulik, I. Büsching, T. Boutelier, P. M. Chadwick, A. Charbonnier, R. C. G. Chaves, A. Cheesebrough, L. M. Chounet, A. C. Clapson, G. Coignet, M. Dalton, M. K. Daniel, I. D. Davids, B. Degrange, C. Deil, H. J. Dickinson, A. Djannati-Ataï, W. Domainko, L. O'C. Drury, F. Dubois, G. Dubus, J. Dyks, M. Dyrda, K. Egberts, D. Em-

manoulopoulos, P. Espigat, C. Farnier, F. Feinstein, A. Fiasson, A. Förster, G. Fontaine, M. Füßling, S. Gabici, Y. A. Gallant, L. Gérard, B. Giebels, J. F. Glicenstein, B. Glück, P. Goret, D. Göhring, D. Hauser, M. Hauser, S. Heinz, G. Heinzelmann, G. Henri, G. Hermann, J. A. Hinton, A. Hoffmann, W. Hofmann, M. Holleran, S. Hoppe, D. Horns, S. Inoue, A. Jacholkowska, O. C. de Jager, C. Jahn, I. Jung, K. Katarzyński, U. Katz, S. Kaufmann, E. Kendziorra, M. Kerschhaggl, D. Khangulyan, B. Khélifi, D. Keogh, W. Kluźniak, T. Kneiske, Nu. Komin, K. Kosack, G. Lamanna, J. P. Lenain, T. Lohse, V. Marandon, J. M. Martin, O. Martineau-Huynh, A. Marcowith, D. Maurin, T. J. L. McComb, M. C. Medina, R. Moderski, E. Moulin, M. Naumann-Godo, M. de Naurois, D. Nedbal, D. Nekrassov, J. Niemiec, S. J. Nolan, S. Ohm, J. F. Olive, E. de Oña Wilhelmi, K. J. Orford, M. Ostrowski, M. Panter, M. Paz Arribas, G. Pedaletti, G. Pelletier, P. O. Petrucci, S. Pita, G. Pühlhofer, M. Punch, A. Quirrenbach, B. C. Raubenheimer, M. Raue, S. M. Rayner, M. Renaud, O. Reimer, F. Rieger, J. Ripken, L. Rob, S. Rosier- Lees, G. Rowell, B. Rudak, C. B. Rulten, J. Ruppel, V. Sahakian, A. Santangelo, R. Schlickeiser, F. M. Schöck, R. Schröder, U. Schwanke, S. Schwarzburg, S. Schwemmer, A. Shalchi, M. Sikora, J. L. Skilton, H. Sol, D. Spanglfoer, Ł. Stawarz, R. Steenkamp, C. Stegmann, G. Superina, A. Szostek, P. H. Tam, J. P. Tavernet, R. Terrier, O. Tibolla, M. Tluczykont, C. van Eldik, G. Vasileiadis, C. Venter, L. Venter, J. P. Vialle, P. Vincent, M. Vivier, H. J. Völk, F. Volpe, S. J. Wagner, M. Ward, A. A. Zdziarski, and A. Zech. Constraints on the multi-TeV particle population in the Coma galaxy cluster with HESS observations. *A&A*, 502:437–443, August 2009. doi: 10.1051/0004-6361/200912086.

[5] Adebusola Alabi, Anna Ferré-Mateu, Aaron J. Romanowsky, Jean Brodie, Duncan A. Forbes, Asher Wasserman, Sabine Bellstedt, Ignacio Martín-Navarro, Viraj Pandya, Maria B. Stone, and Nobuhiro Okabe. Origins of ultradiffuse galaxies in the Coma cluster - I. Constraints from velocity phase space. *MNRAS*, 479:3308–3318, September 2018. doi: 10.1093/mnras/sty1616.

[6] N. C. Amorisco, A. Monachesi, A. Agnello, and S. D. M. White. The globular cluster systems of 54 Coma ultra-diffuse galaxies: statistical constraints from HST data. *MNRAS*, 475:4235–4251, April 2018. doi: 10.1093/mnras/sty116.

[7] S. Andreon. The morphological segregation of galaxies in clusters. II. The properties of galaxies in the Coma cluster. *A&A*, 314:763–775, October 1996.

[8] Fabio Antonini. Origin and Growth of Nuclear Star Clusters around Massive Black Holes. *ApJ*, 763:62, January 2013. doi: 10.1088/0004-637X/763/1/62.

[9] Fabio Antonini. On the Distribution of Stellar Remnants around Massive Black Holes: Slow Mass Segregation, Star Cluster Inspirals, and Correlated Orbits. *ApJ*, 794:106, October 2014. doi: 10.1088/0004-637X/794/2/106.

[10] Astropy Collaboration, T. P. Robitaille, E. J. Tollerud, P. Greenfield, M. Droettboom, E. Bray, T. Aldcroft, M. Davis, A. Ginsburg, A. M. Price-Whelan, W. E. Kerzendorf, A. Conley, N. Crighton, K. Barbary, D. Muna, H. Ferguson, F. Grollier, M. M. Parikh, P. H. Nair, H. M. Unther, C. Deil, J. Woillez, S. Conseil, R. Kramer, J. E. H. Turner, L. Singer, R. Fox, B. A. Weaver, V. Zabalza, Z. I. Edwards, K. Azalee Bostroem, D. J. Burke, A. R. Casey, S. M. Crawford, N. Dencheva, J. Ely, T. Jenness, K. Labrie, P. L. Lim, F. Pierfederici, A. Pontzen, A. Ptak, B. Refsdal, M. Servillat, and O. Streicher. Astropy: A community Python package for astronomy. *A&A*, 558:A33, October 2013. doi: 10.1051/0004-6361/201322068.

[11] R. J. Avila, W. Hack, M. Cara, D. Borncamp, J. Mack, L. Smith, and L. Ubeda. Drizzlepac 2.0 - introducing new features. In A. R. Taylor and E. Rosolowsky, editors, *Astronomical Data Analysis Software an Systems XXIV (ADASS XXIV)*, volume 495 of *Astronomical Society of the Pacific Conference Series*, page 281, September 2015.

[12] Neta A. Bahcall. Structure of the Central Region of the Coma Cluster. *ApJ*, 183:783–790, August 1973. doi: 10.1086/152267.

[13] Frank W. Baier, Klaus Fritze, and Heinz Tiersch. The asymmetry of the Coma cluster of galaxies. *Astronomische Nachrichten*, 311:89, February 1990. doi: 10.1002/asna.2113110202.

[14] Pauline Barmby, John P. Huchra, and Jean P. Brodie. The m31 globular cluster luminosity function. *AJ*, 121(3):1482–1496, March 2001. doi: 10.1086/319389. URL https://ui.adsabs.harvard.edu/abs/2001AJ....121.1482B.

[15] M. A. Beasley, A. J. Romanowsky, V. Pota, I. M. Navarro, D. Martinez Delgado, F. Neyer, and A. L. Deich. An overmassive dark halo around an ultra-diffuse galaxy in the virgo cluster. *ApJL*, 819:L20, March 2016. doi: 10.3847/2041-8205/819/2/L20.

[16] Kenji Bekki and Hideki Yahagi. On spatial distributions of old globular clusters in clusters of galaxies. *MNRAS*, 372:1019–1033, November 2006. doi: 10.1111/j.1365-2966.2006.10833.x.

[17] E. Bertin. Automated Morphometry with SExtractor and PSFEx. In I. N. Evans, A. Accomazzi, D. J. Mink, and A. H. Rots, editors, *Astronomical Data Analysis Software and Systems XX*, volume 442 of *Astronomical Society of the Pacific Conference Series*, page 435, July 2011.

[18] E. Bertin and S. Arnouts. SExtractor: Software for source extraction. *A&AS*, 117:393–404, June 1996. doi: 10.1051/aas:1996164.

[19] Bruno Binggeli, G. A. Tammann, and Allan Sandage. Studies of the Virgo Cluster. VI. Morphological and Kinematical Structure of the Virgo Cluster. *AJ*, 94:251, August 1987. doi: 10.1086/114467.

[20] J. Blakeslee. A definitive distance to the coma core ellipticals. HST Proposal, July 2009.

[21] J. P. Blakeslee, A. Jordán, S. Mei, P. Côté, L. Ferrarese, L. Infante, E. W. Peng, J. L. Tonry, and M. J. West. The ACS Fornax Cluster Survey. V. Measurement and Recalibration of Surface Brightness Fluctuations and a Precise Value of the Fornax-Virgo Relative Distance. *ApJ*, 694:556–572, March 2009. doi: 10.1088/0004-637X/694/1/556.

[22] John P. Blakeslee. Globular Clusters in Dense Clusters of Galaxies. *AJ*, 118:1506–1525, October 1999. doi: 10.1086/301052.

[23] T. Böker. Nuclear star clusters. In R. de Grijs and J. R. D. Lépine, editors, *Star Clusters: Basic Galactic Building Blocks Throughout Time and Space*, volume 266 of *IAU Symposium*, pages 58–63, January 2010. doi: 10.1017/S1743921309990871.

[24] Torsten Böker, Seppo Laine, Roeland P. van der Marel, Marc Sarzi, Hans-Walter Rix, Luis C. Ho, and Joseph C. Shields. A Hubble Space Telescope Census of Nuclear Star Clusters in Late-Type Spiral Galaxies. I. Observations and Image Analysis. *AJ*, 123:1389–1410, March 2002. doi: 10.1086/339025.

[25] A. Bonafede, L. Feretti, M. Murgia, F. Govoni, G. Giovannini, D. Dallacasa, K. Dolag, and G. B. Taylor. The Coma cluster magnetic field from Faraday rotation measures. *A&A*, 513:A30, April 2010. doi: 10.1051/0004-6361/200913696.

[26] G. Bono, P. B. Stetson, D. A. VandenBerg, A. Calamida, M. Dall'Ora, G. Iannicola, P. Amico, A. Di Cecco, E. Marchetti, M. Monelli, N. Sanna, A. R. Walker, M. Zoccali, R. Buonanno, F. Caputo, C. E. Corsi, S. Degl'Innocenti, S. D'Odorico, I. Ferraro, R. Gilmozzi, J. Melnick, M. Nonino, S. Ortolani, A. M. Piersimoni, P. G. Prada Moroni, L. Pulone, M. Romaniello, and

J. Storm. On a new near-infrared method to estimate the absolute ages of star clusters: Ngc 3201 as a first test case. *ApJL*, 708: L74–L79, January 2010. doi: 10.1088/2041-8205/708/2/L74.

[27] S. Brown and L. Rudnick. Diffuse radio emission in/around the coma cluster: beyond simple accretion. *MNRAS*, 412:2–12, March 2011. doi: 10.1111/j.1365-2966.2010.17738.x.

[28] R. C. Brüns, P. Kroupa, M. Fellhauer, M. Metz, and P. Assmann. A parametric study on the formation of extended star clusters and ultra- compact dwarf galaxies. *A&A*, 529:A138, May 2011. doi: 10.1051/0004-6361/201016220.

[29] Jack O. Burns, Kurt Roettiger, Michael Ledlow, and Anatoly Klypin. The Coma Cluster after Lunch: Has a Galaxy Group Passed through the Cluster Core? *ApJ*, 427:L87, June 1994. doi: 10.1086/187371.

[30] N. Caldwell, J. A. Rose, R. M. Sharples, R. S. Ellis, and R. G. Bower. Star formation in early-type galaxies in the Coma cluster. *AJ*, 106:473–492, August 1993. doi: 10.1086/116656.

[31] Michele Cantiello, Aniello Grado, Marina Rejkuba, Magda Arnaboldi, Massimo Capaccioli, Laura Greggio, Enrica Iodice, and Luca Limatola. A VST and VISTA study of globular clusters in NGC 253. *Astronomy & Astrophysics*, 611:A21, mar 2018. doi: 10.1051/0004-6361/201731325.

[32] R. Capuzzo-Dolcetta and I. Tosta e Melo. On the relation between the mass of Compact Massive Objects and their host galaxies. *MNRAS*, 472:4013–4023, December 2017. doi: 10.1093/mnras/stx2246.

[33] Nicolas Cardiel. Rmodel: Determining stellar population parameters, April 2011. URL https://ui.adsabs.harvard.edu/abs/2011ascl.soft04008C.

[34] C. Marcella Carollo, Massimo Stiavelli, Marc Seigar, P. Tim de Zeeuw, and Herwig Dejonghe. Spiral Galaxies with HST/NICMOS. I. Nuclear Morphologies, Color Maps, and Distinct Nuclei. *AJ*, 123:159–183, January 2002. doi: 10.1086/324725.

[35] D. Carter, P. Goudfrooij, B. Mobasher, H. C. Ferguson, T. H. Puzia, A. L. Aguerri, M. Balcells, D. Batcheldor, T. J. Bridges, J. I. Davies, P. Erwin, A. W. Graham, R. Guzmán, D. Hammer, A. Hornschemeier, C. Hoyos, M. J. Hudson, A. Huxor, S. Jogee, Y. Komiyama, J. Lotz, J. R. Lucey, R. O. Marzke, D. Merritt, B. W. Miller, N. A. Miller, M. Mouhcine, S. Okamura, R. F. Peletier, S. Phillipps, B. M. Poggianti, R. M. Sharples, R. J. Smith, N. Trentham, R. B. Tully, E. Valentijn, and G. Verdoes Kleijn. The hubble space telescope advanced camera for surveys coma cluster

survey. i. survey objectives and design. *ApJS*, 176:424-437, June 2008. doi: 10.1086/533439.

[36] T. K. Chan, D. Kereš, A. Wetzel, P. F. Hopkins, C.-A. Faucher-Giguère, K. El-Badry, S. Garrison-Kimmel, and M. Boylan-Kolchin. The origin of ultra diffuse galaxies: stellar feedback and quenching. *MNRAS*, 478:906–925, July 2018. doi: 10.1093/mnras/sty1153.

[37] K. Chiboucas. Origin of ucds in the coma cluster. HST Proposal, October 2012.

[38] K. Chiboucas, R. B. Tully, R. O. Marzke, S. Phillipps, J. Price, E. W. Peng, N. Trentham, D. Carter, and D. Hammer. Ultra-compact Dwarfs in the Coma Cluster. *ApJ*, 737:86, August 2011. doi: 10.1088/0004-637X/737/2/86.

[39] K. Chiboucas, P. Ferguson, R. B. Tully, D. Carter, S. Phillipps, and E. Peng. The ucd population of the coma cluster. In C. Charbonnel and A. Nota, editors, *Formation, Evolution, and Survival of Massive Star Clusters*, volume 316 of *IAU Symposium*, pages 253–254, March 2017. doi: 10.1017/S1743921315008893.

[40] Kristin Chiboucas, R. Brent Tully, Ronald O. Marzke, Neil Trentham, Henry C. Ferguson, Derek Hammer, David Carter, and Habib Khosroshahi. Keck/LRIS Spectroscopic Confirmation of Coma Cluster Dwarf Galaxy Membership Assignments. *ApJ*, 723:251–266, November 2010. doi: 10.1088/0004-637X/723/1/251.

[41] I. V. Chilingarian and I. Y. Zolotukhin. A universal ultraviolet-optical colour-colour-magnitude relation of galaxies. *MNRAS*, 419:1727–1739, January 2012. doi: 10.1111/j.1365-2966.2011.19837.x.

[42] I. V. Chilingarian, A.-L. Melchior, and I. Y. Zolotukhin. Analytical approximations of k-corrections in optical and near-infrared bands. *MNRAS*, 405:1409–1420, July 2010. doi: 10.1111/j.1365-2966.2010.16506.x.

[43] I. Chiu, S. Desai, and J. Liu. ComEst: A completeness estimator of source extraction on astronomical imaging. *Astronomy and Computing*, 16:79–87, July 2016. doi: 10.1016/j.ascom.2016.04.005.

[44] H. Cho, J. P. Blakeslee, A. L. Chies-Santos, M. J. Jee, J. B. Jensen, E. W. Peng, and Y.-W. Lee. The Globular Cluster System of the Coma cD Galaxy NGC 4874 from Hubble Space Telescope ACS and WFC3/IR Imaging. *ApJ*, 822:95, May 2016. doi: 10.3847/0004-637X/822/2/95.

[45] E. Churazov, I. Khabibullin, N. Lyskova, R. Sunyaev, and A. M. Bykov. Tempestuous life beyond r_500: X-ray view on the coma cluster with srg/erosita. i. x-ray morphology, recent merger, and radio halo connection. *arXiv e-prints*, art. arXiv:2012.11627, December 2020. URL https://ui.adsabs.harvard.edu/abs/2020arXiv201211627C.

[46] Matthew Colless and Andrew M. Dunn. Structure and Dynamics of the Coma Cluster. *ApJ*, 458:435, February 1996. doi: 10.1086/176827.

[47] E. M. Corsini, G. Wegner, R. P. Saglia, J. Thomas, R. Bender, and D. Thomas. Spatially Resolved Spectroscopy of Coma Cluster Early-Type Galaxies. IV. Completing the Data Set. *The Astrophysical Journal Supplement Series*, 175:462–484, April 2008. doi: 10.1086/524409.

[48] P. Côté, J. P. Blakeslee, L. Ferrarese, A. Jordán, S. Mei, D. Merritt, M. Milosavljević, E. W. Peng, J. L. Tonry, and M. J. West. The acs virgo cluster survey. i. introduction to the survey. *ApJS*, 153: 223–242, July 2004. doi: 10.1086/421490.

[49] Patrick Côté, Slawomir Piatek, Laura Ferrarese, Andrés Jordán, David Merritt, Eric W. Peng, Monica Haşegan, John P. Blakeslee, Simona Mei, Michael J. West, Miloš Milosavljević, and John L. Tonry. The ACS Virgo Cluster Survey. VIII. The Nuclei of Early-Type Galaxies. *The Astrophysical Journal Supplement Series*, 165: 57–94, July 2006. doi: 10.1086/504042.

[50] E. Daddi, A. Cimatti, A. Renzini, A. Fontana, M. Mignoli, L. Pozzetti, P. Tozzi, and G. Zamorani. A new photometric technique for the joint selection of star-forming and passive galaxies at $1.4 \lesssim z \lesssim 2.5$. *ApJ*, 617:746–764, December 2004. doi: 10.1086/425569.

[51] R. I. Davies, F. Müller Sánchez, R. Genzel, L. J. Tacconi, E. K. S. Hicks, S. Friedrich, and A. Sternberg. A Close Look at Star Formation around Active Galactic Nuclei. *ApJ*, 671:1388–1412, December 2007. doi: 10.1086/523032.

[52] Elisabetta De Filippis, Mauro Sereno, Mark W. Bautz, and Giuseppe Longo. Measuring the Three-dimensional Structure of Galaxy Clusters. I. Application to a Sample of 25 Clusters. *ApJ*, 625:108–120, May 2005. doi: 10.1086/429401.

[53] M. den Brok, R. F. Peletier, E. A. Valentijn, M. Balcells, D. Carter, P. Erwin, H. C. Ferguson, P. Goudfrooij, A. W. Graham, D. Hammer, J. R. Lucey, N. Trentham, R. Guzmán, C. Hoyos, G. Verdoes Kleijn, S. Jogee, A. M. Karick, I. Marinova, M. Mouhcine, and T. Weinzirl. The HST/ACS Coma Cluster Survey - VI. Colour

gradients in giant and dwarf early-type galaxies. *MNRAS*, 414: 3052–3070, July 2011. doi: 10.1111/j.1365-2966.2011.18606.x.

[54] M. den Brok, R. F. Peletier, A. Seth, M. Balcells, L. Dominguez, A. W. Graham, D. Carter, P. Erwin, H. C. Ferguson, P. Goudfrooij, R. Guzmán, C. Hoyos, S. Jogee, J. Lucey, S. Phillipps, T. Puzia, E. Valentijn, G. Verdoes Kleijn, and T. Weinzirl. The HST/ACS Coma Cluster Survey - X. Nuclear star clusters in low-mass early-type galaxies: scaling relations. *MNRAS*, 445: 2385–2403, December 2014. doi: 10.1093/mnras/stu1906.

[55] A. Di Cintio, C. B. Brook, A. A. Dutton, A. V. Macciò, A. Obreja, and A. Dekel. Nihao - xi. formation of ultra-diffuse galaxies by outflows. *MNRAS*, 466:L1–L6, March 2017. doi: 10.1093/mnrasl/slw210.

[56] L. Dressel. *Wide Field Camera 3 Instrument Handbook, Version 10.0*. Baltimore: STScI, 2018.

[57] M. J. Drinkwater, J. B. Jones, M. D. Gregg, and S. Phillipps. Compact Stellar Systems in the Fornax Cluster: Super-massive Star Clusters or Extremely Compact Dwarf Galaxies? *Publications of the Astronomical Society of Australia*, 17:227–233, December 2000. doi: 10.1071/AS00034.

[58] M. J. Drinkwater, M. D. Gregg, B. A. Holman, and M. J. I. Brown. The evolution and star formation of dwarf galaxies in the Fornax Cluster. *MNRAS*, 326:1076–1094, September 2001. doi: 10.1046/j.1365-8711.2001.04646.x.

[59] M. J. Drinkwater, M. D. Gregg, W. J. Couch, H. C. Ferguson, M. Hilker, J. B. Jones, A. Karick, and S. Phillipps. Ultra-Compact Dwarf Galaxies in Galaxy Clusters. *PASA*, 21:375–378, 2004. doi: 10.1071/AS04048.

[60] Michael J. Drinkwater, Michael D. Gregg, and Matthew Colless. Substructure and Dynamics of the Fornax Cluster. *ApJ*, 548: L139–L142, February 2001. doi: 10.1086/319113.

[61] Louise O. V. Edwards and Dario Fadda. A Multi-wavelength Analysis of Spitzer Selected Coma Cluster Galaxies: Star Formation Rates and Masses. *AJ*, 142:148, November 2011. doi: 10.1088/0004-6256/142/5/148.

[62] V. Epanechnikov. Non-parametric estimation of a multivariate probability density. *Theory of Probability & Its Applications*, 14(1): 153–158, 1969. doi: 10.1137/1114019. URL https://doi.org/10.1137/1114019.

[63] L. Ferrarese, P. Côté, J.-C. Cuillandre, S. D. J. Gwyn, E. W. Peng, L. A. MacArthur, P.-A. Duc, A. Boselli, S. Mei, T. Erben, A. W. McConnachie, P. R. Durrell, J. C. Mihos, A. Jordán, A. Lançon, T. H. Puzia, E. Emsellem, M. L. Balogh, J. P. Blakeslee, L. van Waerbeke, R. Gavazzi, B. Vollmer, J. J. Kavelaars, D. Woods, N. M. Ball, S. Boissier, S. Courteau, E. Ferriere, G. Gavazzi, H. Hildebrandt, P. Hudelot, M. Huertas-Company, C. Liu, D. McLaughlin, Y. Mellier, M. Milkeraitis, D. Schade, C. Balkowski, F. Bournaud, R. G. Carlberg, S. C. Chapman, H. Hoekstra, C. Peng, M. Sawicki, L. Simard, J. E. Taylor, R. B. Tully, W. van Driel, C. D. Wilson, T. Burdullis, B. Mahoney, and N. Manset. The Next Generation Virgo Cluster Survey (NGVS). I. Introduction to the Survey. *ApJS*, 200:4, May 2012. doi: 10.1088/0067-0049/200/1/4.

[64] Laura Ferrarese, Patrick Côté, Elena Dalla Bontà, Eric W. Peng, David Merritt, Andrés Jordán, John P. Blakeslee, Monica Haşegan, Simona Mei, Slawomir Piatek, John L. Tonry, and Michael J. West. A Fundamental Relation between Compact Stellar Nuclei, Supermassive Black Holes, and Their Host Galaxies. *ApJ*, 644:L21–L24, June 2006. doi: 10.1086/505388.

[65] Anna Ferré-Mateu, Adebusola Alabi, Duncan A. Forbes, Aaron J. Romanowsky, Jean Brodie, Viraj Pandya, Ignacio Martín-Navarro, Sabine Bellstedt, Asher Wasserman, Maria B. Stone, and Nobuhiro Okabe. Origins of ultradiffuse galaxies in the Coma cluster - II. Constraints from their stellar populations. *MNRAS*, 479:4891–4906, October 2018. doi: 10.1093/mnras/sty1597.

[66] Philippe Fischer, James E. Hesser, Hugh C. Harris, and Gregory D. Bothun. The globular cluster system of the edge-on sb galaxy ngc 5170. *PASP*, 102:5, January 1990. doi: 10.1086/132602. URL https://ui.adsabs.harvard.edu/abs/1990PASP..102....5F.

[67] Michael Fitchett and Rachel Webster. Substructure in the Coma Cluster. *ApJ*, 317:653, June 1987. doi: 10.1086/165310.

[68] E. L. Fitzpatrick. Correcting for the Effects of Interstellar Extinction. *PASP*, 111:63–75, January 1999. doi: 10.1086/316293.

[69] D. A. Forbes, J. I. Read, M. Gieles, and M. L. M. Collins. Extending the globular cluster system-halo mass relation to the lowest galaxy masses. *MNRAS*, 481:5592–5605, December 2018. doi: 10.1093/mnras/sty2584.

[70] Duncan A. Forbes, Paul Lasky, Alister W. Graham, and Lee Spitler. Uniting old stellar systems: from globular clusters to

giant ellipticals. *MNRAS*, 389:1924–1936, October 2008. doi: 10.1111/j.1365-2966.2008.13739.x.

[71] Gaia Collaboration, T. Prusti, J. H. J. de Bruijne, A. G. A. Brown, A. Vallenari, C. Babusiaux, C. A. L. Bailer-Jones, U. Bastian, M. Biermann, D. W. Evans, and et al. The Gaia mission. *A&A*, 595:A1, November 2016. doi: 10.1051/0004-6361/201629272.

[72] Gaia Collaboration, A. G. A. Brown, A. Vallenari, T. Prusti, J. H. J. de Bruijne, C. Babusiaux, C. A. L. Bailer-Jones, M. Biermann, D. W. Evans, L. Eyer, and et al. Gaia Data Release 2. Summary of the contents and survey properties. *A&A*, 616:A1, August 2018. doi: 10.1051/0004-6361/201833051.

[73] Gaia Collaboration, F. Mignard, S. A. Klioner, L. Lindegren, J. Hernández, U. Bastian, A. Bombrun, D. Hobbs, U. Lammers, D. Michalik, M. Ramos-Lerate, M. Biermann, J. Fernández-Hernández, R. Geyer, T. Hilger, H. I. Siddiqui, H. Steidelmüller, C. Babusiaux, C. Barache, S. Lambert, A. H. Andrei, G. Bourda, P. Charlot, A. G. A. Brown, A. Vallenari, T. Prusti, J. H. J. de Bruijne, C. A. L. Bailer-Jones, D. W. Evans, L. Eyer, F. Jansen, C. Jordi, X. Luri, C. Panem, D. Pourbaix, S. Randich, P. Sartoretti, C. Soubiran, F. van Leeuwen, N. A. Walton, F. Arenou, M. Cropper, R. Drimmel, D. Katz, M. G. Lattanzi, J. Bakker, C. Cacciari, J. Castañeda, L. Chaoul, N. Cheek, F. De Angeli, C. Fabricius, R. Guerra, B. Holl, E. Masana, R. Messineo, N. Mowlavi, K. Nienartowicz, P. Panuzzo, J. Portell, M. Riello, G. M. Seabroke, P. Tanga, F. Thévenin, G. Gracia-Abril, G. Comoretto, M. Garcia-Reinaldos, D. Teyssier, M. Altmann, R. Andrae, M. Audard, I. Bellas-Velidis, K. Benson, J. Berthier, R. Blomme, P. Burgess, G. Busso, B. Carry, A. Cellino, G. Clementini, M. Clotet, O. Creevey, M. Davidson, J. De Ridder, L. Delchambre, A. Dell'Oro, C. Ducourant, M. Fouesneau, Y. Frémat, L. Galluccio, M. García-Torres, J. González-Núñez, J. J. González- Vidal, E. Gosset, L. P. Guy, J. L. Halbwachs, N. C. Hambly, D. L. Harrison, D. Hestroffer, S. T. Hodgkin, A. Hutton, G. Jasniewicz, A. Jean-Antoine-Piccolo, S. Jordan, A. J. Korn, A. Krone-Martins, A. C. Lanzafame, T. Lebzelter, W. Löffler, M. Manteiga, P. M. Marrese, J. M. Martín-Fleitas, A. Moitinho, A. Mora, K. Muinonen, J. Osinde, E. Pancino, T. Pauwels, J. M. Petit, A. Recio-Blanco, P. J. Richards, L. Rimoldini, A. C. Robin, L. M. Sarro, C. Siopis, M. Smith, A. Sozzetti, M. Süveges, J. Torra, W. van Reeven, U. Abbas, A. Abreu Aramburu, S. Accart, C. Aerts, G. Altavilla, M. A. Álvarez, R. Alvarez, J. Alves, R. I. Anderson, E. Anglada Varela, E. Antiche, T. Antoja, B. Arcay, T. L. Astraatmadja, N. Bach, S. G. Baker, L. Balaguer-Núñez, P. Balm, C. Barata, D. Barbato, F. Barblan, P. S. Barklem, D. Barrado, M. Barros, M. A.

Barstow, L. Bartholomé Muñoz, J. L. Bassilana, U. Becciani, M. Bellazzini, A. Berihuete, S. Bertone, L. Bianchi, O. Bienaymé, S. Blanco-Cuaresma, T. Boch, C. Boeche, R. Borrachero, D. Bossini, S. Bouquillon, A. Bragaglia, L. Bramante, M. A. Breddels, A. Bressan, N. Brouillet, T. Brüsemeister, E. Brugaletta, B. Bucciarelli, A. Burlacu, D. Busonero, A. G. Butkevich, R. Buzzi, E. Caffau, R. Cancelliere, G. Cannizzaro, T. Cantat-Gaudin, R. Carballo, T. Carlucci, J. M. Carrasco, L. Casamiquela, M. Castellani, A. Castro-Ginard, L. Chemin, A. Chiavassa, G. Cocozza, G. Costigan, S. Cowell, F. Crifo, M. Crosta, C. Crowley, J. Cuypers, C. Dafonte, Y. Damerdji, A. Dapergolas, P. David, M. David, P. de Laverny, F. De Luise, R. De March, R. de Souza, A. de Torres, J. Debosscher, E. del Pozo, M. Delbo, A. Delgado, H. E. Delgado, S. Diakite, C. Diener, E. Distefano, C. Dolding, P. Drazinos, J. Durán, B. Edvardsson, H. Enke, K. Eriksson, P. Esquej, G. Eynard Bontemps, C. Fabre, M. Fabrizio, S. Faigler, A. J. Falcão, M. Farràs Casas, L. Federici, G. Fedorets, P. Fernique, F. Figueras, F. Filippi, K. Findeisen, A. Fonti, E. Fraile, M. Fraser, B. Frézouls, M. Gai, S. Galleti, D. Garabato, F. García-Sedano, A. Garofalo, N. Garralda, A. Gavel, P. Gavras, J. Gerssen, P. Giacobbe, G. Gilmore, S. Girona, G. Giuffrida, F. Glass, M. Gomes, M. Granvik, A. Gueguen, A. Guerrier, J. Guiraud, R. Gutié, R. Haigron, D. Hatzidimitriou, M. Hauser, M. Haywood, U. Heiter, A. Helmi, J. Heu, W. Hofmann, G. Holland, H. E. Huckle, A. Hypki, V. Icardi, K. Janßen, G. Jevardat de Fombelle, P. G. Jonker, A. L. Juhász, F. Julbe, A. Karampelas, A. Kewley, J. Klar, A. Kochoska, R. Kohley, K. Kolenberg, M. Kontizas, E. Kontizas, S. E. Koposov, G. Kordopatis, Z. Kostrzewa-Rutkowska, P. Koubsky, A. F. Lanza, Y. Lasne, J. B. Lavigne, Y. Le Fustec, C. Le Poncin-Lafitte, Y. Lebreton, S. Leccia, N. Leclerc, I. Lecoeur-Taibi, H. Lenhardt, F. Leroux, S. Liao, E. Licata, H. E. P. Lindstrøm, T. A. Lister, E. Livanou, A. Lobel, M. López, S. Managau, R. G. Mann, G. Mantelet, O. Marchal, J. M. Marchant, M. Marconi, S. Marinoni, G. Marschalkó, D. J. Marshall, M. Martino, G. Marton, N. Mary, D. Massari, G. Matijevič, T. Mazeh, P. J. McMillan, S. Messina, N. R. Millar, D. Molina, R. Molinaro, L. Molnár, P. Montegriffo, R. Mor, R. Morbidelli, T. Morel, D. Morris, A. F. Mulone, T. Muraveva, I. Musella, G. Nelemans, L. Nicastro, L. Noval, W. O'Mullane, C. Ordénovic, D. Ordóñez-Blanco, P. Osborne, C. Pagani, I. Pagano, F. Pailler, H. Palacin, L. Palaversa, A. Panahi, M. Pawlak, A. M. Piersimoni, F. X. Pineau, E. Plachy, G. Plum, E. Poggio, E. Poujoulet, A. Prša, L. Pulone, E. Racero, S. Ragaini, N. Rambaux, S. Regibo, C. Reylé, F. Riclet, V. Ripepi, A. Riva, A. Rivard, G. Rixon, T. Roegiers, M. Roelens, M. Romero-Gómez, N. Row-

ell, F. Royer, L. Ruiz-Dern, G. Sadowski, T. Sagristà Sellés, J. Sahlmann, J. Salgado, E. Salguero, N. Sanna, T. Santana-Ros, M. Sarasso, H. Savietto, M. Schultheis, E. Sciacca, M. Segol, J. C. Segovia, D. Ségransan, I. C. Shih, L. Siltala, A. F. Silva, R. L. Smart, K. W. Smith, E. Solano, F. Solitro, R. Sordo, S. Soria Nieto, J. Souchay, A. Spagna, F. Spoto, U. Stampa, I. A. Steele, C. A. Stephenson, H. Stoev, F. F. Suess, J. Surdej, L. Szabados, E. Szegedi-Elek, D. Tapiador, F. Taris, G. Tauran, M. B. Taylor, R. Teixeira, D. Terrett, P. Teyssandier, W. Thuillot, A. Titarenko, F. Torra Clotet, C. Turon, A. Ulla, E. Utrilla, S. Uzzi, M. Vaillant, G. Valentini, V. Valette, A. van Elteren, E. Van Hemelryck, M. van Leeuwen, M. Vaschetto, A. Vecchiato, J. Veljanoski, Y. Viala, D. Vicente, S. Vogt, C. von Essen, H. Voss, V. Votruba, S. Voutsinas, G. Walmsley, M. Weiler, O. Wertz, T. Wevers, Ł. Wyrzykowski, A. Yoldas, M. Žerjal, H. Ziaeepour, J. Zorec, S. Zschocke, S. Zucker, C. Zurbach, and T. Zwitter. Gaia Data Release 2. The celestial reference frame (Gaia-CRF2). *A&A*, 616: A14, August 2018. doi: 10.1051/0004-6361/201832916.

[74] F. Gastaldello, D. R. Wik, S. Molendi, N. J. Westergaard, A. Hornstrup, G. Madejski, D. D. M. Ferreira, S. E. Boggs, F. E. Christensen, W. W. Craig, B. W. Grefenstette, C. J. Hailey, F. A. Harrison, K. K. Madsen, D. Stern, and W. W. Zhang. A nustar observation of the center of the coma cluster. *ApJ*, 800:139, February 2015. doi: 10.1088/0004-637X/800/2/139.

[75] G. Gavazzi, K. O'Neil, A. Boselli, and W. van Driel. H I observations of galaxies. II. The Coma Supercluster. *A&A*, 449:929–935, April 2006. doi: 10.1051/0004-6361:20053844.

[76] G. Gavazzi, G. Savorgnan, and Mattia Fumagalli. The complete census of optically selected AGNs in the Coma supercluster: the dependence of AGN activity on the local environment. *A&A*, 534:A31, October 2011. doi: 10.1051/0004-6361/201117461.

[77] M. J. Geller and J. P. Huchra. Mapping the universe. *Science*, 246: 897–903, November 1989. doi: 10.1126/science.246.4932.897.

[78] Iskren Y. Georgiev, Thomas H. Puzia, Paul Goudfrooij, and Michael Hilker. Globular cluster systems in nearby dwarf galaxies - III. Formation efficiencies of old globular clusters. *MNRAS*, 406:1967–1984, August 2010. doi: 10.1111/j.1365-2966.2010.16802.x.

[79] Rosa A. González-López lira, Luis Lomelí-Núñez, Karla Álamo-Martínez, Yasna Órdenes-Briceño, Laurent Loinard, Iskren Y. Georgiev, Roberto P. Muñoz, Thomas H. Puzia, Gustavo Bruzual A., and Stephen Gwyn. The relation between globular cluster systems and supermassive black holes in spiral

galaxies: The case study of NGC 4258. *The Astrophysical Journal*, 835(2):184, jan 2017. doi: 10.3847/1538-4357/835/2/184.

[80] Morgan Goodman and Kenji Bekki. Formation of ultra-compact dwarf galaxies from supergiant molecular clouds. *MNRAS*, 478: 3564–3575, August 2018. doi: 10.1093/mnras/sty1187.

[81] M. Gu, C. Conroy, D. Law, P. van Dokkum, R. Yan, D. Wake, K. Bundy, A. Merritt, R. Abraham, J. Zhang, M. Bershady, D. Bizyaev, J. Brinkmann, N. Drory, K. Grabowski, K. Masters, K. Pan, J. Parejko, A.-M. Weijmans, and K. Zhang. Low metallicities and old ages for three ultra-diffuse galaxies in the coma cluster. *ApJ*, 859:37, May 2018. doi: 10.3847/1538-4357/aabbae.

[82] Meng Gu, Charlie Conroy, David Law, Pieter van Dokkum, Renbin Yan, David Wake, Kevin Bundy, Alexa Villaume, Roberto Abraham, Allison Merritt, Jielai Zhang, Matthew Bershady, Dmitry Bizyaev, Niv Drory, Kaike Pan, Daniel Thomas, and Anne-Marie Weijmans. Spectroscopic constraints on the buildup of intracluster light in the coma cluster. *ApJ*, 894(1): 32, May 2020. doi: 10.3847/1538-4357/ab845c. URL https://ui.adsabs.harvard.edu/abs/2020ApJ...894...32G.

[83] Monica Haşegan, Andrés Jordán, Patrick Côté, S. G. Djorgovski, Dean E. McLaughlin, John P. Blakeslee, Simona Mei, Michael J. West, Eric W. Peng, Laura Ferrarese, Miloš Milosavljević, John L. Tonry, and David Merritt. The ACS Virgo Cluster Survey. VII. Resolving the Connection between Globular Clusters and Ultracompact Dwarf Galaxies. *ApJ*, 627:203–223, July 2005. doi: 10.1086/430342.

[84] D. Hammer, A. E. Hornschemeier, B. Mobasher, N. Miller, R. Smith, S. Arnouts, B. Milliard, and L. Jenkins. Deep GALEX Observations of the Coma Cluster: Source Catalog and Galaxy Counts. *ApJS*, 190:43–57, September 2010. doi: 10.1088/0067-0049/190/1/43.

[85] D. Hammer, G. Verdoes Kleijn, C. Hoyos, M. den Brok, M. Balcells, H. C. Ferguson, P. Goudfrooij, D. Carter, R. Guzmán, R. F. Peletier, R. J. Smith, A. W. Graham, N. Trentham, E. Peng, T. H. Puzia, J. R. Lucey, S. Jogee, A. L. Aguerri, D. Batcheldor, T. J. Bridges, K. Chiboucas, J. I. Davies, C. del Burgo, P. Erwin, A. Hornschemeier, M. J. Hudson, A. Huxor, L. Jenkins, A. Karick, H. Khosroshahi, E. Kourkchi, Y. Komiyama, J. Lotz, R. O. Marzke, I. Marinova, A. Matkovic, D. Merritt, B. W. Miller, N. A. Miller, B. Mobasher, M. Mouhcine, S. Okamura, S. Percival, S. Phillipps, B. M. Poggianti, J. Price, R. M. Sharples, R. B. Tully, and E. Valentijn. The HST/ACS Coma Cluster Survey.

II. Data Description and Source Catalogs. *ApJS*, 191:143–159, November 2010. doi: 10.1088/0067-0049/191/1/143.

[86] William E. Harris, J. J. Kavelaars, David A. Hanes, Christopher J. Pritchet, and W. A. Baum. The globular cluster systems in the coma ellipticals. iv: Wfpc2 photometry for five giant ellipticals. *AJ*, 137(2):3314–3328, February 2009. doi: 10.1088/0004-6256/137/2/3314. URL https://ui.adsabs.harvard.edu/abs/2009AJ....137.3314H.

[87] N. P. Hathi, R. E. Ryan, Jr., S. H. Cohen, H. Yan, R. A. Windhorst, P. J. McCarthy, R. W. O'Connell, A. M. Koekemoer, M. J. Rutkowski, B. Balick, H. E. Bond, D. Calzetti, M. J. Disney, M. A. Dopita, J. A. Frogel, D. N. B. Hall, J. A. Holtzman, R. A. Kimble, F. Paresce, A. Saha, J. I. Silk, J. T. Trauger, A. R. Walker, B. C. Whitmore, and E. T. Young. Uv-dropout galaxies in the goods-south field from wfc3 early release science observations. *ApJ*, 720:1708–1716, September 2010. doi: 10.1088/0004-637X/720/2/1708.

[88] J. T. C. G. Head, J. R. Lucey, M. J. Hudson, and R. J. Smith. Dissecting the red sequence: the bulge and disc colours of early-type galaxies in the coma cluster. *MNRAS*, 440:1690–1711, May 2014. doi: 10.1093/mnras/stu325.

[89] M. Hilker, L. Infante, G. Vieira, M. Kissler-Patig, and T. Richtler. The central region of the Fornax cluster. II. Spectroscopy and radial velocities of member and background galaxies. *Astronomy and Astrophysics Supplement Series*, 134:75–86, January 1999. doi: 10.1051/aas:1999434.

[90] Carlos Hoyos, Mark den Brok, Gijs Verdoes Kleijn, David Carter, Marc Balcells, Rafael Guzmán, Reynier Peletier, Henry C. Ferguson, Paul Goudfrooij, Alister W. Graham, Derek Hammer, Arna M. Karick, John R. Lucey, Ana Matković, David Merritt, Mustapha Mouhcine, and Edwin Valentijn. The HST/ACS Coma Cluster Survey - III. Structural parameters of galaxies using single Sérsic fits. *MNRAS*, 411:2439–2460, March 2011. doi: 10.1111/j.1365-2966.2010.17855.x.

[91] M. J. Hudson, G. L. Harris, and W. E. Harris. Dark matter halos in galaxies and globular cluster populations. *ApJL*, 787:L5, May 2014. doi: 10.1088/2041-8205/787/1/L5.

[92] J. D. Hunter. Matplotlib: A 2D Graphics Environment. *Computing in Science and Engineering*, 9:90–95, May 2007. doi: 10.1109/MCSE.2007.55.

[93] T.-O. Husser, S. Wende-von Berg, S. Dreizler, D. Homeier, A. Reiners, T. Barman, and P. H. Hauschildt. A new extensive

library of PHOENIX stellar atmospheres and synthetic spectra. *A&A*, 553:A6, May 2013. doi: 10.1051/0004-6361/201219058.

[94] L. P. Jenkins, A. E. Hornschemeier, B. Mobasher, D. M. Alexander, and F. E. Bauer. Uncovering the near-ir dwarf galaxy population of the coma cluster with spitzer irac. *ApJ*, 666:846–862, September 2007. doi: 10.1086/520035.

[95] Y. Jiménez-Teja, R. A. Dupke, R. Lopes de Oliveira, H. S. Xavier, P. R. T. Coelho, A. L. Chies-Santos, C. López-Sanjuan, A. Alvarez-Candal, M. V. Costa-Duarte, E. Telles, J. A. Hernandez-Jimenez, N. Benítez, J. Alcaniz, J. Cenarro, D. Cristóbal-Hornillos, A. Ederoclite, A. Marín-Franch, C. Mendes de Oliveira, M. Moles, L. Sodré, J. Varela, and H. Vázquez Ramió. J-PLUS: Analysis of the intracluster light in the Coma cluster. *A&A*, 622:A183, Feb 2019. doi: 10.1051/0004-6361/201833547.

[96] Yolanda Jiménez-Teja, Renato Dupke, Narciso Benítez, Anton M. Koekemoer, Adi Zitrin, Keiichi Umetsu, Bodo L. Ziegler, Brenda L. Frye, Holland Ford, Rychard J. Bouwens, Larry D. Bradley, Thomas Broadhurst, Dan Coe, Megan Donahue, Genevieve J. Graves, Claudio Grillo, Leopoldo Infante, Stephanie Jouvel, Daniel D. Kelson, Ofer Lahav, Ruth Lazkoz, Dorom Lemze, Dan Maoz, Elinor Medezinski, Peter Melchior, Massimo Meneghetti, Amata Mercurio, Julian Merten, Alberto Molino, Leonidas A. Moustakas, Mario Nonino, Sara Ogaz, Adam G. Riess, Piero Rosati, Jack Sayers, Stella Seitz, and Wei Zheng. Unveiling the Dynamical State of Massive Clusters through the ICL Fraction. *ApJ*, 857:79, April 2018. doi: 10.3847/1538-4357/aab70f.

[97] J. B. Jones, M. J. Drinkwater, R. Jurek, S. Phillipps, M. D. Gregg, K. Bekki, W. J. Couch, A. Karick, Q. A. Parker, and R. M. Smith. Discovery of Ultracompact Dwarf Galaxies in the Virgo Cluster. *AJ*, 131:312–324, January 2006. doi: 10.1086/497960.

[98] Andrés Jordán, Eric W. Peng, John P. Blakeslee, Patrick Côté, Susana Eyheramendy, and Laura Ferrarese. The ACS Fornax Cluster Survey. XI. Catalog of Globular Cluster Candidates. *The Astrophysical Journal Supplement Series*, 221:13, November 2015. doi: 10.1088/0067-0049/221/1/13.

[99] J. Kadowaki, D. Zaritsky, and R. L. Donnerstein. Spectroscopy of ultra-diffuse galaxies in the coma cluster. *ApJL*, 838:L21, April 2017. doi: 10.3847/2041-8213/aa653d.

[100] J. J. Kavelaars, W. E. Harris, D. A. Hanes, J. E. Hesser, and C. J. Pritchet. The globular cluster systems in the coma el-

lipticals. i. the luminosity function in ngc 4874 and implications for hubble's constant. *ApJ*, 533:125–136, April 2000. doi: 10.1086/308642.

[101] S. M. Kent and J. E. Gunn. The dynamics of rich clusters of galaxies. I. The Coma cluster. *AJ*, 87:945–960, July 1982. doi: 10.1086/113178.

[102] R. Khatri and M. Gaspari. Thermal sz fluctuations in the icm: probing turbulence and thermodynamics in coma cluster with planck. *MNRAS*, 463:655–669, November 2016. doi: 10.1093/mnras/stw2027.

[103] T. Kitayama, Y. Ito, Y. Okada, H. Kaneda, H. Takahashi, N. Ota, T. Onaka, Y. Y. Tajiri, H. Nagata, and K. Yamada. Constraints on the intracluster dust emission in the coma cluster of galaxies. *ApJ*, 695:1191–1198, April 2009. doi: 10.1088/0004-637X/695/2/1191.

[104] J. Koda, M. Yagi, H. Yamanoi, and Y. Komiyama. Approximately a Thousand Ultra-diffuse Galaxies in the Coma Cluster. *ApJL*, 807:L2, July 2015. doi: 10.1088/2041-8205/807/1/L2.

[105] E. Kourkchi, H. G. Khosroshahi, D. Carter, A. M. Karick, E. Mármol-Queraltó, K. Chiboucas, R. B. Tully, B. Mobasher, R. Guzmán, A. Matković, and N. Gruel. Dwarf galaxies in the Coma cluster - I. Velocity dispersion measurements. *MNRAS*, 420:2819–2834, March 2012. doi: 10.1111/j.1365-2966.2011.19899.x.

[106] V. Kozhurina-Platais, N. Grogin, and E. Sabbi. Accuracy of the hst standard astrometric catalogs w.r.t. gaia. Technical report, February 2018.

[107] Pavel Kroupa. The dynamical evolution of stellar superclusters. *MNRAS*, 300:200–204, October 1998. doi: 10.1046/j.1365-8711.1998.01892.x.

[108] J. M. Kubo, A. Stebbins, J. Annis, I. P. Dell'Antonio, H. Lin, H. Khiabanian, and J. A. Frieman. The mass of the coma cluster from weak lensing in the sloan digital sky survey. *ApJ*, 671:1466–1470, December 2007. doi: 10.1086/523101.

[109] B. M. Lasker, M. G. Lattanzi, B. J. McLean, B. Bucciarelli, R. Drimmel, J. Garcia, G. Greene, F. Guglielmetti, C. Hanley, G. Hawkins, V. G. Laidler, C. Loomis, M. Meakes, R. Mignani, R. Morbidelli, J. Morrison, R. Pannunzio, A. Rosenberg, M. Sarasso, R. L. Smart, A. Spagna, C. R. Sturch, A. Volpicelli, R. L. White, D. Wolfe, and A. Zacchei. The Second-Generation Guide Star Catalog: Description and Properties. *AJ*, 136:735–766, August 2008. doi: 10.1088/0004-6256/136/2/735.

[110] D. Le Borgne, B. Rocca-Volmerange, P. Prugniel, A. Lançon, M. Fioc, and C. Soubiran. Evolutionary synthesis of galaxies at high spectral resolution with the code PEGASE-HR. Metallicity and age tracers. *A&A*, 425:881–897, October 2004. doi: 10.1051/0004-6361:200400044.

[111] Ryan Leaman, Don A. VandenBerg, and J. Trevor Mendel. The bifurcated age-metallicity relation of milky way globular clusters and its implications for the accretion history of the galaxy. *MNRAS*, 436(1):122–135, November 2013. doi: 10.1093/mnras/stt1540. URL https://ui.adsabs.harvard.edu/abs/2013MNRAS.436..122L.

[112] Bumhyun Lee, Aeree Chung, Stephanie Tonnesen, Jeffrey D. P. Kenney, O. Ivy Wong, B. Vollmer, Glen R. Petitpas, Hugh H. Crowl, and Jacqueline van Gorkom. The effect of ram pressure on the molecular gas of galaxies: three case studies in the virgo cluster. *MNRAS*, 466(2):1382–1398, April 2017. doi: 10.1093/mnras/stw3162. URL https://ui.adsabs.harvard.edu/abs/2017MNRAS.466.1382L.

[113] Myung Gyoon Lee and In Sung Jang. Globular Clusters and Spur Clusters in NGC 4921, the Brightest Spiral Galaxy in the Coma Cluster. *ApJ*, 819:77, March 2016. doi: 10.3847/0004-637X/819/1/77.

[114] S. Lim, E. W. Peng, P. Côté, L. V. Sales, M. den Brok, J. P. Blakeslee, and P. Guhathakurta. The Globular Cluster Systems of Ultra-diffuse Galaxies in the Coma Cluster. *ApJ*, 862:82, July 2018. doi: 10.3847/1538-4357/aacb81.

[115] C. Liu, E. W. Peng, P. Côté, L. Ferrarese, A. Jordán, J. C. Mihos, H.-X. Zhang, R. P. Muñoz, T. H. Puzia, A. Lançon, S. Gwyn, J.-C. Cuillandre, J. P. Blakeslee, A. Boselli, P. R. Durrell, P.-A. Duc, P. Guhathakurta, L. A. MacArthur, S. Mei, R. Sánchez-Janssen, and H. Xu. The Next Generation Virgo Cluster Survey. X. Properties of Ultra-compact Dwarfs in the M87, M49, and M60 Regions. *ApJ*, 812:34, October 2015. doi: 10.1088/0004-637X/812/1/34.

[116] D. Lokhorst, E. Starkenburg, A. W. McConnachie, J. F. Navarro, L. Ferrarese, P. Côté, C. Liu, E. W. Peng, S. D. J. Gwyn, J.-C. Cuillandre, and P. Guhathakurta. The next generation virgo cluster survey. xix. tomography of milky way substructures in the ngvs footprint. *ApJ*, 819:124, March 2016. doi: 10.3847/0004-637X/819/2/124.

[117] Omar López-Cruz, H. K. C. Yee, James P. Brown, Christine Jones, and William Forman. Are luminous cd halos formed

by the disruption of dwarf galaxies? *The Astrophysical Journal Letters*, 475(2):L97, 1997. URL http://stacks.iop.org/1538-4357/475/i=2/a=L97.

[118] N. Lyskova, E. Churazov, C. Zhang, W. Forman, C. Jones, K. Dolag, E. Roediger, and A. Sheardown. Close-up view of an ongoing merger between the ngc 4839 group and the coma cluster - a post-merger scenario. *MNRAS*, 485:2922–2934, May 2019. doi: 10.1093/mnras/stz597.

[119] J. P. Madrid, C. R. O'Neill, A. T. Gagliano, and J. R. Marvil. A wide-field map of intracluster globular clusters in coma. *ApJ*, 867:144, November 2018. doi: 10.3847/1538-4357/aae206.

[120] Juan P. Madrid, Alister W. Graham, William E. Harris, Paul Goudfrooij, Duncan A. Forbes, David Carter, John P. Blakeslee, Lee R. Spitler, and Henry C. Ferguson. Ultra-compact Dwarfs in the Core of the Coma Cluster. *ApJ*, 722:1707–1715, October 2010. doi: 10.1088/0004-637X/722/2/1707.

[121] S. Mahajan, A. Singh, and D. Shobhana. Ultraviolet and optical view of galaxies in the coma supercluster. *MNRAS*, 478:4336–4347, August 2018. doi: 10.1093/mnras/sty1370.

[122] Cecilia Mateu, Justin I. Read, and Daisuke Kawata. Fourteen candidate RR Lyrae star streams in the inner Galaxy. *MNRAS*, 474:4112–4129, March 2018. doi: 10.1093/mnras/stx2937.

[123] A. W. McConnachie, M. J. Irwin, A. M. N. Ferguson, R. A. Ibata, G. F. Lewis, and N. Tanvir. Distances and metallicities for 17 Local Group galaxies. *MNRAS*, 356:979–997, January 2005. doi: 10.1111/j.1365-2966.2004.08514.x.

[124] S. Mei, J. P. Blakeslee, P. Côté, J. L. Tonry, M. J. West, L. Ferrarese, A. Jordán, E. W. Peng, A. Anthony, and D. Merritt. The ACS Virgo Cluster Survey. XIII. SBF Distance Catalog and the Three-dimensional Structure of the Virgo Cluster. *ApJ*, 655:144–162, January 2007. doi: 10.1086/509598.

[125] Y. Mellier, G. Mathez, A. Mazure, B. Chauvineau, and D. Proust. Subclustering and evolution of the Coma cluster. *A&A*, 199:67–72, June 1988.

[126] S. Mieske, M. Hilker, and L. Infante. Fornax compact object survey FCOS: On the nature of Ultra Compact Dwarf galaxies. *A&A*, 418:445–458, May 2004. doi: 10.1051/0004-6361:20035723.

[127] Steffen Mieske, Andrés Jordán, Patrick Côté, Eric W. Peng, Laura Ferrarese, John P. Blakeslee, Simona Mei, Holger Baumgardt, John L. Tonry, Leopoldo Infante, and Michael J. West.

The ACS Fornax Cluster Survey. IX. The Color-Magnitude Relation of Globular Cluster Systems. *ApJ*, 710:1672–1682, February 2010. doi: 10.1088/0004-637X/710/2/1672.

[128] J. C. Mihos, P. R. Durrell, L. Ferrarese, J. J. Feldmeier, P. Côté, E. W. Peng, P. Harding, C. Liu, S. Gwyn, and J.-C. Cuillandre. Galaxies at the Extremes: Ultra-diffuse Galaxies in the Virgo Cluster. *ApJL*, 809:L21, August 2015. doi: 10.1088/2041-8205/809/2/L21.

[129] Bahram Mobasher, Terry J. Bridges, Dave Carter, Bianca M. Poggianti, Y. Komiyama, N. Kashikawa, M. Doi, M. Iye, S. Okamura, M. Sekiguchi, K. Shimasaku, M. Yagi, and N. Yasuda. A Photometric and Spectroscopic Study of Dwarf and Giant Galaxies in the Coma Cluster. II. Spectroscopic Observations. *The Astrophysical Journal Supplement Series*, 137:279–296, December 2001. doi: 10.1086/323584.

[130] R. P. Muñoz, T. H. Puzia, A. Lançon, E. W. Peng, P. Côté, L. Ferrarese, J. P. Blakeslee, S. Mei, J.-C. Cuillandre, P. Hudelot, S. Courteau, P.-A. Duc, M. L. Balogh, A. Boselli, F. Bournaud, R. G. Carlberg, S. C. Chapman, P. Durrell, P. Eigenthaler, E. Emsellem, G. Gavazzi, S. Gwyn, M. Huertas-Company, O. Ilbert, A. Jordán, R. Läsker, R. Licitra, C. Liu, L. MacArthur, A. McConnachie, H. J. McCracken, Y. Mellier, C. Y. Peng, A. Raichoor, M. A. Taylor, J. L. Tonry, R. B. Tully, and H. Zhang. The Next Generation Virgo Cluster Survey-Infrared (NGVS-IR). I. A New Near-Ultraviolet, Optical, and Near-Infrared Globular Cluster Selection Tool. *ApJS*, 210:4, January 2014. doi: 10.1088/0067-0049/210/1/4.

[131] R. P. Muñoz, P. Eigenthaler, T. H. Puzia, M. A. Taylor, Y. Ordenes-Briceño, K. Alamo-Martínez, K. X. Ribbeck, S. Ángel, M. Capaccioli, P. Côté, L. Ferrarese, G. Galaz, M. Hempel, M. Hilker, A. Jordán, A. Lançon, S. Mieske, M. Paolillo, T. Richtler, R. Sánchez-Janssen, and H. Zhang. Unveiling a Rich System of Faint Dwarf Galaxies in the Next Generation Fornax Survey. *ApJL*, 813:L15, November 2015. doi: 10.1088/2041-8205/813/1/L15.

[132] D. M. Neumann, M. Arnaud, R. Gastaud, N. Aghanim, D. Lumb, U. G. Briel, W. T. Vestrand, G. C. Stewart, S. Molendi, and J. P. D. Mittaz. The NGC 4839 group falling into the Coma cluster observed by XMM-Newton. *A&A*, 365:L74–L79, January 2001. doi: 10.1051/0004-6361:20000182.

[133] Nadine Neumayer, Anil Seth, and Torsten Boeker. Nuclear star clusters. 2020.

[134] Yasna Ordenes-Briceño, Thomas H. Puzia, Paul Eigenthaler, Matthew A. Taylor, Roberto P. Muñoz, Hongxin Zhang, Karla Alamo-Martínez, Karen X. Ribbeck, Eva K. Grebel, Simón Ángel, Patrick Côté, Laura Ferrarese, Michael Hilker, Ariane Lançon, Steffen Mieske, Bryan W. Miller, Yu Rong, and Ruben Sánchez-Janssen. The Next Generation Fornax Survey (NGFS). IV. Mass and Age Bimodality of Nuclear Clusters in the Fornax Core Region. *ApJ*, 860:4, June 2018. doi: 10.3847/1538-4357/aac1b.

[135] C. Y. Peng, L. C. Ho, C. D. Impey, and H.-W. Rix. Detailed Decomposition of Galaxy Images. II. Beyond Axisymmetric Models. *AJ*, 139:2097–2129, June 2010. doi: 10.1088/0004-6256/139/6/2097.

[136] Chien Y. Peng, Luis C. Ho, Chris D. Impey, and Hans-Walter Rix. Detailed structural decomposition of galaxy images. *AJ*, 124(1):266–293, July 2002. doi: 10.1086/340952. URL https://ui.adsabs.harvard.edu/abs/2002AJ....124..266P.

[137] E. W. Peng and S. Lim. A rich globular cluster system in dragonfly 17: Are ultra-diffuse galaxies pure stellar halos? *ApJL*, 822:L31, May 2016. doi: 10.3847/2041-8205/822/2/L31.

[138] E. W. Peng, H. C. Ferguson, P. Goudfrooij, D. Hammer, J. R. Lucey, R. O. Marzke, T. H. Puzia, D. Carter, M. Balcells, T. Bridges, K. Chiboucas, C. del Burgo, A. W. Graham, R. Guzmán, M. J. Hudson, A. Matković, D. Merritt, B. W. Miller, M. Mouhcine, S. Phillipps, R. Sharples, R. J. Smith, B. Tully, and G. Verdoes Kleijn. The HST/ACS Coma Cluster Survey. IV. Intergalactic Globular Clusters and the Massive Globular Cluster System at the Core of the Coma Galaxy Cluster. *ApJ*, 730:23, March 2011. doi: 10.1088/0004-637X/730/1/23.

[139] Eric W. Peng, Andrés Jordán, Patrick Côté, John P. Blakeslee, Laura Ferrarese, Simona Mei, Michael J. West, David Merritt, Milos Milosavljević, and John L. Tonry. The ACS Virgo Cluster Survey. IX. The Color Distributions of Globular Cluster Systems in Early-Type Galaxies. *ApJ*, 639:95–119, March 2006. doi: 10.1086/498210.

[140] J. Pfeffer and H. Baumgardt. Ultra-compact dwarf galaxy formation by tidal stripping of nucleated dwarf galaxies. *MNRAS*, 433:1997–2005, August 2013. doi: 10.1093/mnras/stt867.

[141] S. Phillipps, M. J. Drinkwater, M. D. Gregg, and J. B. Jones. Ultracompact Dwarf Galaxies in the Fornax Cluster. *ApJ*, 560:201–206, October 2001. doi: 10.1086/322517.

[142] K. A. Pimbblet, S. J. Penny, and R. L. Davies. How typical is the coma cluster? *MNRAS*, 438:3049–3057, March 2014. doi: 10.1093/mnras/stt2411.

[143] Planck Collaboration, P. A. R. Ade, N. Aghanim, M. Arnaud, M. Ashdown, F. Atrio-Barandela, J. Aumont, C. Baccigalupi, A. Balbi, A. J. Banday, and et al. Planck intermediate results. X. Physics of the hot gas in the Coma cluster. *A&A*, 554:A140, June 2013. doi: 10.1051/0004-6361/201220247.

[144] Planck Collaboration, P. A. R. Ade, N. Aghanim, M. Arnaud, M. Ashdown, J. Aumont, C. Baccigalupi, A. J. Banday, R. B. Barreiro, J. G. Bartlett, and et al. Planck 2015 results. XIII. Cosmological parameters. *A&A*, 594:A13, September 2016. doi: 10.1051/0004-6361/201525830.

[145] Planck Collaboration, N. Aghanim, Y. Akrami, M. Ashdown, J. Aumont, C. Baccigalupi, M. Ballardini, A. J. Banday, R. B. Barreiro, N. Bartolo, S. Basak, R. Battye, K. Benabed, J. P. Bernard, M. Bersanelli, P. Bielewicz, J. J. Bock, J. R. Bond, J. Borrill, F. R. Bouchet, F. Boulanger, M. Bucher, C. Burigana, R. C. Butler, E. Calabrese, J. F. Cardoso, J. Carron, A. Challinor, H. C. Chiang, J. Chluba, L. P. L. Colombo, C. Combet, D. Contreras, B. P. Crill, F. Cuttaia, P. de Bernardis, G. de Zotti, J. Delabrouille, J. M. Delouis, E. Di Valentino, J. M. Diego, O. Doré, M. Douspis, A. Ducout, X. Dupac, S. Dusini, G. Efstathiou, F. Elsner, T. A. Enßlin, H. K. Eriksen, Y. Fantaye, M. Farhang, J. Fergusson, R. Fernandez-Cobos, F. Finelli, F. Forastieri, M. Frailis, E. Franceschi, A. Frolov, S. Galeotta, S. Galli, K. Ganga, R. T. Génova-Santos, M. Gerbino, T. Ghosh, J. González-Nuevo, K. M. Górski, S. Gratton, A. Gruppuso, J. E. Gudmundsson, J. Hamann, W. Handley, D. Herranz, E. Hivon, Z. Huang, A. H. Jaffe, W. C. Jones, A. Karakci, E. Keihänen, R. Keskitalo, K. Kiiveri, J. Kim, T. S. Kisner, L. Knox, N. Krachmalnicoff, M. Kunz, H. Kurki-Suonio, G. Lagache, J. M. Lamarre, A. Lasenby, M. Lattanzi, C. R. Lawrence, M. Le Jeune, P. Lemos, J. Lesgourgues, F. Levrier, A. Lewis, M. Liguori, P. B. Lilje, M. Lilley, V. Lindholm, M. López-Caniego, P. M. Lubin, Y. Z. Ma, J. F. Macías-Pérez, G. Maggio, D. Maino, N. Mandolesi, A. Mangilli, A. Marcos-Caballero, M. Maris, P. G. Martin, M. Martinelli, E. Martínez- González, S. Matarrese, N. Mauri, J. D. McEwen, P. R. Meinhold, A. Melchiorri, A. Mennella, M. Migliaccio, M. Millea, S. Mitra, M. A. Miville-Deschênes, D. Molinari, L. Montier, G. Morgante, A. Moss, P. Natoli, H. U. Nørgaard-Nielsen, L. Pagano, D. Paoletti, B. Partridge, G. Patanchon, H. V. Peiris, F. Perrotta, V. Pettorino, F. Piacentini, L. Polastri, G. Polenta, J. L. Puget, J. P. Rachen, M. Reinecke, M. Remazeilles, A. Renzi, G. Rocha, C. Rosset, G. Roudier, J. A. Rubiño-Martín,

B. Ruiz-Granados, L. Salvati, M. Sandri, M. Savelainen, D. Scott, E. P. S. Shellard, C. Sirignano, G. Sirri, L. D. Spencer, R. Sunyaev, A. S. Suur-Uski, J. A. Tauber, D. Tavagnacco, M. Tenti, L. Toffolatti, M. Tomasi, T. Trombetti, L. Valenziano, J. Valiviita, B. Van Tent, L. Vibert, P. Vielva, F. Villa, N. Vittorio, B. D. Wandelt, I. K. Wehus, M. White, S. D. M. White, A. Zacchei, and A. Zonca. Planck 2018 results. VI. Cosmological parameters. *ArXiv e-prints*, art. arXiv:1807.06209, July 2018.

[146] M. Powalka, A. Lançon, T. H. Puzia, E. W. Peng, C. Liu, R. P. Muñoz, J. P. Blakeslee, P. Côté, L. Ferrarese, J. Roediger, R. Sánchez-Janssen, H. Zhang, P. R. Durrell, J.-C. Cuillandre, P.-A. Duc, P. Guhathakurta, S. D. J. Gwyn, P. Hudelot, S. Mei, and E. Toloba. The next generation virgo cluster survey (ngvs). xxv. fiducial panchromatic colors of virgo core globular clusters and their comparison to model predictions. *ApJS*, 227:12, November 2016. doi: 10.3847/0067-0049/227/1/12.

[147] Mathieu Powalka, Thomas H. Puzia, Ariane Lançon, Eric W. Peng, Frederik Schönebeck, Karla Alamo-Martínez, Simón Ángel, John P. Blakeslee, Patrick Côté, Jean-Charles Cuillandre, Pierre-Alain Duc, Patrick Durrell, Laura Ferrarese, Eva K. Grebel, Puragra Guhathakurta, S. D. J. Gwyn, Harald Kuntschner, Sungsoon Lim, Chengze Liu, Mariya Lyubenova, J. Christopher Mihos, Roberto P. Muñoz, Yasna Ordenes-Briceño, Joel Roediger, Rubén Sánchez-Janssen, Chelsea Spengler, Elisa Toloba, and Hongxin Zhang. New constraints on a complex relation between globular cluster colors and environment. *ApJL*, 829(1):L5, September 2016. doi: 10.3847/2041-8205/829/1/L5. URL https://ui.adsabs.harvard.edu/abs/2016ApJ...829L...5P.

[148] Mathieu Powalka, Ariane Lançon, Thomas H. Puzia, Eric W. Peng, Chengze Liu, Roberto P. Muñoz, John P. Blakeslee, Patrick Côté, Laura Ferrarese, Joel Roediger, Rúben Sánchez-Janssen, Hongxin Zhang, Patrick R. Durrell, Jean-Charles Cuillandre, Pierre-Alain Duc, Puragra Guhathakurta, S. D. J. Gwyn, Patrick Hudelot, Simona Mei, and Elisa Toloba. The next generation virgo cluster survey (ngvs). xxvi. the issues of photometric age and metallicity estimates for globular clusters. *ApJ*, 844 (2):104, August 2017. doi: 10.3847/1538-4357/aa77b1. URL https://ui.adsabs.harvard.edu/abs/2017ApJ...844..104P.

[149] J. Price, S. Phillipps, A. Huxor, N. Trentham, H. C. Ferguson, R. O. Marzke, A. Hornschemeier, P. Goudfrooij, D. Hammer, R. B. Tully, K. Chiboucas, R. J. Smith, D. Carter, D. Merritt, M. Balcells, P. Erwin, and T. H. Puzia. The HST/ACS Coma Cluster Survey - V. Compact stellar systems in the

Coma Cluster. *MNRAS*, 397:1816–1835, August 2009. doi: 10.1111/j.1365-2966.2009.15122.x.

[150] J. Price, S. Phillipps, A. Huxor, R. J. Smith, and J. R. Lucey. The stellar populations of bright coma cluster galaxies. *MNRAS*, 411:2558–2585, March 2011. doi: 10.1111/j.1365-2966.2010.17862.x.

[151] Felipe Ramos-Almendares, Mario Abadi, Hernán Muriel, and Valeria Coenda. Intra-cluster Globular Clusters in a Simulated Galaxy Cluster. *ApJ*, 853:91, January 2018. doi: 10.3847/1538-4357/aaa1ef.

[152] M. Rejkuba. Globular cluster luminosity function as distance indicator. *Ap&SS*, 341(1):195–206, September 2012. doi: 10.1007/s10509-012-0986-9. URL https://ui.adsabs.harvard.edu/abs/2012Ap&SS.341..195R.

[153] Florent Renaud. Star clusters in evolving galaxies. *NewAR*, 81:1–38, Apr 2018. doi: 10.1016/j.newar.2018.03.001.

[154] Tom Richtler. *The Globular Cluster Luminosity Function: New Progress in Understanding an Old Distance Indicator*, volume 635, pages 281–305. 2003. doi: 10.1007/978-3-540-39882-0_15. URL https://ui.adsabs.harvard.edu/abs/2003LNP...635..281R.

[155] Ian D. Roberts and Laura C. Parker. Ram pressure stripping candidates in the coma cluster: evidence for enhanced star formation. *MNRAS*, 495(1):554–569, June 2020. doi: 10.1093/mnras/staa1213. URL https://ui.adsabs.harvard.edu/abs/2020MNRAS.495..554R.

[156] A. C. Robin, C. Reylé, S. Derrière, and S. Picaud. A synthetic view on structure and evolution of the Milky Way. *A&A*, 409:523–540, October 2003. doi: 10.1051/0004-6361:20031117.

[157] T. Robitaille and E. Bressert. APLpy: Astronomical Plotting Library in Python. Astrophysics Source Code Library, August 2012.

[158] J. Rossa, R. P. van der Marel, T. Böker, J. Gerssen, L. C. Ho, H.-W. Rix, J. C. Shields, and C.-J. Walcher. Hubble space telescope stis spectra of nuclear star clusters in spiral galaxies: Dependence of age and mass on hubble type. *AJ*, 132:1074–1099, September 2006. doi: 10.1086/505968.

[159] J. S. Sanders, A. C. Fabian, E. Churazov, A. A. Schekochihin, A. Simionescu, S. A. Walker, and N. Werner. Linear structures in the core of the coma cluster of galaxies. *Science*, 341:1365–1368, September 2013. doi: 10.1126/science.1238334.

[160] S. Saracino, E. Dalessandro, F. R. Ferraro, B. Lanzoni, L. Origlia, M. Salaris, A. Pietrinferni, D. Geisler, J. S. Kalirai, M. Correnti, R. E. Cohen, F. Mauro, S. Villanova, and C. Moni Bidin. On the use of the main-sequence knee (saddle) to measure globular cluster ages. *ApJ*, 860:95, June 2018. doi: 10.3847/1538-4357/aac2c2.

[161] Takuya Sato, Kyoko Matsushita, Naomi Ota, Kosuke Sato, Kazuhiro Nakazawa, and Craig L. Sarazin. Suzaku Observations of Iron K-Lines from the Intracluster Medium of the Coma Cluster. *Publications of the Astronomical Society of Japan*, 63:S991–S1007, November 2011. doi: 10.1093/pasj/63.sp3.S991.

[162] E. F. Schlafly and D. P. Finkbeiner. Measuring Reddening with Sloan Digital Sky Survey Stellar Spectra and Recalibrating SFD. *ApJ*, 737:103, August 2011. doi: 10.1088/0004-637X/737/2/103.

[163] M. Sirianni, A. R. Martel, M. J. Jee, D. van Orsow, and W. B. Sparks. Bias subtraction and correction of acs/wfc frames. In *HST Calibration Workshop : Hubble after the Installation of the ACS and the NICMOS Cooling System*, page 82, January 2003. URL https://ui.adsabs.harvard.edu/abs/2003hstc.conf...82S.

[164] M. Sirianni, M. J. Jee, N. Benítez, J. P. Blakeslee, A. R. Martel, G. Meurer, M. Clampin, G. De Marchi, H. C. Ford, R. Gilliland, G. F. Hartig, G. D. Illingworth, J. Mack, and W. J. McCann. The Photometric Performance and Calibration of the Hubble Space Telescope Advanced Camera for Surveys. *Publications of the Astronomical Society of the Pacific*, 117:1049–1112, October 2005. doi: 10.1086/444553.

[165] Letizia Stanghellini, A. Cesar González-García, and Arturo Manchado. Merging of Elliptical Galaxies as a Possible Origin of the Intergalactic Stellar Population. *ApJ*, 644:843–849, June 2006. doi: 10.1086/503825.

[166] M. B. Taylor. TOPCAT & STIL: Starlink Table/VOTable Processing Software. In P. Shopbell, M. Britton, and R. Ebert, editors, *Astronomical Data Analysis Software and Systems XIV*, volume 347 of *Astronomical Society of the Pacific Conference Series*, page 29, December 2005.

[167] M. B. Taylor. STILTS - A Package for Command-Line Processing of Tabular Data. In C. Gabriel, C. Arviset, D. Ponz, and S. Enrique, editors, *Astronomical Data Analysis Software and Systems XV*, volume 351 of *Astronomical Society of the Pacific Conference Series*, page 666, July 2006.

[168] C. Tortora, A. D. Romeo, N. R. Napolitano, V. Antonuccio-Delogu, A. Meza, J. Sommer-Larsen, and M. Capaccioli. Stel-

lar population gradients from cosmological simulations: dependence on mass and environment in local galaxies. *MNRAS*, 411: 627–634, February 2011. doi: 10.1111/j.1365-2966.2010.17708.x.

[169] O. Vaduvescu, V. Petropoulou, D. Reverte, and V. Pinter. Studying star forming dwarf galaxies in Abell 779, Abell 1367, Coma, and Hercules clusters. *A&A*, 616:A165, September 2018. doi: 10.1051/0004-6361/201833113.

[170] Remco F. J. van der Burg, Adam Muzzin, and Henk Hoekstra. The abundance and spatial distribution of ultra-diffuse galaxies in nearby galaxy clusters. *A&A*, 590:A20, May 2016. doi: 10.1051/0004-6361/201628222.

[171] Stéfan van der Walt, S. Chris Colbert, and Gaël Varoquaux. The numpy array: a structure for efficient numerical computation. *CoRR*, 13:22–30, 2011. doi: 10.1109/MCSE.2011.37. URL https://ieeexplore.ieee.org/document/5725236.

[172] P. G. van Dokkum, R. Abraham, A. Merritt, J. Zhang, M. Geha, and C. Conroy. Forty-seven Milky Way-sized, Extremely Diffuse Galaxies in the Coma Cluster. *ApJL*, 798:L45, January 2015. doi: 10.1088/2041-8205/798/2/L45.

[173] P. G. van Dokkum, A. J. Romanowsky, R. Abraham, J. P. Brodie, C. Conroy, M. Geha, A. Merritt, A. Villaume, and J. Zhang. Spectroscopic confirmation of the existence of large, diffuse galaxies in the coma cluster. *ApJL*, 804:L26, May 2015. doi: 10.1088/2041-8205/804/1/L26.

[174] P. G. van Dokkum, Roberto Abraham, Aaron J. Romanowsky, Jean Brodie, Charlie Conroy, Shany Danieli, Deborah Lokhorst, Allison Merritt, Lamiya Mowla, and Jielai Zhang. Extensive Globular Cluster Systems Associated with Ultra Diffuse Galaxies in the Coma Cluster. *ApJ*, 844:L11, July 2017. doi: 10.3847/2041-8213/aa7ca2.

[175] C. J. Walcher, R. P. van der Marel, D. McLaughlin, H. W. Rix, T. Böker, N. Häring, L. C. Ho, M. Sarzi, and J. C. Shields. Masses of Star Clusters in the Nuclei of Bulgeless Spiral Galaxies. *ApJ*, 618:237–246, January 2005. doi: 10.1086/425977.

[176] Song Wang, Jun Ma, Zhenyu Wu, and Xu Zhou. New 2MASS Near-infrared Photometry for Globular Clusters in M31. *AJ*, 148:4, July 2014. doi: 10.1088/0004-6256/148/1/4.

[177] Elizabeth H. Wehner and William E. Harris. From Supermassive Black Holes to Dwarf Elliptical Nuclei: A Mass Continuum. *ApJ*, 644:L17–L20, June 2006. doi: 10.1086/505387.

[178] P. Westera, T. Lejeune, R. Buser, F. Cuisinier, and G. Bruzual. A standard stellar library for evolutionary synthesis. III. Metallicity calibration. *A&A*, 381:524–538, January 2002. doi: 10.1051/0004-6361:20011493.

[179] Simon D. M. White, Ulrich G. Briel, and J. P. Henry. X-ray archeology in the Coma cluster. *MNRAS*, 261:L8–L12, March 1993. doi: 10.1093/mnras/261.1.L8.

[180] M. Yagi, J. Koda, Y. Komiyama, and H. Yamanoi. Catalog of Ultra-diffuse Galaxies in the Coma Clusters from Subaru Imaging Data. *ApJS*, 225:11, July 2016. doi: 10.3847/0067-0049/225/1/11.

[181] M. Yagi, J. Koda, Y. Komiyama, and H. Yamanoi. Erratum: "catalog of ultra diffuse galaxies in the coma clusters from subaru imaging data" (2016, apjs, 225, 11 [http://doi.org/10.3847/0067-0049/225/1/11]). *ApJS*, 230(1): 10, 2017. URL http://stacks.iop.org/0067-0049/230/i=1/a=10.

[182] Hong-Xin Zhang, Eric W. Peng, Patrick Côté, Chengze Liu, Laura Ferrarese, Jean-Charles Cuillandre, Nelson Caldwell, Stephen D. J. Gwyn, Andrés Jordán, Ariane Lançon, Biao Li, Roberto P. Muñoz, Thomas H. Puzia, Kenji Bekki, John P. Blakeslee, Alessandro Boselli, Michael J. Drinkwater, Pierre-Alain Duc, Patrick Durrell, Eric Emsellem, Peter Firth, and Rubén Sánchez-Janssen. The Next Generation Virgo Cluster Survey. VI. The Kinematics of Ultra- compact Dwarfs and Globular Clusters in M87. *ApJ*, 802:30, March 2015. doi: 10.1088/0004-637X/802/1/30.

[183] Hong-Xin Zhang, Thomas H. Puzia, Eric W. Peng, Chengze Liu, Patrick Côté, Laura Ferrarese, Pierre-Alain Duc, Paul Eigenthaler, Sungsoon Lim, Ariane Lançon, Roberto P. Muñoz, Joel Roediger, Ruben Sánchez-Janssen, Matthew A. Taylor, and Jincheng Yu. Stellar Population Properties of Ultracompact Dwarfs in M87: A Mass- Metallicity Correlation Connecting Low-metallicity Globular Clusters and Compact Ellipticals. *ApJ*, 858:37, May 2018. doi: 10.3847/1538-4357/aab88a.

[184] Jun-liang Zhao, Rong-shi Pan, and Yan-ping He. Studies on the Coma cluster—4. Structure and substructure. *ChA&A*, 17: 281–290, July 1993. doi: 10.1016/0275-1062(93)90094-6.

COLOPHON

This document was typeset using the typographical look-and-feel `classicthesis` developed by André Miede. The style was inspired by Robert Bringhurst's seminal book on typography "*The Elements of Typographic Style*". `classicthesis` is available for both LaTeX and LyX:

http://code.google.com/p/classicthesis/